NASA CONTRACTOR REPORT

NASA CR-1307

RECIRCULATION EFFECTS PRODUCED BY A PAIR OF HEATED JETS IMPINGING ON A GROUND PLANE

by Gordon R. Hall and Kenneth H. Rogers

Prepared by
NORTHROP CORPORATION
Hawthorne, Calif.
for Langley Research Center

NATIONAL AERONAUTICS AND SPACE ADMINISTRATION • WASHINGTON, D. C. • MAY 1969

NASA CR-1307

RECIRCULATION EFFECTS PRODUCED BY A PAIR OF HEATED JETS IMPINGING ON A GROUND PLANE

By Gordon R. Hall and Kenneth H. Rogers

Prepared under Contract No. NAS 1-7834 by
NORTHROP CORPORATION
Hawthorne, Calif.

for Langley Research Center

NATIONAL AERONAUTICS AND SPACE ADMINISTRATION

For sale by the Clearinghouse for Federal Scientific and Technical Information
Springfield, Virginia 22151 – CFSTI price $3.00

ABSTRACT

An experimental investigation of the recirculation effects resulting from the interaction of a pair of heated jets, a quiescent environment, a ground plane, and a pair of inlets was performed. Upwash blockage surfaces were also used for selected tests. Inlet temperature rise and upwash flow characteristics were determined for a wide range of model geometries and inlet/nozzle flow conditions. Details of the near flow field structure were obtained. Inlet temperature rise and induced aerodynamic forces have been related to the character of the near flow field. The results of the investigation lead to several significant conclusions which relate directly to model simulation of full-scale recirculation phenomena.

CONTENTS

RECIRCULATION EFFECTS PRODUCED BY A PAIR OF HEATED JETS IMPINGING ON A GROUND PLANE

by Gordon R. Hall and Kenneth H. Rogers
Northrop Corporation, Hawthorne, Calif.

SUMMARY

An experimental investigation of the recirculation effects resulting from the interaction of a pair of heated jets, a quiescent environment, a ground plane, and a pair of inlets was performed. Inlet temperature rise and upwash flow characteristics were determined for a wide range of model geometries and inlet/nozzle flow conditions.

The upwash, or "fountain," between the inlets was generally found to be concentrated in a region about three nozzle diameters in width, with peak velocities in excess of 100 ft/sec. The temperature distribution between the inlets was found to be relatively uniform, with peak temperatures in the upwash only slightly higher than inlet temperature levels. The stability of the upwash was found to be affected by nozzle height above the ground plane (H/D), internozzle spacing (S/D), nozzle inserts, and nozzle pressure ratio. Specifically, the upwash was found to be unstable at low values of H/D and S/D. The upwash was also found to become less stable with insertion of swirl vanes and turbulator discs upstream of the nozzle exits and less stable with decreasing nozzle pressure ratio.

Numerous tests were performed to determine the sensitivity of inlet temperature rise and/or upwash flow characteristics to variations in model geometry and inlet/nozzle flow conditions. The results of these tests led to many conclusions which have important implications with respect to modeling of recirculation phenomena. For example, the upwash flow and inlet temperature rise were found to be extremely sensitive to deviations in jet impingement angle with the ground plane and to nozzle pressure ratio differential; thus, in small-scale simulations of recirculation phenomena extreme care is required to insure that jet impingement angles are normal to the ground plane (if this is a condition to be simulated) and that the pressure ratios of the various nozzles are equal (if this is a condition to be simulated).

The upwash flow and inlet temperature rise were found to be moderately sensitive to the insertion of swirl vanes and turbulator discs upstream of the nozzle exits; thus, close simulation of full-scale jet exit flow conditions in small-scale recirculation investigations is important. The upwash flow and inlet temperature rise were found to be relatively insensitive to inlet flow rate and/or inlet Mach number; thus, in small-scale simulations of recirculation phenomena in which external model geometry distortion would be required in order to accommodate the internal plumbing necessary for true simulation of full-scale inlet flow rate, consideration could be given to reduction in inlet flow rate without compromise in the model simulation. The upwash temperature and inlet temperature rise were found to be proportional to the jet temperature differential above ambient; thus, investigation of recirculation phenomena in small-scale at reduced exhaust temperature levels could be considered in facilities which lack air supply systems at real engine temperature levels and/or for investigations where funding level prohibits a model designed to accommodate real engine exhaust temperatures.

The effects of upwash blockage surfaces attached at the nozzle exit plane also were investigated. The blockage surfaces were found to effectively protect the inlets from the high temperature upwash. The net lift of a two jet configuration with a blockage disc attached at the nozzle exits was found to be independent of the nozzle spacing and was found to correlate well with the net lift from a single jet configuration with a disc attached at the nozzle exit.

INTRODUCTION

Various phenomena associated with jet lift VTOL aircraft operating in ground proximity have drawn recent attention. Recirculation of exhaust gases about the aircraft resulting from interaction of the vertically directed lifting jets with the ground plane is one such phenomenon. Ingestion of the recirculating exhaust gases by the engine is of major concern due to the rather strong effect that hot gas ingestion can have on engine performance. In particular, ingestion of hot exhaust gases by the engines results in thrust degradation which, in turn, reduces net lift capability, and, generally would introduce aircraft imbalance in hover. Additionally, high rates of inlet temperature rise and/or large temperature distortions across the inlet face can result in engine stall.

Recirculation of exhaust gases also can result in aerodynamic forces on the vehicle which arise from the direct impingement of ground plane reflected exhaust flows on the aircraft structure. Additionally, aerodynamic forces result from the circulation of free air about the aircraft, the circulation being induced as a result of flow entrainment by the lifting jets and ground-jet flows. Although the pressure levels resulting from induced free air circulation and impingement of reflected exhaust gases generally are low, the extent of the surfaces affected is generally quite large. Hence, the total induced force can be large, having an appreciable effect on net lifting capability and aircraft balance in hover.

Recirculation of exhaust gases in large-scale jet lift VTOL models has been the subject of several recent investigations (e.g., References 1-5). These investigations generally have shown that recirculation effects are highly dependent upon the vehicle configuration and can be a serious problem -- especially for split engine configurations in which an upwash, or fountain, of hot gases is developed as a result of the interaction of opposing ground jet flows.

While full-scale investigations of recirculation effects of specific configurations provide guideline information useful in synthesizing aircraft configurations, they cannot provide generalized design data which would allow confident prediction of the ingestion characteristics and induced aerodynamic forces for an arbitrary VTOL aircraft. That is, extrapolation of data to configurations other than the actual configuration tested is not reliable due to the fact that major changes in exhaust gas ingestion and induced aerodynamic forces have been found to occur from what would seem to be minor changes in aircraft configuration (e.g., References 1-5). As a result, new VTOL configurations evolved from design studies need to be tested for ingestion and induced aerodynamic characteristics. With such evaluations required, small-scale simulations yielding results applicable to geometrically similar full-scale vehicles are highly desirable in order to avoid costly full-scale testing during the preliminary design stages of VTOL aircraft. Heretofore, however, sound techniques for modeling recirculation phenomena have not been established or demonstrated.

Additionally, since it is not feasible to generate generalized design data for ingestion and induced aerodynamic forces, it is important that one has an understanding of the types of near flow fields which can develop as a result of recirculation, along with some knowledge of how the flow fields relate to ingestion and vehicle pressure fields. With this understanding and knowledge, sound technical judgment can be exercised in synthesizing VTOL configurations with a high probability of success, thereby minimizing costly cut-and-try experimental approaches to configuration synthesis.

With the above problems in mind, an exploratory investigation directed toward attaining a basic understanding of recirculation problems has been conducted. The model chosen was a fundamental configuration which provided for the interaction of a pair of heated jets, a quiescent environment, a ground plane, and a pair of inlets. Some preliminary results with this model are reported in Reference 6. Reported herein are more complete and more comprehensive results of an investigation with the following specific objectives:

1. To determine inlet temperature rise and upwash flow characteristics over a wide range of model geometries and inlet/nozzle flow conditions.
2. To provide information on the details of the near flow field structure.
3. To relate inlet temperature rise and induced aerodynamic forces to the characteristics of the near flow field.
4. To provide information on modeling criteria and techniques required for simulation of full-scale recirculation phenomena in small scale.

SYMBOLS

A_e	Total nozzle area
A_p	Area of plate or blockage disc
D	Nozzle diameter
D_e	Effective nozzle diameter, based on total area of the nozzles
D_p	Plate or blockage disc diameter
F	Thrust
$\mathscr{f}$	Frequency
H	Nozzle height above ground plane
h	Height above ground plane
M_i	Inlet Mach number
P	Pressure
$\mathscr{P}_T(\mathscr{f})$	Power spectral density of temperature fluctuation
$\mathscr{P}_U(\mathscr{f})$	Power spectral density of velocity fluctuation
q	Ground-jet dynamic pressure
r	Radial distance from jet centerline
R	Nozzle radius
S	Distance between nozzle centerlines
T	Temperature
ΔT	Temperature differential above ambient
U	Velocity
U_o	Wind velocity
$\sqrt{\overline{u'^2}}/U$	RMS turbulence intensity of velocity fluctuations
X	Horizontal reference axis in interaction plane (normal to common plane of the nozzles)

SYMBOLS (Continued)

Y	Horizontal reference axis in common plane of nozzles
Z	Vertical distance from nozzle exit
β	Nozzle angular deviation from vertical, in common plane of nozzles
γ	Nozzle angular deviation from vertical, in plane normal to common plane of nozzles

Subscripts

N	Nozzle
T	Stagnation
∞	Ambient
1	Nozzle number 1
2	Nozzle number 2

TEST FACILITY AND MODEL

The investigation was performed in a test cell of the Northrop Inlet and Duct Facility. The test cell is 40 feet long, 14 feet wide, and 13 feet high and is enclosed by vented walls and ceiling. Additional ventilation is provided by double doors (extending from floor to ceiling across the full width of the cell) which open one end of the test cell to the external ambient environment.

The investigation was performed using the test rig shown in Figure 1. In designing the nozzle-inlet assembly, primary importance was placed on achieving vertical axisymmetric jets, with inlet geometry being of secondary importance. Thus, jet flows were provided by two nominally vertical pipes with convergent nozzles (1.25 inch exit diameter) attached to the ends. A semicircular inlet was attached to each of the jet pipes as illustrated in Figure 2. In order to minimize radiant heat exchange to thermal instrumentation mounted in the inlets, the exhaust pipes were wrapped with asbestos cloth.

The spacing between the nozzle centerlines was varied by means of an overhead crank (Figure 1). The height of the ground plane (a 4 foot by 4 foot flat asbestos board) was varied with respect to the nozzle exits by an overhead crane. In addition to nozzle height and spacing variations, the angle of the nozzle centerlines could be varied independently, both in their common plane and in the plane perpendicular to their common plane (henceforth referred to as the interaction plane). These angularity changes were accomplished by rotation of the vertical pipes about the overhead support.

Three circular plates of diameters 12, 18, and 24 inches (with holes for the exhaust jets to pass through) were provided for attachment to the nozzle exit plane for selected tests. The 12- and 24-inch diameter plates were designed to accommodate a single value of nozzle spacing while the 18-inch diameter plate was designed to accommodate three values of nozzle spacing.

Nozzle exhaust conditions were varied from the nominal open nozzle conditions by insertion of: (1) a nozzle centerbody held in place by four straight vanes; (2) a nozzle centerbody held in place by four vanes which induced swirl into the exhaust flow (approximately 12°); and (3) a turbulator disc upstream of the nozzle exit to promote an increase in the jet decay characteristics. Section views of the turbulator disc and swirl vane inserts are shown in Figure 3. The straight vane insert was identical in construction to the swirl vane insert with the exception, of course, that the vanes were straight.

The nominal exhaust temperature for the tests was 500°F and the nominal nozzle pressure ratio was 1.8 (jet exit velocity 1340 ft/sec). For selected tests, however, the exhaust temperature and the nozzle pressure ratio were varied. The nominal inlet Mach number was 0.4 but was varied for selected tests. The jet and inlet flow rates were equal at the above stated nominal values of nozzle and inlet flow conditions.

INSTRUMENTATION

Inlet temperatures. - Three high response bare bead thermocouples were located in each inlet to measure the inlet thermal environment. The specific locations of these thermocouples are shown in Figure 2 with details of the thermocouple construction shown in Figure 4. The sensing element of the thermocouples was fabricated from .002" chromel/alumel wire. Based on Reference 7, the time constant for the thermocouple/nominal flow environment combination was 10 milliseconds (or in terms of response to the sinusoidal input signal, flat response within 10% up to a frequency of about 8 cps), assuming an ideal butt weld junction through which the local thermal mass is not increased above that of the parent wire. The output of the thermocouples was recorded on magnetic tape and later played back on oscillograph tape.

Upwash flow. - The upwash flow was measured by a pressure/temperature rake mounted between the inlets. The sensing element of the rake included three thermocouples (construction similar to those of the inlets), four total pressure probes, and four static pressure probes, spaced as shown in Figure 5. The rake was mounted as shown in Figure 6 with the probe sensing elements at the level of the inlet entrances. Extensions at each end of the rake support were provided for mounting the rake at internozzle spacings greater than that shown in Figure 6. The output of the rake thermocouples also was recorded on magnetic tape and later played back on oscillograph tape. The pressures were read from a manometer board.

Ground plane pressures. - Thirty-one pressure tapes were provided in the ground plane to determine the ground plane pressure distribution for selected tests. The specific locations of the ground plane pressure measurements, which were read from a manometer board, are shown in Figure 7.

Blockage disc pressures. - Thirty pressure taps were provided on the undersurface of the 18 inch upwash blockage disc to determine the pressure distribution and net force on the disc. The specific location of the disc pressure measurements, which were read from a manometer board, are shown in Figure 8. The 12 inch and 24 inch upwash blockage discs were not instrumented.

Exhaust conditions. - The exhaust jet pressure was measured by a static pressure orifice, and the exhaust temperature by a bare bead thermocouple, both located upstream of the nozzle. The upstream static pressure, which was used for setting the exhaust pressure levels, was calibrated against a total pressure probe located at the nozzle exit during pretest calibrations.

Flow field. - A variety of quantitative instruments and flow visualization techniques was used to evaluate the external flow field. Ground-jet dynamic pressure and temperature profiles were measured using the rake shown in Figure 9. The rake pressures were read from a manometer board and the temperatures recorded on a multipoint temperature recorder. A constant temperature hot wire anemometer, used as both a velocity and temperature sensor, was used to survey the flow field. Data from the hot wire anemometer were initially monitored on an oscilloscope and later

recorded on magnetic tape for more detailed data analysis. Flow visualization included smoke injection, sparklers, water spray injection, oil streak patterns, tufts, and vanes. Flow visualization provided by smoke injection and sparklers was documented by high speed cameras. Additional details on the techniques used to evaluate the flow field are given in the particular sections which discuss the results obtained by the various techniques.

PROCEDURE

Test Procedures

The general procedure for conducting the tests was as follows:

1. The doors at the end of the test cell were opened to the external ambient environment (the model is near this end of the test cell). Fans at the other end of the test cell were set to provide a draft of about 2 ft/sec thus minimizing bulk heating of the test cell during preheating of the exhaust system and during data acquisition periods by convecting the hot gases to the external environment.

2. The inlet suction system was turned on and adjusted to the desired inlet Mach number (nominal $M_i = 0.4$).

3. The exhaust jets were turned on and the exhaust system preheated to give the desired steady state exhaust temperature (nominal exhaust temperature = 500 °F).

4. The exhaust jets were then turned off and the inlet and "upwash" rake temperatures were recorded to give prerun reference temperature conditions.

5. The exhaust jets were then turned back on (exhaust system still in the preheat condition) to the desired nozzle pressure.

6. Thermocouple and pressure data were recorded. The nominal data acquisition period for the thermocouple data was 30 seconds.

7. The exhaust jets were turned off and the inlet and "upwash" rake temperatures were recorded to give post-run reference temperature conditions.

Data Reduction

The inlet and upwash values of temperature rise were based on the average temperature rise over 20 seconds of recorded data. Although the selection of a 20-second averaging period was arbitrary, the average temperature rise was found to be essentially independent of time over the 30-second data acquisition period (provided the averaging period was greater than a few seconds in order to "filter" temperature oscillations which generally occurred at frequencies greater than about 3 cps).

Although data were recorded for the three thermocouples in each inlet, the data presented in subsequent sections are the time average of only the center thermocouple of each inlet. Selection of the center thermocouple for representation of inlet temperature rise was based on comparison of the three thermocouples of each inlet for several tests; it was found that the center thermocouple value was a representative average of all three thermocouples. Unless otherwise noted, "inlet temperature rise" for a particular test is the average value of inlet temperature rise for the center thermocouples of the two inlets. This is the case for nominally symmetrical geometries with nominally symmetrical exhaust flow conditions. For asymmetrical geometries or asymmetrical

exhaust conditions, for each case the two inlets may experience a significant difference in temperature rise, the "inlet temperature rise" is presented separately for each of the two inlets.

Calculation of the upwash velocities was based on the local difference between stagnation and static pressure in the upwash and on local density of the upwash, the density being determined from the local static pressure and temperature. The absence of data points on the curves for upwash velocity distribution is the result of having staggered pressure and temperature probes on the upwash rake (Figure 5).

DISCUSSION

The data obtained for various arrangements of two hot jets impinging on a flat surface are presented in the following discussion. The primary objective of these data is to illustrate trends on the effects of configuration and flow conditions on the inlet temperature rise, near-field flow characteristics, and jet-induced aerodynamic forces. As such, the actual numerical values of the data presented should not be considered as design data, but rather should give the reviewer additional insight into recirculation phenomena. The insight gained may be used to great advantage in synthesizing VTOL configurations, and perhaps more importantly, in providing guideline information on various elements of model design and test techniques in order to obtain more meaningful data in future model simulations of full-scale recirculation phenomena than have been obtained in the past.

Ingestion and Upwash Characteristics

Basic Data

Figure 10 shows a typical sample of the temperature time histories for the inlets and upwash flow. Although the temperature traces were relatively unsteady, the amplitude of the temperature oscillations about the mean value was generally no more than $\pm 10^{\circ}$F at frequencies predominantly less than 10 cps. Generally, the major temperature fluctuations recorded by the upwash and inlet thermocouples were in phase (e.g., Figure 10) thereby indicating large-scale temperature fluctuations, rather than localized fluctuations which might arise from small-scale turbulence. Exclusive of the temperature oscillations observed in Figure 10, the inlet and upwash temperature levels were found to be essentially independent of time over the duration of a 30-second period of data acquisition, with the exception of a few configurations in which the upwash was found to be unstable.

Repeatability

Figure 11 presents data on inlet temperature rise, upwash temperature, and upwash velocity for five tests run under "identical" conditions. The various tests were run periodically during the test program and, as such, represent a measure of the repeatability of the various measurements.

As can be seen from Figure 11, the upwash temperature and velocity profiles are fairly repeatable, with a spread in the upwash temperature data of about 10°F, and virtually no spread in the maximum value of upwash velocity within the five tests shown. There is, however, some deviation in the upwash line of symmetry from the midpoint between the nozzle centerlines from test to test, indicating the difficulty in obtaining a perfectly symmetrical upwash.

Although the spread in the inlet temperature data of Figure 11 (considering each inlet separately) is seen to be somewhat greater than the spread for the upwash temperature, the spread for the five tests is less than 10°F when averaging the temperature rise for the two inlets of each test. Furthermore, in reviewing the temperature distributions within each inlet considering all three thermocouple measurements, it was found

that the circumferential variation was generally less than 10°F. The foregoing comments suggest that only differences in inlet temperature rise of greater than about 10°F would indicate trends, while differences in temperature rise of less than about 10°F are probably within "data scatter."

Effect of Jet Height and Jet Spacing

Upwash stability. - Before proceeding with a discussion of the effect of jet height, H/D, and jet spacing, S/D, on inlet temperature rise and upwash temperature and velocity, some comments on the stability of the upwash flow, or fountain, are in order. First of all, the stability of the upwash was generally found to increase with increasing H/D and increasing S/D. Even under the most stable combinations of H/D and S/D, however, relatively small biases in nozzle pressure ratio and small values of jet inclination away from the vertical (in the common plane of the nozzles) were found to result in either a large bias in the upwash flow toward one nozzle, or total elimination of any upwash flow in the region between the inlets. Details of the upwash flow structure are discussed under "Flow Field Investigations."

At the lowest value of H/D investigated (i.e., H/D = 1), in combination with the two lowest values of nozzle spacing investigated (i.e., S/D = 4 and 7), the upwash flow was found to be completely unstable; that is, at these conditions, it was not possible to attain a symmetrical upwash between the inlets, but rather the upwash emanating from the ground plane was totally entrained by one jet or the other before reaching the level of the inlets. Additionally, a hysteresis effect was observed in attempting to obtain a symmetrical upwash condition by fine adjustment of one nozzle pressure ratio with respect to the other. Namely, it was found that the upwash emanating from the ground plane could be "switched" from being entrained by one jet to being entrained by the other jet by adjustment of the nozzle pressure ratio. The hysteresis associated with this nozzle pressure "switching" was found to be about 1/2 psi.

For H/D = 1, the incipient value of nozzle spacing for a marginally stable upwash condition was found to be S/D = 10. At all other values of H/D investigated (i.e., H/D = 3, 5, and 8), the upwash flow was found to be stable (within the limits discussed previously) at all values of S/D investigated (i.e., S/D = 4, 7, 10, and 15).

Upwash temperature and velocity. - Figures 12 and 13 show the effect of H/D and S/D, respectively, on the upwash temperature and velocity distributions. Based on the velocity distribution (and confirmed by manual survey with the hand), the upwash is concentrated midway between the inlets in a region of about three nozzle diameters in width.

The effect of H/D on the upwash temperature and velocity (Figure 12) is seen to be very significant. Maximum levels of temperature rise and velocity are about 70°F and 130 ft/sec (compared to jet exit velocity of nominally 1340 ft/sec), respectively, at H/D = 3. The distributions are seen to be relatively symmetrical between the inlets, except for the data at H/D = 1. As discussed previously, the upwash emanating from the ground plane for the configuration H/D = 1 at S/D = 7 was found to be unstable. As a result, there is very little upwash velocity midway between the inlets. Correspondingly, the temperature field between the inlets also is reduced. The data do indicate, however, that there is a relatively strong upwash in the proximity of inlet No. 2.

In Figure 13 the upwash temperature and velocity distributions are seen to be less sensitive to S/D variations than to the H/D variations of Figure 12. Velocity data were not obtained at S/D = 4 because the pressure rake of Figure 5 could not be accommodated at this spacing.

Summary curves of the effect of H/D and S/D on maximum upwash temperature and velocity between the inlet are presented in Figures 14 and 15 in the form of contour maps. These maps were generated from cross plotting of data plotted vs H/D for the various values of S/D, and vs S/D for the various values of H/D. Also indicated in Figures 14 and 15 is the approximate region of upwash instability and the region in which the jets merge prior to impingement on the ground plane. As can be seen, the upwash temperature and velocity generally decrease with increasing H/D. The trend with S/D, however, reverses itself in that the temperature and velocity first increase with S/D and then decrease with S/D.

Inlet temperature rise. - Figure 16 shows a contour map for inlet temperature rise. The curves are very similar to those of Figure 14 for the upwash temperature rise, but at somewhat lower levels. Maximum levels of inlet temperature rise are seen to occur at low values of H/D and S/D.

Effect of Jet Angle

Figures 17 and 18 show the effect of canting the jets in their common plane. As can be seen from Figure 17, the upwash is extremely sensitive to small jet cant angles. A cant angle of only 1° is seen to result in a significant shift in the upwash toward inlet No. 1. For cant angles greater than about 4°, the upwash between the inlets is virtually eliminated. Indeed, for cant angles greater than about 4°, smoke injected in the region between the inlets showed a definite downflow in this region. The structure of the flow in this region was investigated in detail and is discussed in greater detail under "Flow Field Investigations."

Figure 18 shows the temperature rise for the two inlets as a function of the nozzle cant angle. As the upwash shifts toward inlet No. 1, there is first a major reduction in the temperature rise at inlet No. 2. A further increase in nozzle cant angle results in a reduction in temperature rise at inlet No. 1 as the upwash shifts outboard of both inlets.

In addition to parallel nozzles canted in their common plane, other canted nozzle configurations were investigated. These configurations are identified in Figure 19. The results of these configurations, for which the nozzles were canted 4°, are shown in Figure 20. For the nozzle cant configurations of Figure 20, there is seen to be little difference in the upwash temperature inlet temperature rise and the upwash velocity from those of the reference condition of parallel nozzles with axes normal to the ground plane: the deviation from the reference condition being not much greater than the magnitude of the deviation resulting from repeatability tests of the identical test conditions (Figure 11). This result is, of course, in strong contrast to the results of Figures 17 and 18 which show a strong effect of 4° nozzle cant (in the common plane of the nozzles).

In summarizing the effect of nozzle cant angle, it is concluded that the upwash and inlet temperature rise are extremely sensitive to small configuration asymmetries as viewed looking normal to the common plane of the nozzles (e.g., the configuration of Figure 17). Conversely, it is concluded that the upwash and inlet temperature rise are relatively insensitive to small nozzle cant angles which maintain geometric symmetry as viewed looking normal to the common plane of the nozzles (e.g., the configurations of Figure 19).

In view of the above result, extreme care must be taken in model tests of recirculation and induced aerodynamic phenomena to insure that the jet angles relative to the ground plane are identical to those for the full-scale vehicle being simulated. Further, since "nominal" hover conditions of full-scale vehicles will naturally involve some tolerance on attitude, model tests should include perturbation in attitude about the "nominal" condition in order to provide a realistic range of results applicable to the "nominal" condition.

Effect of Nozzle Configuration

For model investigations of recirculation phenomena, it becomes important to know how closely full-scale jet exhaust conditions must be simulated in the model. That is, the full-scale jet exhaust will differ from the exhaust of a simple open nozzle (which would be the most convenient configuration for model tests) in having different turbulence levels, generally some amount of swirl, and different axial velocity profiles due to the effect of the full-scale nozzle centerbody. One aspect of establishing modeling criteria, then, is to assess the effect of exhaust jet characteristics in recirculation phenomena.

Four different nozzle configurations were used to accomplish the above objective. These configurations included the basic open nozzle configuration (Figure 2), a configuration with a centerbody held in place by four straight vanes, a configuration with a centerbody held in place by four vanes which induced an estimated 12° average component of exhaust swirl at the nozzle exit (same direction for both nozzles), and a configuration in which a turbulator disc was placed upstream of the nozzle exit. Section views of the turbulator disc and swirl vane configurations are shown in Figure 3. The straight vane configuration was identical in construction to the swirl vane configuration with the exception, of course, that the vanes were straight. The results from this series of tests are presented in Figures 21 through 29.

Exhaust jet characteristics. - Figures 21 through 24 present exhaust jet dynamic pressure profiles for the various nozzle configurations tested. The open nozzle profiles (Figure 21) indicate uniform flow at the exit, with a gradual decay of the dynamic pressure peak with distance from the nozzle exit, and spreading of the jet boundaries at approximately 7° with respect to the jet centerline. As can be seen, there is virtually no difference in the open nozzle profiles due to the jet temperature.

Figure 22 shows the dynamic pressure profiles for the configuration with a centerbody held in place by straight vanes. The only apparent difference in the profiles for this configuration compared to those of the open nozzle is a small depression in the profiles close to the nozzle exit. On the other hand, the profiles of Figure 23, representing the centerbody held in place by swirl inducing vanes, are substantially different: there is a "hole" in the pressure profile at the nozzle centerline which persists for a

substantial distance downstream of the nozzle exit. The rather gross difference in the characteristics of the "straight vane" and "swirl vane" configuration is attributed to centrifugal force effects of the swirling flow which open up a "hole" at the jet centerline.

Figure 24 shows the dynamic pressure profiles with the turbulator disc installed. The most obvious difference between the "turbulator disc" profiles and those of the open nozzle is the nonuniformity of the flow at the jet exit.

Figure 25 compares the dynamic pressure decay with the distance from the nozzle exit for the various configurations. The curve for the "straight vane" configuration is seen to be virtually the same as for the open nozzle, except at small values of Z/D where a depression in the pressure profile results from the centerbody. The dynamic pressure decay rates for the "turbulator disc," and particularly for the "swirl vane," however, are seen to be significantly higher than for the open nozzle configuration. Note that curves are shown for both the maximum local value of dynamic pressure and the centerline dynamic pressure for the "swirl vane" configuration. Comparison of the two curves indicates a centerline depression in the dynamic profile which persists for about 10 diameters from the nozzle exit.

Figure 26 shows the distribution of the RMS turbulence fluctuation (as a percent of the local mean velocity) measured at the nozzle exit for the various configurations. Of significance is the generally increased level of turbulence associated with the turbulator disc configuration. Although the percent of turbulence of the swirl vane configuration is seen to increase to high levels near the nozzle centerline ($r/R \rightarrow 0$), it is recalled that the local mean velocity for this configuration near the centerline is approximately zero, so that the absolute level of turbulence is actually less than that in regions away from the centerline. This same comment applies to the outer boundaries of the jet ($r/R \rightarrow 1.0$), for which case the percent turbulence increases for all configurations.

Upwash and inlet characteristics. - Figure 27 shows the upwash temperature and velocity distribution for the various nozzle configurations. The upwash temperature and velocity distributions for the open nozzle and straight vane configuration are essentially the same (as were the exhaust jet characteristics for these two configurations). The temperature and velocity distributions for the turbulator disc and swirl vane configurations, however, are significantly different from those of the open nozzle configuration (as were the exhaust jet characteristics). It would appear that the level of temperature and the velocity distribution of the upwash are rather sensitive to decay characteristics of the free jet -- that is, rapid velocity and temperature decay of the free jets result in rapid velocity and temperature decay of the upwash flow.

Detailed examination of the upwash flow for the various configurations indicates that the upwash with the turbulator disc was less stable than for the open nozzle and straight vane configuration. That is, maintaining a stable symmetrical upwash by fine adjustment of the nozzle pressures was more difficult with this configuration. For the swirl vane configuration, a stable symmetrical upwash was unattainable at the values of H/D and S/D investigated (viz, H/D = 3, 5, 8 at S/D = 7). The reason for the upwash instability with the swirl vane configuration is not clear. The instability incurred is reflected in the curves of Figure 27 which show a highly unsymmetrical temperature and velocity distribution for the swirl vane configuration.

Also shown in Figure 27 is the velocity distribution for the swirl vane configuration based on a symmetrical upwash. Although this condition could not be maintained as a steady state condition, it was possible to get quasi-steady data by continuous fine adjustment of the nozzle pressure which resulted in maintaining the upwash in a quasi-symmetrical condition.

Figure 28 shows the effect of H/D on the upwash temperature and velocity midway between the inlets. The rather strong effects of nozzle configuration indicated in Figure 27 are seen to persist at all values of H/D. Figure 29 shows the inlet temperature rise for the various configurations. Again, the strong effect of nozzle configuration is evident.

The result of Figures 27 through 29 indicate that close duplication of full-scale exhaust jet characteristics in small-scale investigations of recirculation phenomena is essential to attaining model results which are potentially applicable to the full-scale vehicles.

Effect of Upwash Blockage Surfaces

Tests were conducted to determine the effect of various blockage surfaces on upwash and ingestion characteristics. The surfaces included 12, 18, and 24 inch circular discs attached flush with the nozzle exits. Figure 30 shows the installed 18-inch disc configuration. All three disc sizes were found to effectively protect the inlets from the upwash flow. Detailed discussion of the disc pressure distributions and flow patterns in the region of the discs is presented in a later section.

Figure 31 shows inlet temperature rise for the various upwash blockage configurations. For comparative purposes, the reference "open" configuration (i.e., no upwash blockage) is also shown. As can be seen, all three discs resulted in significant reductions in inlet temperature rise from the reference level of the "open" configuration.

Effect of Exhaust Temperature

Figure 32 shows the upwash temperature and velocity distributions for three different levels of exhaust gas temperature. The upwash temperature is seen to be strongly dependent on the exhaust gas temperature level while the upwash velocity is seen to be rather insensitive to the temperature level over the range of exhaust temperatures investigated.

Figure 33 shows the inlet temperature rise as a function of exhaust temperature. The experimental data are seen to lie approximately on a straight line whose slope is 0.14. That is, the inlet temperature rise is proportional to the difference between the exhaust gas temperature and the ambient temperature. Although the range of temperature levels investigated was limited, the above result would suggest that model tests of ingestion phenomena could be conducted at reduced temperature levels without serious compromise in the test results. If so, large savings could be effected in model and operational costs and, depending upon the particular facility capability, could make the difference of whether or not tests could be conducted at all.

Figure 34 shows the effect of one jet heated (nozzle 2) and one jet cold (nozzle 1). The data are compared to the reference condition of both jets heated. The results give insight to the degree of mixing which occurs between the two ground-jets which meet to form the upwash. That is, with little mixing, the upwash temperature in the proximity of the cold jet would be near ambient while the upwash temperature in the proximity of the hot jet would be about the same as for the case of both jets heated. On the other hand, with complete mixing, the temperature distribution between the inlets would be symmetrical about the midpoint between the two inlets and at one half the level obtained with both jets heated. As can be seen from the temperature distribution of Figure 34, the latter (i.e., complete mixing of the two opposing ground-jet flows prior to reaching the level of the inlets) is, in fact, very nearly achieved. Complete mixing within such a short path length would indicate intense turbulence at the ground stagnation region between the jets and/or within the free upwash flow. Turbulence levels within the upwash are discussed in more detail in a later section.

Effect of Nozzle Pressure

Figure 35 shows the upwash temperature and velocity distribution for several values of nozzle pressure ratio. The upwash temperature is seen to be relatively insensitive to nozzle pressure ratio. The upwash velocity, however, is considerably more dependent on the nozzle pressure ratio. Figure 36 shows the upwash velocity distribution nondimensionalized with respect to the jet exit velocity. As can be seen, the nondimensionalizing process considerably reduces the percent spread of the upwash velocity with nozzle pressure ratio.

The stability of the upwash flow was found to decrease with decreasing pressure ratio, until at $P_N/P_\infty = 1.2$ the upwash was found to be unstable in that a symmetrical upwash could not be maintained. This unstable condition is reflected in the data of Figure 36 which show an unsymmetrical velocity distribution for $P_N/P_\infty = 1.2$.

Figure 37 shows similar upwash distributions, but with a bias in the pressure ratio between the two nozzles. A significant shift in the upwash flow is evident from the data of Figure 37 for nozzle pressure biases as little as 0.1 atmosphere. This shift was also observed by manual survey of the upwash with the hand. The structure of the flow in the region between the inlets with nozzle pressure bias (which is similar to the flow structure with nozzle cant angle) was investigated in detail and is discussed under "Flow Field Investigations."

Figure 38 shows the effect of nozzle pressure level and pressure bias on inlet temperature rise. The data show that inlet temperature rise is not very dependent on nozzle pressure ratio, provided the pressure ratio of the two nozzles are equal. On the other hand, for the case in which one nozzle pressure ratio is held constant while the other nozzle pressure ratio is varied, the data show that the level of inlet temperature rise is very sensitive to pressure biases between the two nozzles.

The above results on nozzle pressure level and pressure bias have important implications with respect to model testing of ingestion phenomena. The results suggest that exact matching of the inlet flow rates to the exhaust flow rates is not important, and further that for model configurations in which room for internal plumbing is limited, plumbing sizes might be reduced by running the nozzles at a reduced pressure ratio

without serious effect on ingestion levels (this same consideration is suggested in the section which follows, with respect to the inlet flow, which has even a stronger effect on the size of internal plumbing than the exhaust flow).

On the other hand, the results indicate that attaining equal nozzle pressure ratios for the various jets are extremely important in model testing. Further, in view of the sensitivity of inlet temperature rise to nozzle pressure ratio bias, it is suggested that any model investigation of full-scale ingestion phenomena (or induced aerodynamic forces) should examine the effect of nozzle pressure biases up to the limits of nozzle pressure tolerance that might occur within nominally "identical" full-scale engines.

Effect of Inlets

Figure 39 shows the effect of inlet Mach number (or inlet flow rate) on inlet temperature rise. Within the limits of data scatter, there is virtually no effect of inlet Mach number on inlet temperature rise. Figure 40 shows the effect of removing the inlets completely and surveying the upwash temperature field with an aspirated thermocouple. As can be seen, the upwash temperature field without inlets falls within the data band of the temperature field with inlets operating at $M_i = 0.4$.

Based on the above results, it is concluded that the region of influence of the inlets is very localized, and that the inlets have virtually no influence on the upwash flow. Rather, the upwash flow is established almost entirely by the jets. The inlets merely draw air from the local environment, having little influence in altering the environment. Although this result is demonstrated for the simple geometry of a pair of jets and inlets, it is thought to apply to more complex geometric configurations with the possible exception of flush inlets imbedded in relatively large surfaces of low contour, where it is possible that the velocity field set up along the surface by the inlet flow could affect attachment/separation phenomena of an upwash flow in the proximity of the surface.

The above result, namely that ingestion characteristics are rather insensitive to inlet flow conditions, has important implications with respect to small-scale investigations of ingestion phenomena. That is, in providing inlet flows for model tests by external suction techniques, the internal plumbing required to attain the full-scale values of inlet Mach number generally becomes excessively large, and in many cases would not be possible without geometric distortion of the model to accommodate the suction ducting system. On the other hand, with ingestion characteristics rather insensitive to inlet Mach number, a reduction in inlet Mach number might well be tolerated, in which case a model ducting system could be provided without resorting to geometric distortion of the model which could have a much more serious effect on the ingestion characteristics than a reduction of inlet Mach number.

The insensitivity to inlet conditions, along with the extreme sensitivity to exhaust jet angle and decay characteristics as discussed previously, also substantiates the approach to the model design for the current investigation -- that is, emphasizing quality and close control of jet exit condition (thus, the straight pipe section for nozzle supply) while attaching secondary importance to the inlet geometry (thus, the semiannular inlets attached to the vertical pipe).

Effect of Wind

Limited tests were conducted to determine the effect of wind on the upwash flow and inlet temperature rise. The primary purpose was to establish a wind criterion for "no wind" tests of near field recirculation phenomena. External wind was simulated by directing the flow from a 3-foot diameter fan toward the upwash flow (Figure 41). Due to the limited extent of the ground plane, and the limited cross-section of the wind, simulated interaction of the wind with the far field ground-jet was not possible. On the other hand, simulation of the interaction of the upwash flow with a cross flow (i.e., wind) was achieved.

Figure 42 shows the upwash temperature and velocity distribution for a wind orientation of 0° (i.e., wind parallel to the common plane of the nozzles). In addition to the quantitative data of Figure 42, the upwash flow was surveyed with the hand in order to provide additional insight as to the effect of wind on the upwash flow. Based on the manual survey, the upwash appeared to remain symmetrical with respect to the two inlets for wind speeds less than about 6-8 ft/sec. For wind speeds greater than about 8 ft/sec, a noticeable shift in the upwash toward inlet No. 2 occurred. With further increase in wind speed, the shift of the upwash toward inlet No. 2 increased, until at about 16 ft/sec, the potential upwash was deflected beyond inlet No. 2, thus resulting in elimination of any upwash between the inlets.

The data of Figure 42 reflect the above observations in that the upwash temperature near inlet No. 1 is seen to decrease with increasing wind speed while that near inlet No. 2 remains essentially unchanged. Also, the upwash velocity distribution indicates a definite shift of the upwash toward inlet No. 2 at the wind speed of 10 ft/sec.

Tests also were conducted at a wind orientation of 90° (i.e., wind parallel to the interaction plane). For the case of the 90° wind orientation, no significant change in either the upwash flow or inlet temperature rise was detected within the range of wind speeds investigated (i.e., wind ≤ 16 ft/sec).

Based on the foregoing, it is suggested that a "no wind" criterion for investigation of near field ingestion effects be taken, conservatively, as 3 mph.

Pressure Distributions

Ground Plane

Figure 43 represents a typical ground plane pressure distribution with both jets operating. Characteristic of the distribution is a relatively high pressure field in the proximity of the intersection of the interaction plane with the common plane of the jet (i.e., $X = 0$, $Y = 0$). For the example shown, a pressure peak in the neighborhood of 10% of the dynamic pressure of the jets issuing from the nozzles is observed at the intersection of these two reference planes. The level of the ground plane pressures in the region between the jets is indicative of the vertical pressure gradient that exists, and as such, is indicative of the relative strength of the upwash experienced.

The effect of H/D and S/D on the ground plane pressure distributions is shown in Figures 44 and 45, respectively. From Figure 44 it is seen that the effect of H/D variation on the ground plane pressure distribution is rather small within the range of

H/D's investigated. Although Figure 44 applies to a single value of nozzle spacing, this result was found to be typical of all values of nozzle spacing investigated.

Figure 45 shows the effect of nozzle spacing (S/D) on the ground plane pressure distribution. Although the characteristic shape of the pressure profiles is essentially unaltered with variation in S/D, there is a rather marked effect on the magnitude of the peak pressure occurring at the origin, the peak pressure decreasing from a value of about 20% of the jet dynamic pressure at S/D = 4 to about 2% at S/D = 15. A summary of the effects of H/D and S/D on ground plane pressure at the origin is shown in Figure 46.

Figure 47 shows a typical comparison of the ground plane pressure distribution for a configuration with an 18-inch upwash blockage disc in the plane of the jet exits (Figure 30) to that for the basic two-jet configuration without a blockage disc. The ground plane pressures were found to be less for configurations with the blockage disc, although the general distribution of pressure was essentially unaltered. The reduction in pressure level with the blockage disc is an expected result in that the net lift of the configuration with the blockage disc is less than the combined thrust of the basic nozzles due to a predominantly negative pressure field on the lower surface of the blockage disc. Thus, the total reaction force absorbed by the ground plane (which is equal to the net lift of jets plus blockage plate combination) is consequently reduced.

Blockage Disc

Figure 48 represents a typical pressure distribution on the undersurface of an 18-inch circular upwash blockage disc in the plane of the jet exits. Characteristic of the distribution is a positive pressure field in the proximity of the interaction plane, with the peak pressure occurring at the intersection of the interaction plane with the common plane of the jets (i.e., X = 0, Y = 0). The positive pressure field results from the impingement of the upwash flow in the interaction plane on the blockage disc.

Other than in the proximity of the interaction plane, the disc pressures are negative, with the peaks of the negative pressures occurring along a line joining the jets and about midway between the jet axes and the interaction plane. The region of negative pressure field on the disc results from the strong entrainment effect of the vertical and ground-jets which scavenge air from the outside environment. This is discussed in greater detail in a later section.

Figure 49 shows the effect of H/D on the blockage disc pressure distribution. As can be seen, the characteristic shape of the pressure distributions is the same at all values of H/D investigated. The magnitude of the pressure fields, however, is seen to decrease with increasing H/D: the positive region decreasing as a result of dissipation of the upwash flow with increasing height; the negative region decreasing as a result of increased venting of the vertical and ground-jets to the ambient environment.

Figure 50 shows the effect of nozzle spacing (S/D) on the blockage disc pressure distribution. Again the characteristic shape of the distributions is seen to remain unchanged. The amplitude of the maxima and minima, however, is seen to decrease with increasing nozzle spacing. In addition, the location of the minima, in remaining about midway between the nozzle centerlines and X-Y origin, is seen to shift outward from the origin with increasing S/D. A summary of the effects of H/D and S/D on the pressure at the origin of the disc is given in Figure 51.

Induced Force

The measured pressure fields on the blockage discs for the various H/D and S/D combinations were integrated to obtain the net force acting on the disc. Figure 52 shows the ratio of F_{net}/F_{jet} at the three values of H/D_e investigated, where F_{net} is the jet thrust plus the net force acting on the plate (positive force upward), F_{jet} is the jet thrust, and H/D_e is the height of the nozzle exit (and disc) from the ground referenced to the equivalent nozzle diameter whose area is the combined area of the jets.

Included in Figure 52 is a curve obtained from the data of Reference 8 for a single jet configuration with a centrally-located square plate attached flush with the nozzle exit. Interpolation of the data of Reference 8 between plate-to-jet area ratios was required in order to compare the single jet data on the same plate-to-jet area ratio basis as the two jet data of the current investigation. In addition, the data of Reference 8 have been corrected for a 2% "base loss" since the reference thrust of Reference 8 is installed thrust (i.e., plate attached) out of ground effect while the reference thrust of Figure 52 is the jet thrust, the former being about 2% less than the latter for the plate to jet area ratio of interest (Reference 9). Also shown in Figure 52 is an empirical equation from Reference 10 based on a rigorous correlation of data in which the effect of D_p/D_N, plate planform shape, nozzle pressure ratio, and jet Reynolds number were successfully correlated for numerous single jet configurations. For the case of a circular plate with a centrally-located jet, the empirical equation of Reference 10 reduces to

$$\frac{F_{net}}{F_{jet}} = \frac{F_{net_{H/D=\infty}}}{F_{jet}} - .012 \left[\frac{\frac{D_p}{D_N} - 1}{H/D_N} \right]^{2.3} \qquad (1)$$

where $F_{net_{H/D=\infty}}/F_{jet}$ is taken to be .98, again reflecting a 2% base loss.

Although there is no a priori reason to expect a correlation between the induced forces with a single jet configuration and a multi-jet configuration, due to the gross difference in the near field flow characteristics, an excellent correlation was found to exist. Figure 52 shows a strong effect of H/D_e on net lift, with good agreement between the net lift of the single-jet configuration based on the experimental data of Reference 8, the empirical equation of Reference 10, and the two-jet configuration of the current investigation. Since the above result is unexpected and not readily explainable, one might consider it a fortuitous result. Figure 53, however, strongly substantiates the result as being more than fortuitous.

Figure 53 shows F_{net}/F_{jet} as a function of the nozzle spacing, S/D. As can be seen the value of F_{net}/F_{jet} is essentially independent of nozzle spacing. Extrapolation of this result to the limiting case of S/D = 0 (i.e., single jet) would suggest the net lift of a single-jet configuration to be essentially the same as a two-jet configuration, which, indeed, is the case as per Figure 52. In view of the practical significance of the results observed herein, more extensive investigation and correlation of induced aerodynamic forces of multi-jet configurations are recommended.

Flow Field Investigations

Ground-Jet Profiles

Ground-jet dynamic pressure profiles and temperature profiles were measured using the rake shown in Figure 9. Data were obtained for single-jet and two-jet operation. The single-jet data can be considered to represent conditions in the common plane of the jets for two-jet operation (i.e., outboard along the Y-axis). The two-jet data were obtained in the interaction plane of the jets (i.e., along the X-axis).

The dynamic pressure profiles are shown in Figures 54 and 55. For the single jet (Figure 54), the horizontal and vertical axes are nondimensionalized with respect to the jet diameter, D. For the two-jet configuration (Figure 55), the axes are nondimensionalized with respect to the equivalent diameter of the two jets (i.e., the diameter of a jet whose area is the sum of the two jets), D_e. In comparing the profiles of Figures 54 and 55, it is evident that "ground-jet" in the interaction plane is much thicker than the ground-jet in the common plane. Correspondingly, the mass flux in the interaction plane is significantly higher than at any other circumferential location on the ground plane. This latter observation was readily made by a simple survey of the ground flow with the hand.

It should be noted that the "ground-jet" in the interaction plane is not entirely parallel to the ground, especially at small values of S/D_e, for which case the flow is both outward and upward. Only the horizontal component of the flow is measured in that the pressure probes were oriented parallel to the ground.

Temperature profiles for the ground-jet are shown in Figures 56 and 57. Again, the thickness of the "ground-jet" in the interaction plane is indicated to be considerably greater than in the common plane of the jets. Also, the temperature levels are higher in the interaction plane.

Figure 58 shows the nondimensional decay of the maximum value of ground-jet dynamic pressure, for single-jet and two-jet conditions. When referenced to the equivalent diameter, D_e, the dynamic pressure in the interaction plane is seen to decay more rapidly than in the common plane of the jets. In terms of absolute distances (i.e., referenced to D), however, the dynamic pressure decays more rapidly in the common plane of the jets. Comparison of the temperature decay is shown in Figure 59. The rate of temperature decay in the common plane of the jets is seen to be much faster than in the interaction plane, either on the basis of equivalent diameter or absolute distance.

Flow Visualization

Oil streak patterns. - A total qualitative picture of the flow field was obtained by the use of a variety of techniques. The flow field appears to be highly unsteady and complex but nevertheless with some basic order. Documentation of some aspects of the flow field was achieved with an oil streak technique. A vertical plate, with appropriate cut-outs for the nozzles and inlets, was installed in the common plane of the nozzle centerlines. Oil drops (with a luminescent additive) were placed on this plate and on the ground plane, after which the jets were turned on and the drops allowed to smear. Figure 60 shows the flow pattern corresponding to the symmetrical configuration of vertical jets, horizontal ground plane and equal nozzle pressure ratios. The nozzle spacing and height, referenced to the nozzle diameter, are, respectively, $S/D = 7$ and $H/D = 4$.

Figure 61 shows schematically a more detailed picture of this flow field which incorporates information obtained from all flow visualization techniques. The flow may be divided into two zones. In zone A the flow is very similar to the wall jet arising from the interaction of a single-jet with a normal plane. In zone B the flow is very different, with a major feature being the two rather large counter-rotating vortices. The opposing flow from the two-jets is forced upwards into a "fountain," but the strong entrainment effects of the jets causes much of this flow to double back and form the vortices. Some of the flow carries on, where it eventually meets a downward flow moving toward the inlets and is bent back by it. The stagnation region formed here is very unstable; indeed its existence in this instance can only be inferred.

A dramatic change takes place with the introduction of asymmetry in the configuration as viewed looking normal to the common plane of the nozzles. Figure 62 shows the flow associated with a nozzle cant angle of 6° and equal nozzle pressures. As may be seen, the left vortex has opened out, and the flow comprising it is now partially drawn into the right vortex and partially deflected over this and around the right exiting jet. The ground plane stagnation line is accordingly curved. Of major significance in this asymmetric configuration is that the direction of the flow between the jets is now downward due to viscous entrainment of the free air by the vortex and jets. Although the associated velocities were too low to create oil streak patterns, visualization with smoke clearly showed that the flow was directed downwards. The inlet temperature rise experienced under conditions corresponding to Figure 62 is, of course, considerably reduced from the levels experienced under the symmetrical conditions of Figure 60.

A similar flow structure results from a differential nozzle pressure in the absence of nozzle cant. This is illustrated in Figure 63 which shows the same flow feature as Figure 62, but with vertical jets and a differential nozzle pressure (i.e., right nozzle pressure lower than left nozzle pressure). Figure 64 shows a more detailed picture of the flow field corresponding to Figures 62 and 63, again incorporating information from all the visualization techniques.

Figure 65 shows the results of increasing the asymmetry of the configuration by combining nozzle cant and nozzle pressure differential. The pattern is essentially the same as for nozzle cant or nozzle pressure differential separately, but more of the air from the left jet now goes around the right jet and the diameter of the vortex is reduced. Figure 66 shows the results of a further increase in the left jet pressure. The flow from the left has now slid under the much weaker jet on the right, as shown by the oil streaks on the vertical wall, and the vortex has disappeared completely.

So far, the flow picture which has been described is one which arises when nozzle centerlines are several diameters apart. As physical intuition would suggest, it is found that as the nozzles are brought closer together a critical value of spacing is reached beyond which the two-jets interact with the ground very much like a combined bigger jet. This critical spacing was found to be $S/D \approx 3$.

Smoke injection and sparklers. - Additional flow field visualization documentation was obtained by injection of oil into the flow upstream of the nozzle exit and by sparklers held within the near flow field. The results were documented by a high speed camera. Figures 67 through 71 represent enlargements of individual frames taken from the movie.

Figure 67 shows a sequence of frames taken from the smoke visualization portion of the movie for a configuration in which the jets are vertical and the pressure ratios of the two nozzles are equal (corresponding to the flow structure schematic of Figure 61).

The extent of the rise of the smoke in Figure 68 is somewhat misleading, due primarily to the turbulent mixing regions which exist at the boundaries of the bulk flow of the gases; the bulk flow of the gases is, indeed, well below the inlet region (the proof of this assertion is in the upwash velocity data of Figure 37, the oil streak photograph of Figure 63, and in the visualization tests with sparklers which follow). However, mixing is vigorous enough that some smoke (i.e., gas above ambient temperature) enters the region of influence of the inlets, and is ingested by the inlets, even in the cases when the symmetrical fountain no longer exists.

Figure 69 shows a sequence of frames for a configuration with equal nozzle pressure ratios, but with the jets canted 6° from vertical. As can be seen, the characteristics are similar to those of Figure 68.

The flow field was also investigated using sparklers for flow visualization. Although the sparks emitted have an initial momentum of their own, the spark pattern indicates the characteristics of the main flow if the sparkler is placed in a velocity field greater than about 5 - 10 ft/sec. For higher velocities, the sparkler visualization technique is quite good. When the streamlines of the flow are strongly curved, however, the sparks (which are glowing particles) will tend to diverge from the actual fluid streamlines because of their inertial effects. The technique as used here, however, was only to illustrate the gross effects of nozzle pressure differential and nozzle cant on the upwash.

Figure 70 illustrates the effect of nozzle pressure differential with vertical jets. In Figure 70a the pressure ratios of the two nozzles are equal (corresponding to the flow structure schematic of Figure 61). The "flow" of sparks issuing from the sparkler held midway between the inlets is clearly upward. In Figure 70b the right nozzle pressure has been reduced below that of the left (corresponding to the flow structure schematic of Figure 64). For this case, the "flow" of sparks between the inlets is clearly downward. The reversal from the upflow condition of Figure 70a to the downflow condition of 70b was found to occur when the dynamic pressure of the right nozzle was reduced to about 55% of the left nozzle pressure.

Figure 71 shows the effect of nozzle cant (6° from vertical) with equal nozzle pressure ratios. Again, the flow of sparks between the inlets is clearly downward.

Flow with blockage discs. - This section primarily concerns the flow on the upper or inlet side of the blockage discs. The study of this flow was purely visual utilizing both sparklers as well as smoke generated by mixing streams of NH_3 and SO_2.

The major finding of interest is that the flow on much of the upper surface of disc is dominated by the sink effects of jet entrainment. This sink effect results in the appearance of two zones of flow as illustrated in Figure 72. The outer zone consists of flow which comes downwards, is turned by the disc, and is then entrained radially outward by the ground-jet. The inner zone consists of flow which is eventually swallowed by the inlets. Some of this flow comes downwards along with the flow which finally goes outwards, but is turned inwards and eventually goes into the inlet. As a result there is a closed stagnation curve on the surface of the disc corresponding to this separation of inner and outer flows. Additional flow comes downwards directly into the inlet. An unsteady free-air stagnation region is formed when the downcoming inlet flow meets some of the inlet flow which has been deflected inward by the disc. This is shown schematically in Figure 72.

The path of the "outer" flow after leaving the disc depends very much on the value of H/D. At values of H/D greater than about 2, the flow is turned fairly sharply around the edge of the disc, eventually being entrained primarily by the free vertical jets. This is shown schematically in Figure 72. When H/D is reduced to values less than about 2, the outer flow pattern changes significantly. There is less tendency for the outer flow to bend around the disc and move inwards in the entrainment process. This is shown schematically in Figure 73. It was also found that when H/D was reduced, the stagnation line separating inner and outer flows on the upper surface of the disc moved outward toward the edge of the disc.

Hot Wire Investigations

As has been shown in the discussions above, the important elements of the near flow field are the vertical jets and associated free shear layers, the upwash in region B (of Figure 61) and the ground-jets in region A (also of Figure 61). It was decided to explore representative positions in each of the above regions using a hot wire anemometer. Accordingly, measurements of velocity, RMS turbulence intensity and temperature were made at the locations shown in Figure 74.

The hot wire anemometer used was a DISA model 55D00, a constant temperature type. The velocity data were obtained with a probe having a platinum plated wire, 1 mm in length and 0.005 mm in diameter. The temperature measurements, involving operation of the instrument essentially as a resistance thermometer, were made with a probe having a wire made of platinum-iron alloy, 1.5 mm in length and 0.01 mm in diameter. The data were monitored on an oscilloscope with selected samples being recorded on a Minneapolis Honeywell 7600 FM tape recorder for subsequent analysis.

The hot wire data were expected to be highly unsteady. In order to characterize these data statistically it was decided to carry out spectral analyses of the taped samples. Spectral analysis essentially reveals the distribution of the fluctuation energy over the spectrum of fluctuation frequency. It was hoped that such analyses would help to determine: (1) whether the fluctuation characteristics of the velocity and temperature fluctuations in the upwash were the same; and (2) whether the fluctuation characteristics were dictated by the vertical jet-free shear layer mixing, the interaction of the jet with the ground plane, or the interaction of the opposed flows in forming the upwash.

Velocity and turbulence intensity. - Figure 75 shows the variation of the upwash velocity, U, and RMS turbulence intensity, $\sqrt{\frac{\overline{u'^2}}{U}}$, (measured at point 3 of Figure 74) as a function of nozzle pressure ratio and jet exit velocity for ambient temperature jets. The upwash velocity, U, is seen to increase with increasing nozzle pressure ratio, the indicated level being somewhat higher than obtained with the upwash pressure rake (Figure 35). The somewhat higher reading with the hot wire is at least in part attributed to the fact that the hot wire was oriented so as to measure the instantaneous total velocity vector within the interaction plane, while the pressure rake was limited to measuring only the vertical component of the velocity vector in the interaction plane. Thus, for the highly turbulent and unsteady flow within the upwash, one would expect a higher velocity to be indicated by the hot wire. The RMS turbulence intensity of the upwash is seen to be quite high, with values in the neighborhood of 40% - 50% of the mean upwash velocity.

Figure 76 shows the velocity profile of the ground-jet at a distance corresponding to point 2, for a nozzle pressure ratio of 1.2. The entire profile was measured with the intention of defining the different "layers" in the flow, so that fluctuation measurements could be made in positions representative of each layer. This was done because it was felt that the statistical characteristics of the velocity fluctuations in the ground-jet might depend upon the relative position within the ground-jet.

Also shown in Figure 76 is the distribution of turbulence intensity across the ground-jet. There is a maximum in the outer layer, followed by a dip to a local minimum near the point of maximum velocity, followed by a local rise. As indicated in Figure 76, the data used for subsequent spectral analysis were recorded at positions close to the above turbulence intensity maximum and minimum as well as at an intermediate position.

Spectral analysis. - Limited spectral analysis of the taped velocity and temperature fluctuations was prepared using a Technical Product Wave Analyzer Model 625. The results are shown in Figures 77 and 78.

Figure 77 shows the power spectral densities, $\mathscr{P}_U(\mathscr{f})$, of the velocity fluctuations, for the free shear layer, the ground-jet, and the upwash measured at points 1, 2, and 3, respectively , in Figure 74. The spectral density of the ground-jet at the height indicated in Figure 76 also was found to be typical of other "layers" within the ground-jet.

As can be seen in Figure 77, the velocity fluctuation spectra of the ground-jet and upwash are virtually the same shape, both exhibiting a rather broad stretch at constant spectral density followed by a sharp roll off. In contrast, the spectral density of the free shear layer exhibits a continuous decay with frequency. These spectra would imply that the nature of the velocity fluctuations of the free jet are substantially altered by the interaction with the ground plane, but that no significant further change occurs as a result of the two jet interaction in forming the upwash.

Figure 78 shows similar data for the temperature fluctuations. In contrast to the velocity data, the temperature fluctuation spectra of the ground-jet and upwash are quite different, while the spectra of the ground-jet and free shear layers are virtually identical. These results would imply that the nature of the temperature fluctuations of the

free jet are unaltered by the interaction with the ground plane, but that a significant change occurs as a result of the two-jet interaction in forming the upwash.

Considering the contrasting implications of Figures 77 and 78, along with the limited amount of data analyzed, it is difficult to reach any strong conclusions regarding the origin and mechanism governing the velocity and temperature fluctuations of the upwash.

CONCLUSIONS

The flow field, external thermal environment, and inlet thermal environment resulting from the interaction of a pair of heated jets, a ground plane, and a pair of inlets have been determined for a wide range of conditions. Details of the near flow field structure were obtained. Inlet temperature rise and induced aerodynamic forces have been related to the character of the near flow field. Many of the conclusions derived from the investigation have important implication with regard to modeling of recirculation phenomena, the implication having been discussed at length within the text. Some specific conclusions of the investigation are given below:

1. The upwash between the inlets generally was concentrated in a region about three nozzle diameters in width, with velocities frequently in excess of 100 ft/sec. The temperature distribution across the upwash was found to be relatively uniform, with peak upwash temperatures usually only slightly higher than inlet temperature levels.

2. The upwash was found to be unstable at low values of H/D and S/D for an open nozzle configuration. The stability of the upwash was found to be affected by exhaust nozzle inserts and nozzle pressure ratio, becoming less stable with the addition of swirl vanes, turbulator discs, and decreasing nozzle pressure ratio.

3. The upwash temperature and velocity and inlet temperature rise were found to decrease with increasing H/D and found to be most severe at an S/D value of approximately 7. Maximum values of inlet temperature rise were about 70°F for a jet temperature of 500°F.

4. Inlet temperature rise was found to be proportional to the difference between jet and ambient temperature.

5. The upwash and inlet temperature rise were found to be extremely sensitive to small nozzle cant angles which result in configuration asymmetries as viewed looking normal to the common plane of the nozzles. Conversely, the upwash and inlet temperature rise were found to be relatively insensitive to small nozzle cant angles which maintained symmetry as viewed looking normal to the common plane of the nozzles.

6. The upwash and inlet temperature rise were found to be sensitive to exhaust flow conditions as affected by the addition of various nozzle inserts. Appreciable reduction in upwash temperature and velocity and inlet temperature rise was observed with the insertion of swirl vanes and turbulator discs upstream of the nozzle exits.

7. Inlet temperature rise was found to be relatively insensitive to nozzle pressure ratio, provided the pressure ratios of the two nozzles were equal. On the other hand, large reductions in inlet temperature rise were found to result from relatively small differences in pressure ratio for the two nozzles.

8. The inlets were found to have virtually no effect on the upwash flow and inlet temperature rise. Rather, the upwash flow is established almost entirely by the jets, with the inlets merely swallowing air in their proximity.

9. The effect of wind in altering the near flow field was found to be negligible for wind speeds less than about 6 ft/sec.

10. Upwash blockage surfaces were found to effectively protect the inlets from the high temperature upwash.

11. The net lift of a two-jet configuration with a disc attached at the nozzle exits was found to be independent of jet spacing and was found to correlate well with the net lift from a single-jet configuration with a disc attached at the nozzle exit.

REFERENCES

1. Lavi, R.: "Parametric Investigation of VTOL Ground Proximity Effects." AIAA Paper No. 67-440, July 1967.

2. Hammond, A.D., McLemore, H.C.: "Hot-Gas Ingestion and Jet Interference Effects for Jet V/STOL Aircraft." Presented at AGARD Flight Mechanics Panel Meeting, Gottingen, West Germany, September 1967.

3. Lavi, R., Hall, G.R., Stark, W.W.: "Full-Scale Ground Proximity Investigation of a VTOL Fighter Model Aircraft." NASA CR-1098, June 1968.

4. McLemore, H.C., Smith, C.C., Jr.: "Hot-Gas Ingestion Investigation of Large-Scale Jet VTOL Fighter-Type Models." NASA TN D-4609, June 1968.

5. Hall, G.R.: "Recirculation and Ingestion Characteristics of a Large-Scale VTOL Lift Engine Pod." NASA CR-72410, August 1968.

6. Adarkar, D.B., Hall, G.R.: "The 'Fountain Effect' and VTOL Exhaust Ingestion." AIAA Paper No. 68-79, January 1968.

7. Hall, G.R., Bogdanovic, J.A.: "Response of Bare Wire Thermocouple to Temperature Variation in a Jet Engine Intake." AIAA Journal of Aircraft, July-August 1967.

8. Spreeman, K.P., Sherman, I.R.: "Effects of Ground Proximity on the Thrust of a Simple Downward-Directed Jet Beneath a Flat Surface." NASA TN-4407, September 1958.

9. Hammond, A.D.: "Thrust Losses in Hovering for Jet VTOL Aircraft." NASA SP-116, 1966, Pp. 163-176.

10. Wyatt, L.A.: "Static Tests of Ground Effect on Planforms Fitted With a Centrally-Located Round Lifting Jet," Ministry of Aviation, C.P. No. 749, 1964.

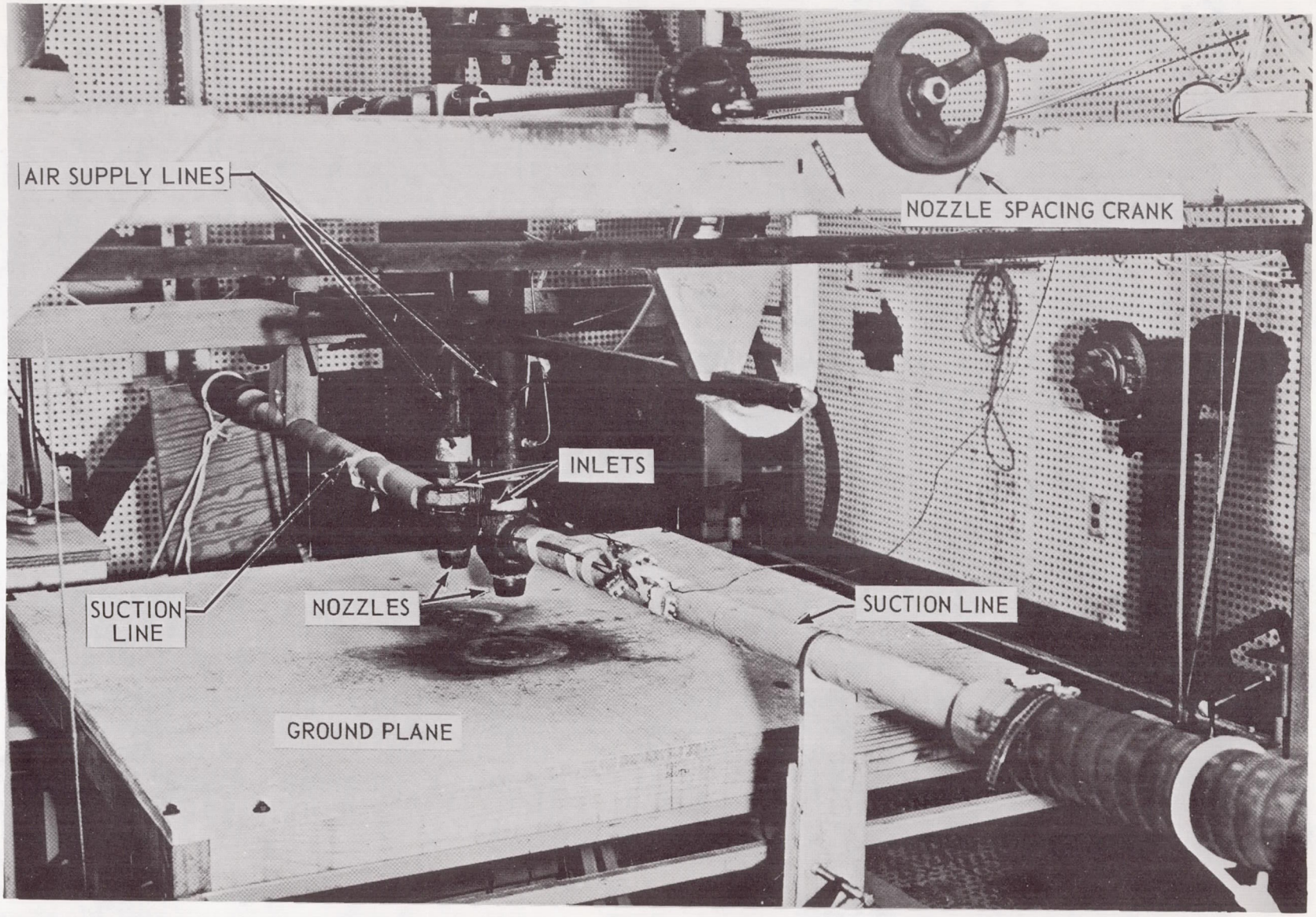

FIGURE 1 TEST RIG – DUAL JET INTERACTION

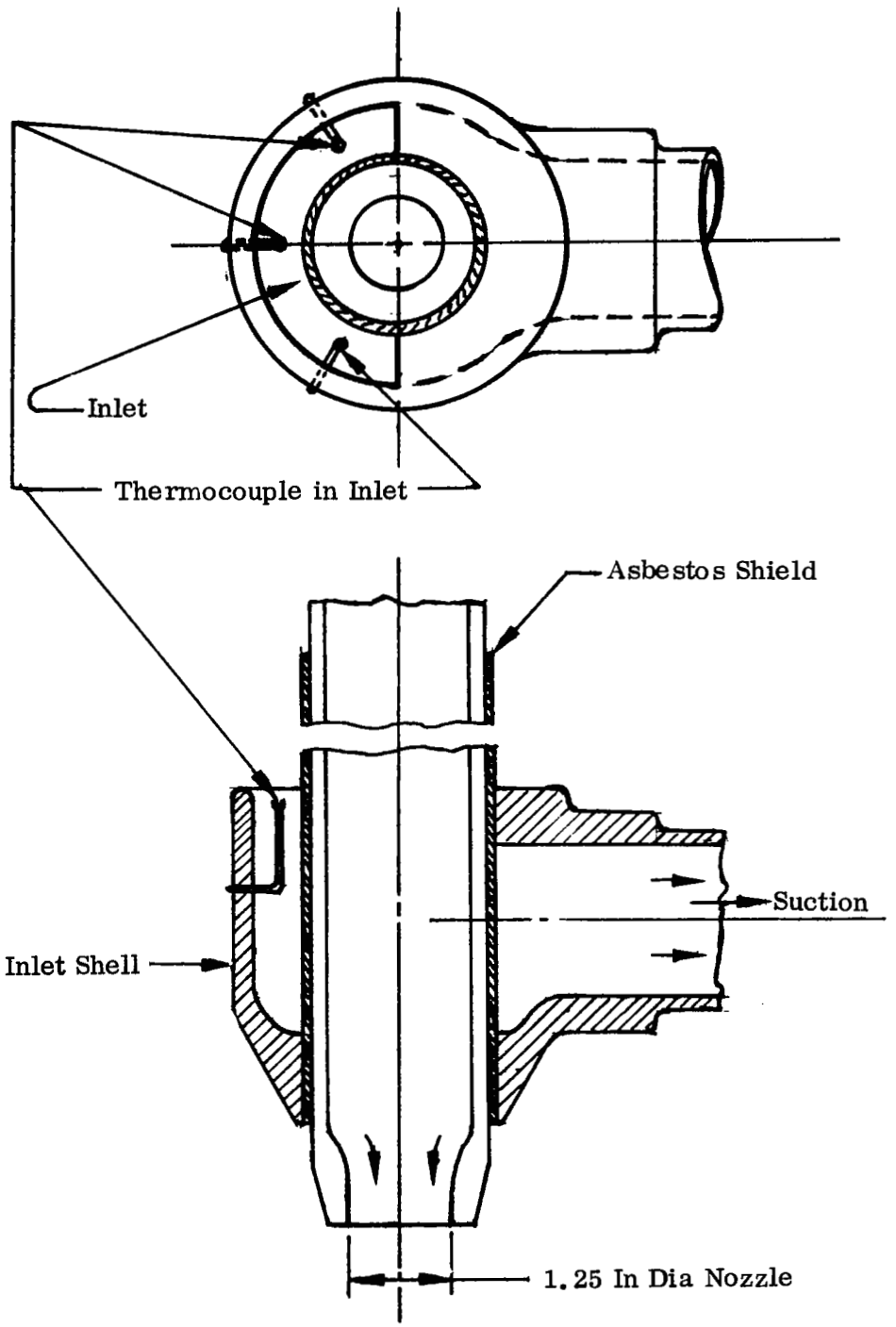

FIGURE 2. INLET AND NOZZLE ASSEMBLY

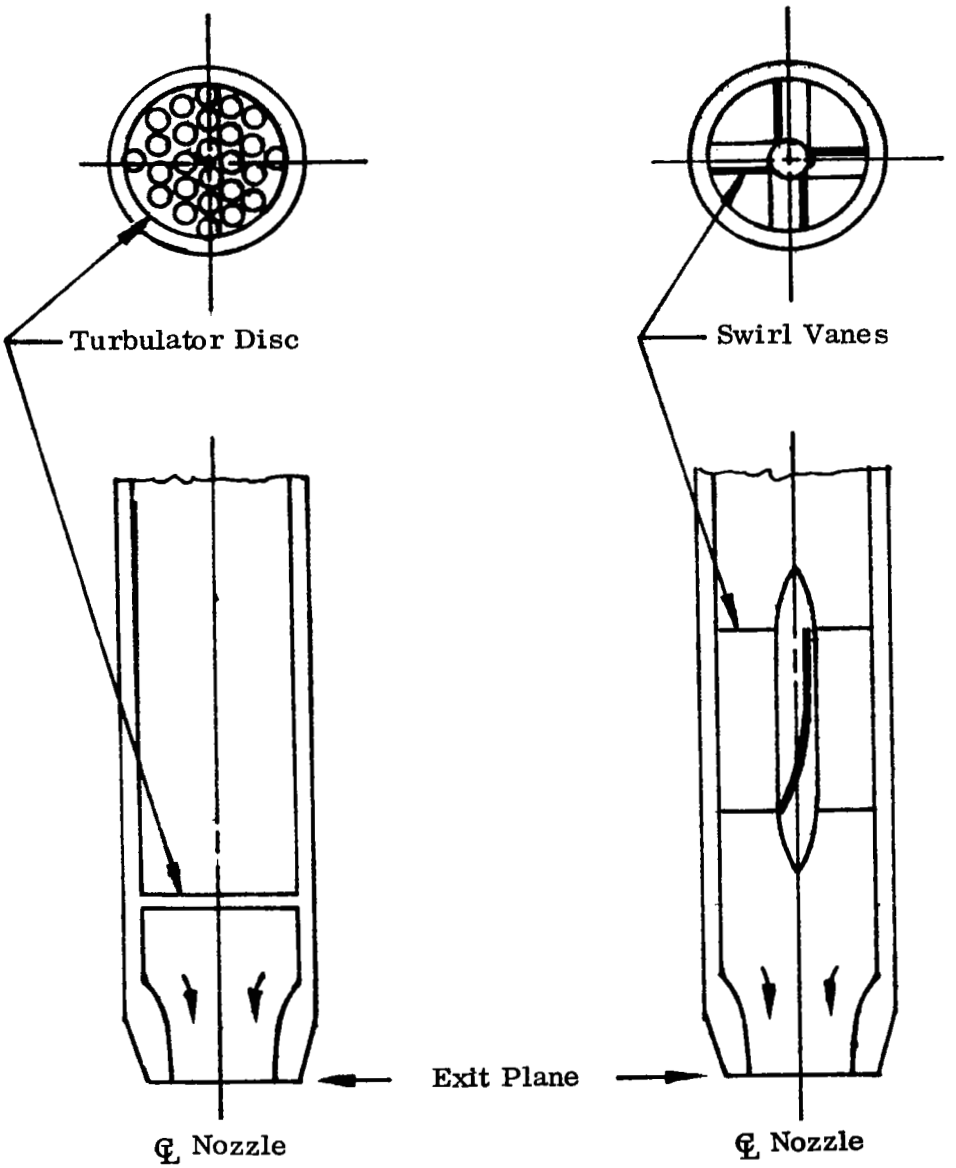

FIGURE 3. NOZZLE INSERTS - SECTION VIEWS

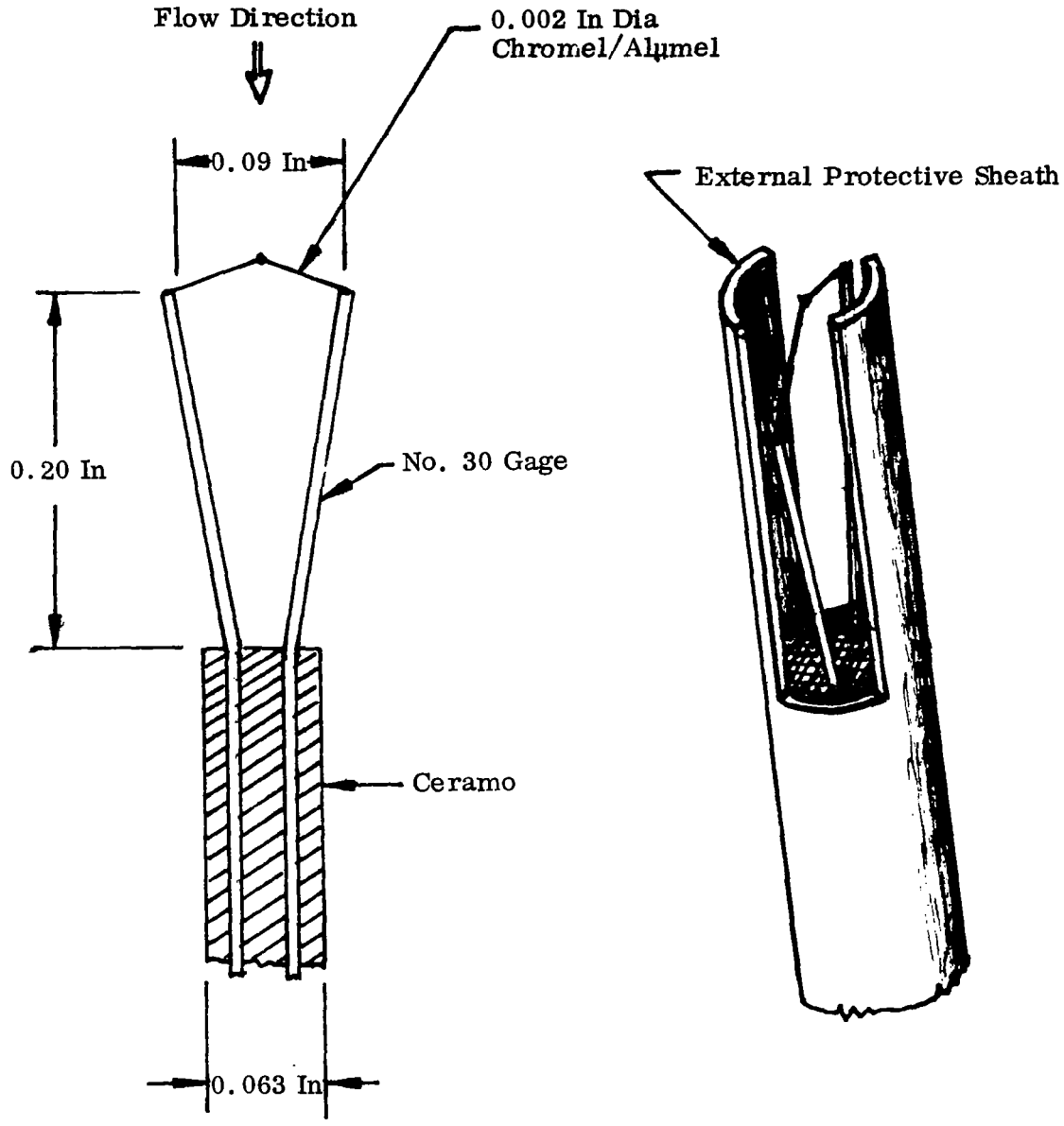

FIGURE 4. THERMOCOUPLE CONSTRUCTION DETAIL

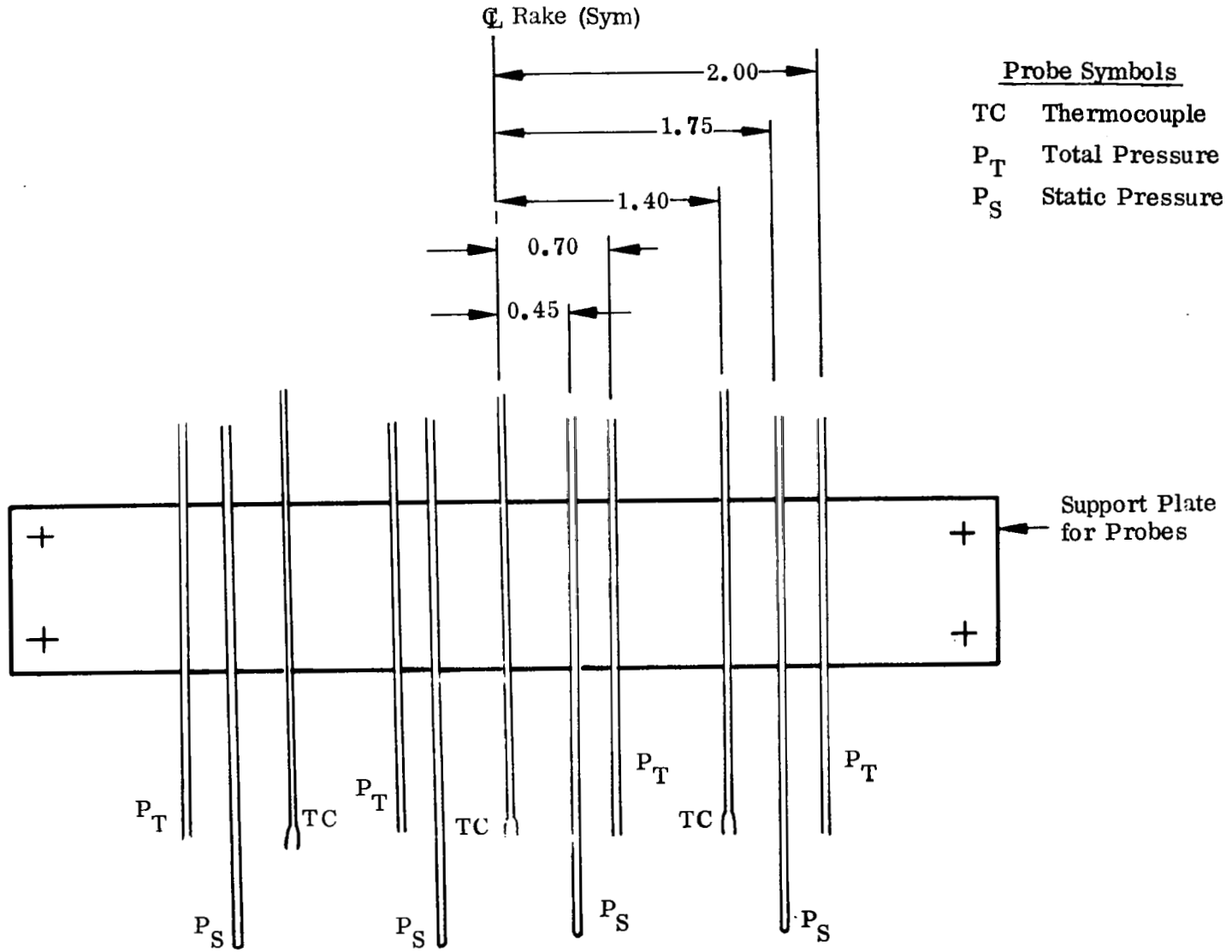

FIGURE 5. UPWASH PRESSURE/TEMPERATURE RAKE

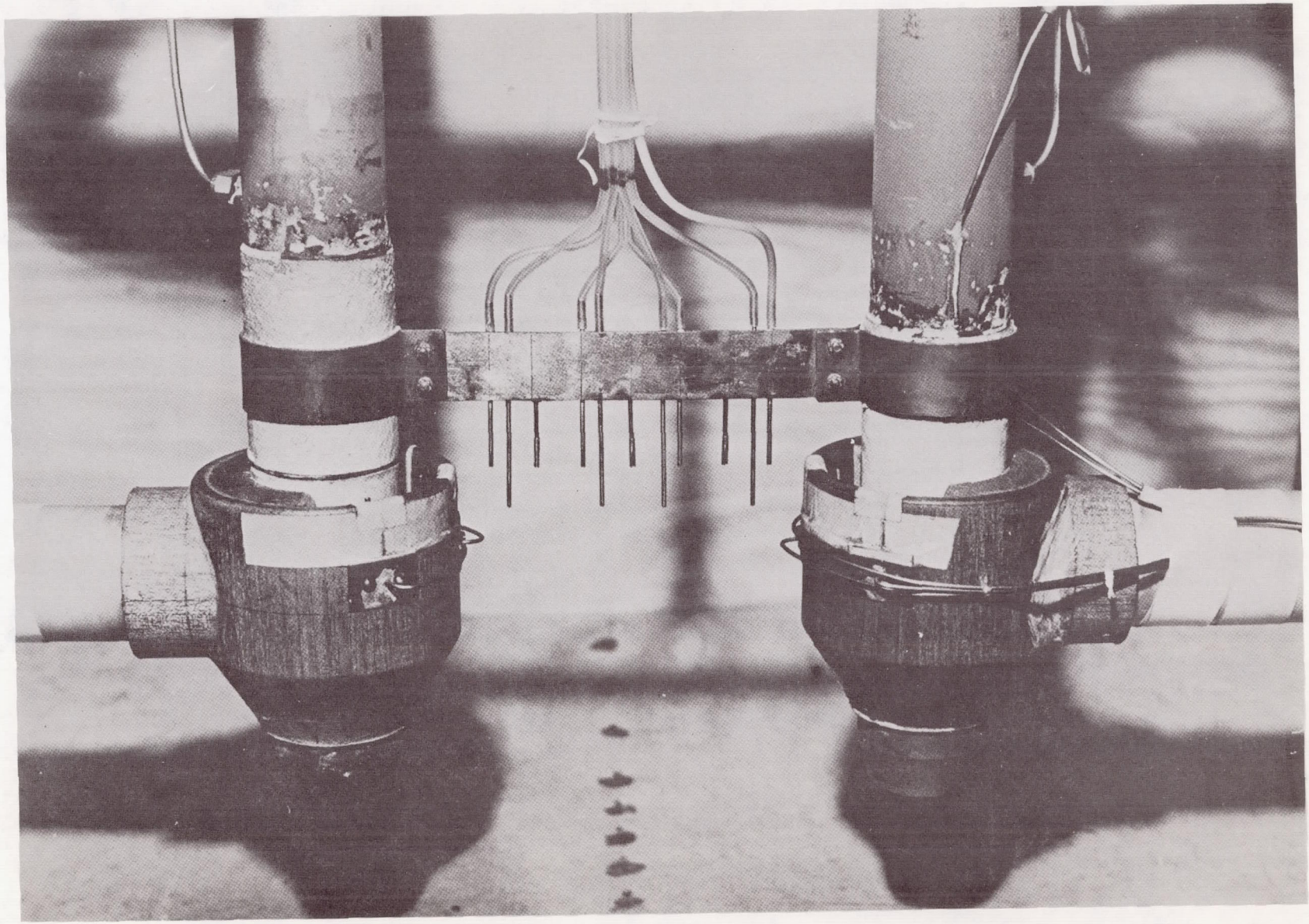

FIGURE 6 UPWASH RAKE MOUNTED BETWEEN NOZZLE-INLET ASSEMBLIES

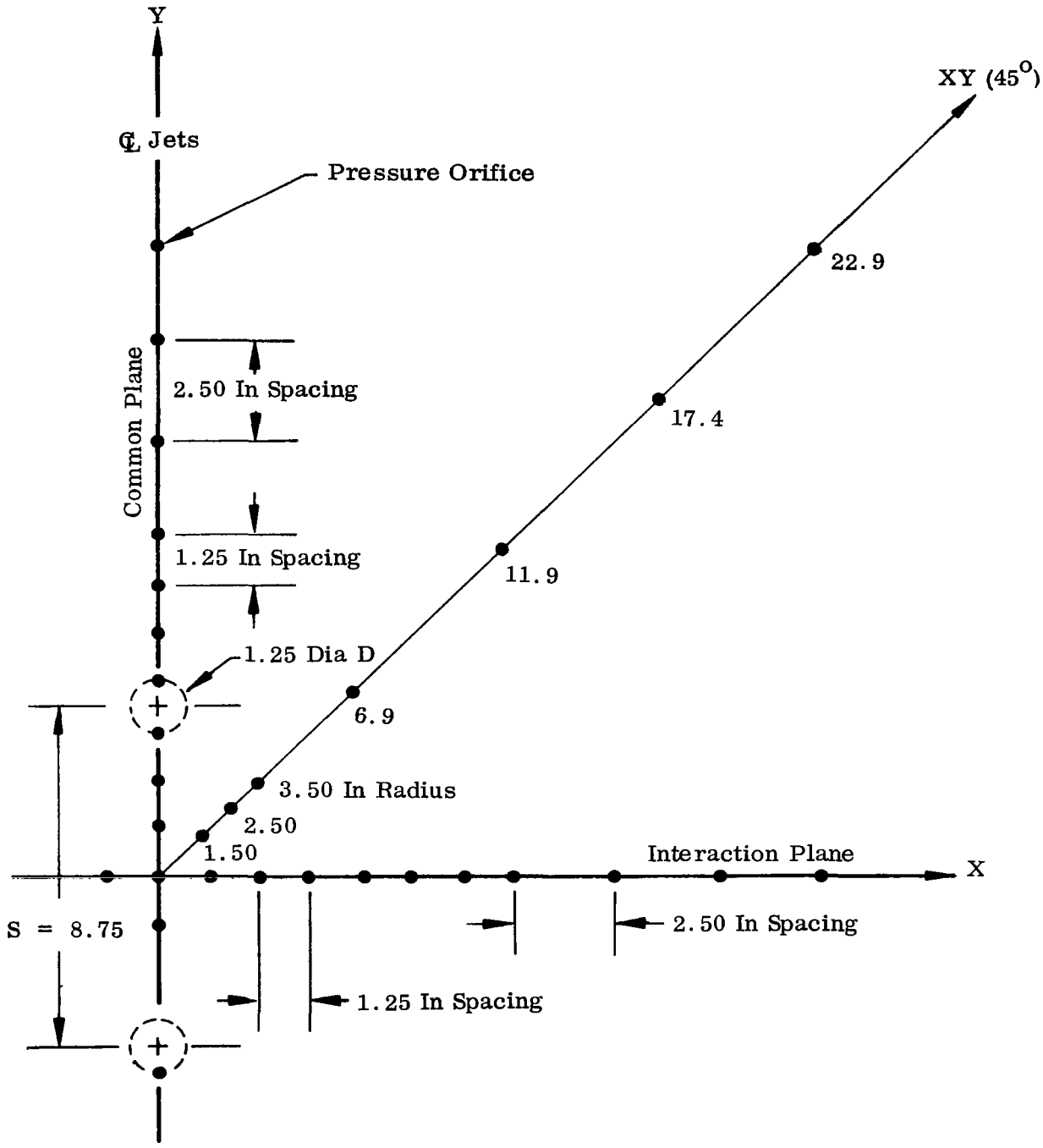

FIGURE 7. GROUND PLANE PRESSURE-TAP PATTERN

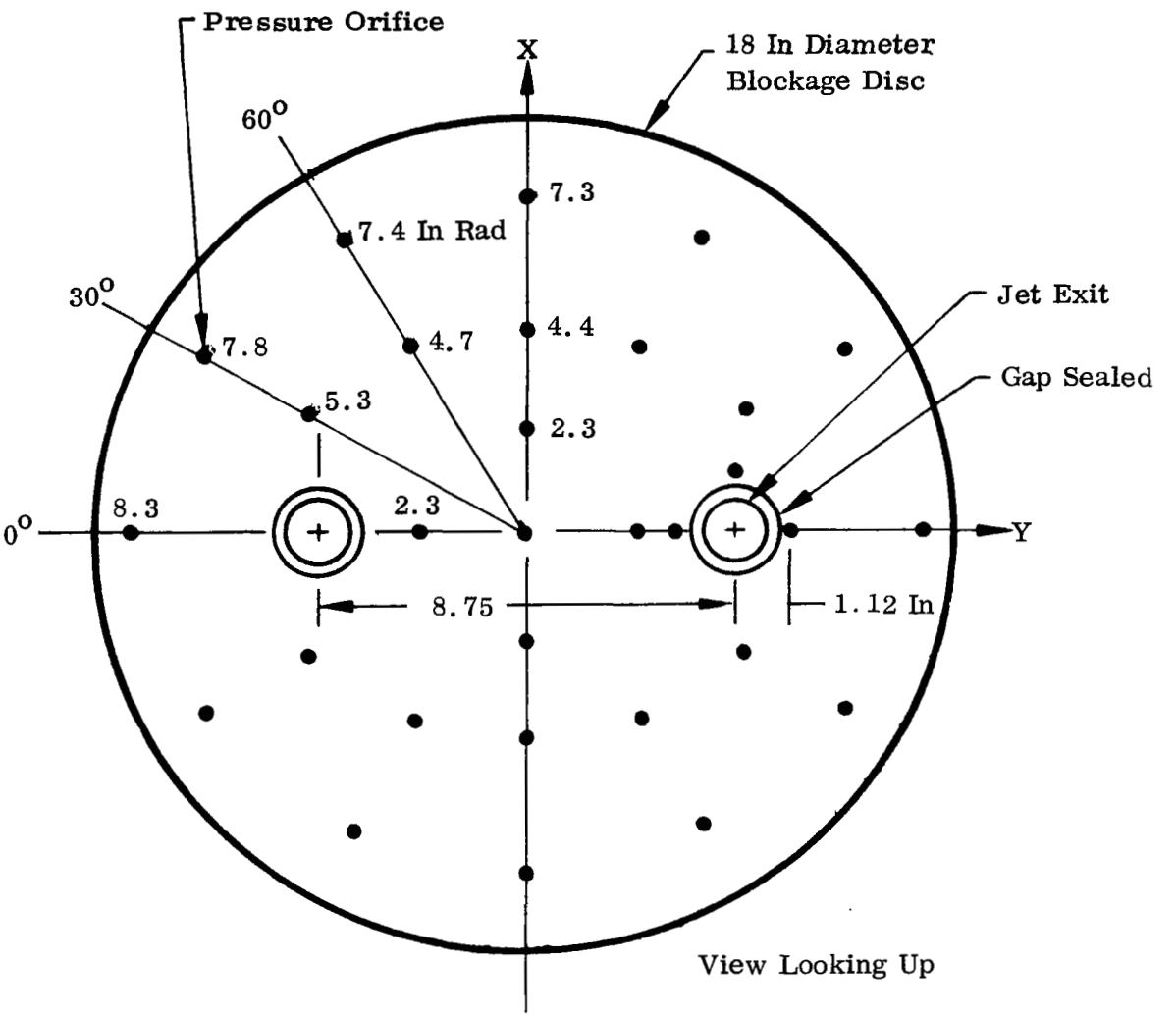

FIGURE 8. PRESSURE-TAP PATTERN ON LOWER SURFACE OF 18 INCH BLOCKAGE DISC

TABLE OF
PROBE HEIGHTS h

h ~IN	P_T	P_S	T
0.05	X		
0.10	X	X	X
0.20	X		
0.30	X	X	X
0.40	X		
0.60	X	X	X
1.00	X		
1.60	X	X	X
2.40	X		
3.40	X	X	X
4.60	X		
6.00	X	X	X

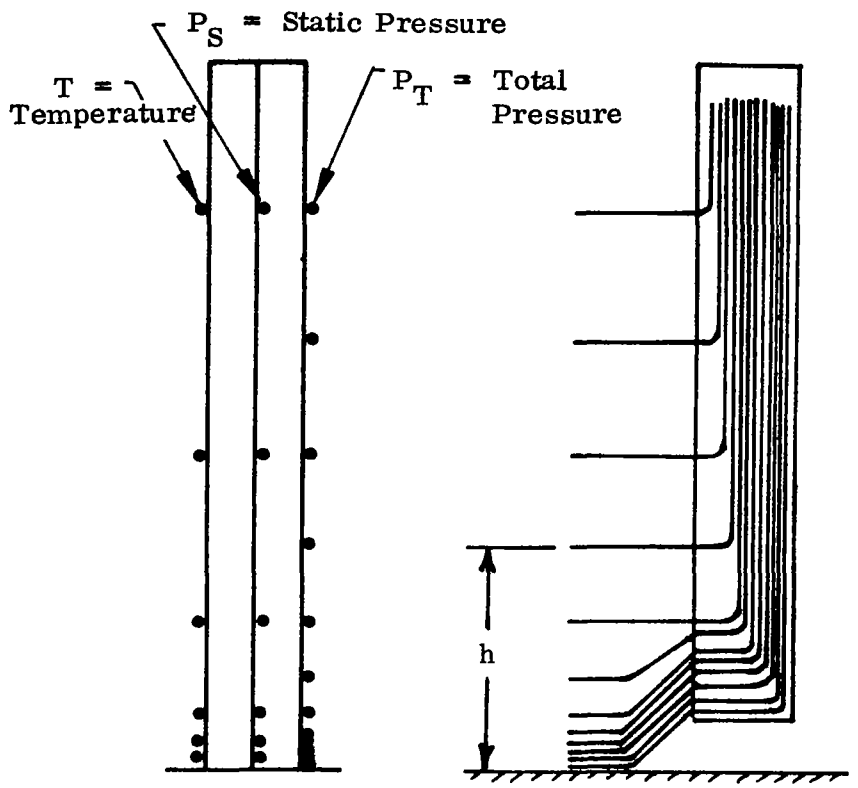

FIGURE 9. GROUND-JET PRESSURE/TEMPERATURE RAKE

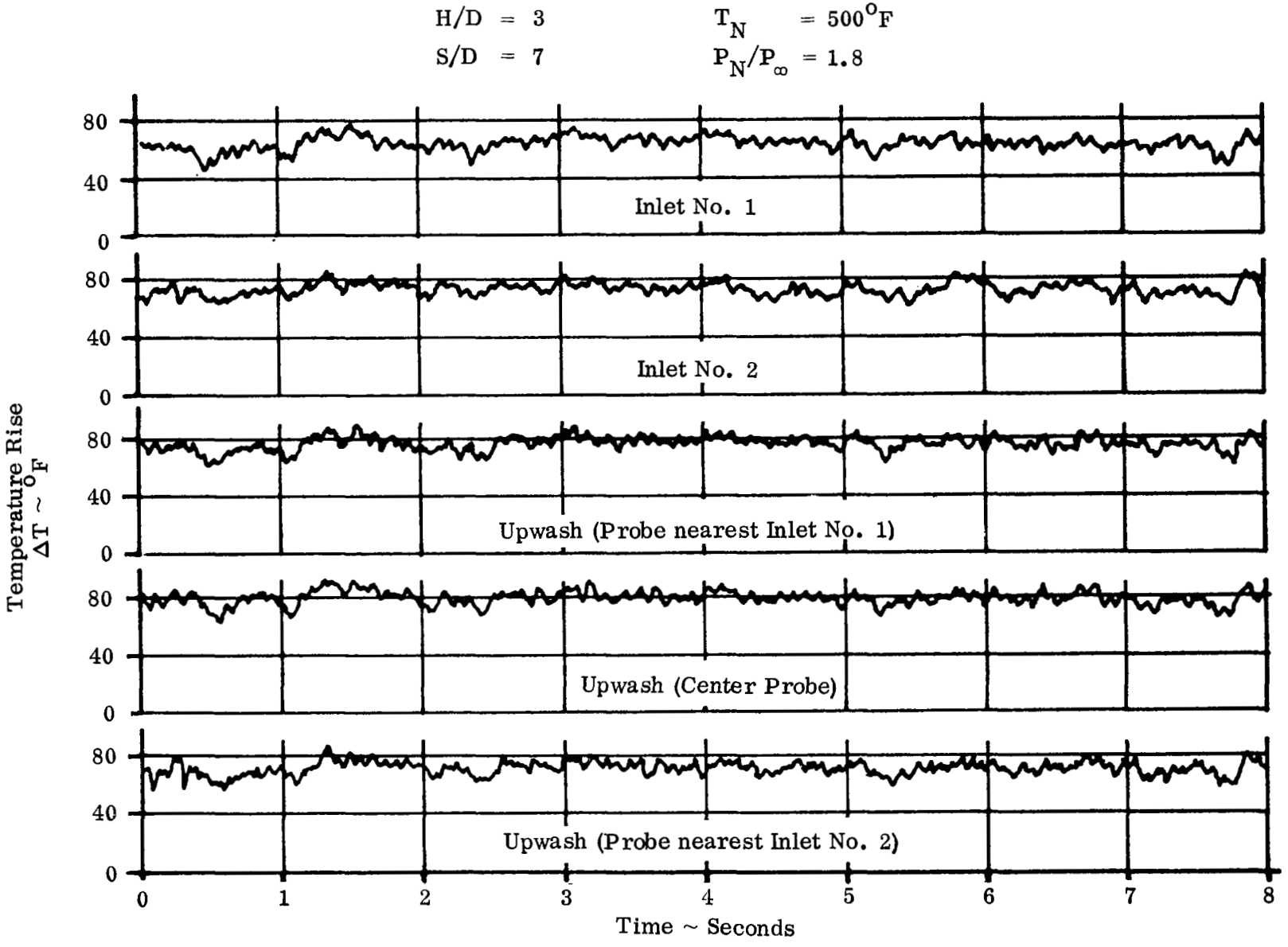

FIGURE 10. TYPICAL INLET AND UPWASH TEMPERATURE HISTORY

H/D = 3 T_N = 500°F

S/D = 7 P_N/P_∞ = 1.8

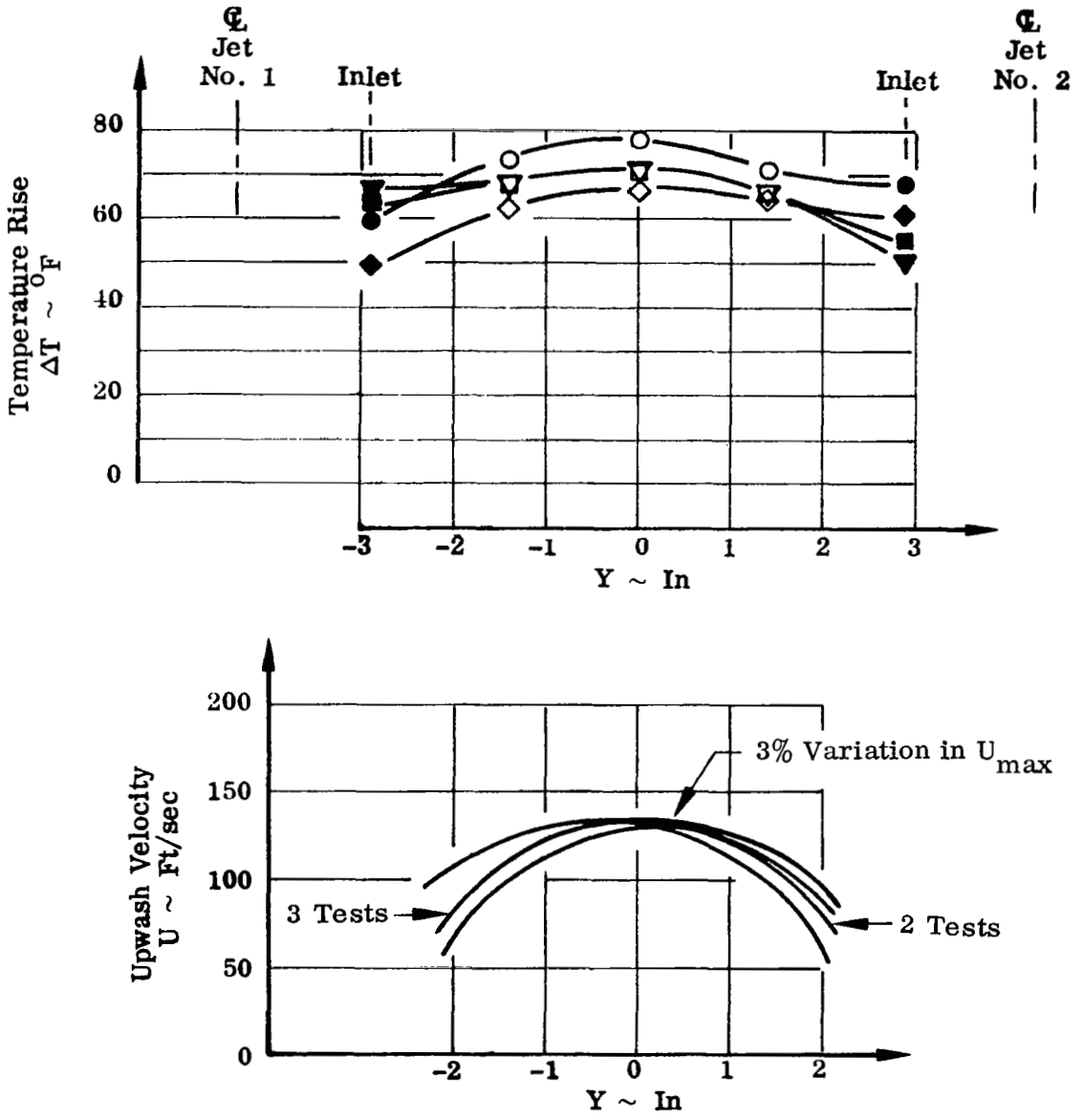

FIGURE 11. REPEATABILITY OF UPWASH TEMPERATURE RISE AND VELOCITY FOR FIVE TESTS

S/D = 7 T_N = 500°F

P_N/P_∞ = 1.8

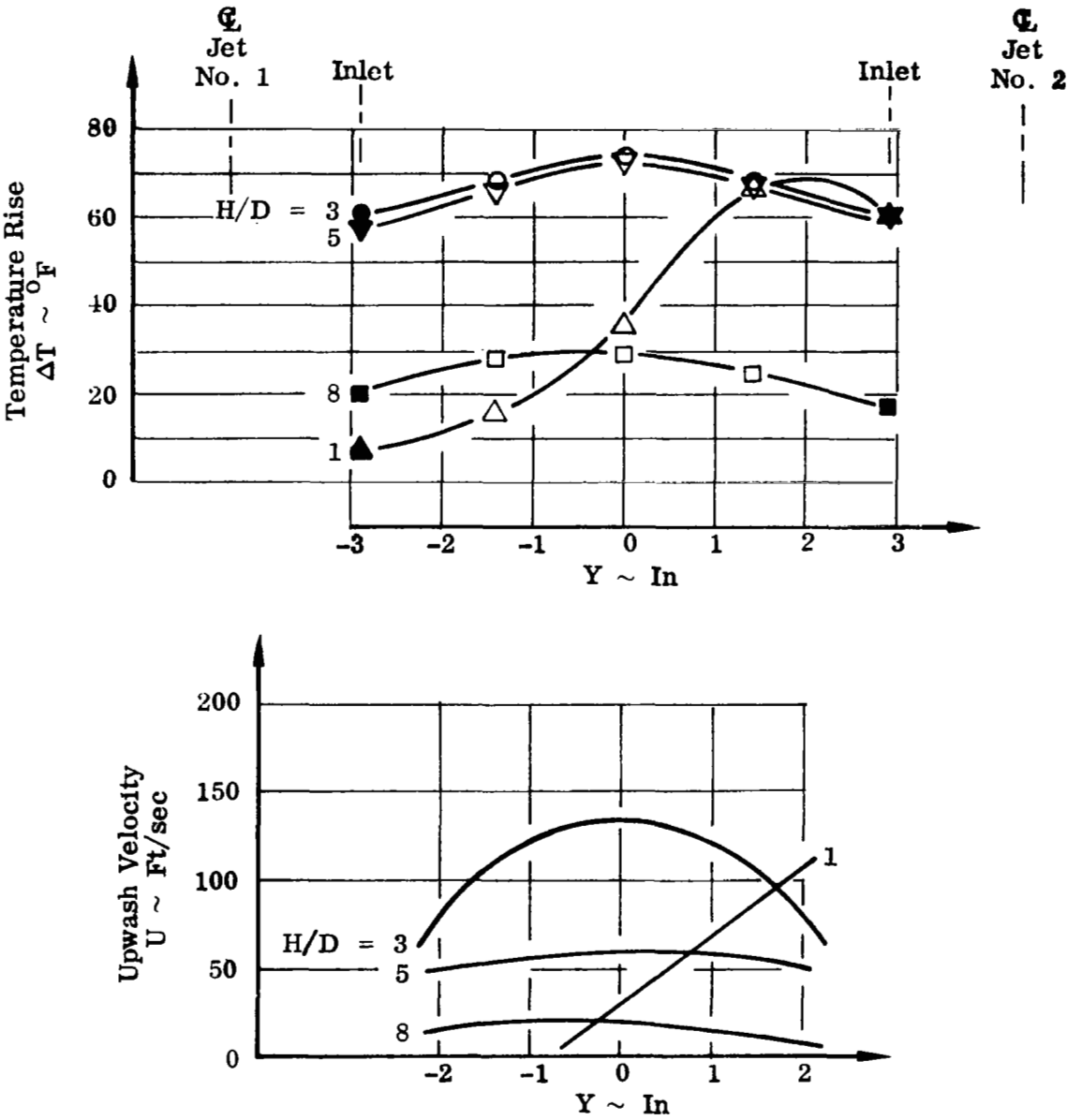

FIGURE 12. EFFECT OF NOZZLE HEIGHT RATIO H/D ON UPWASH TEMPERATURE RISE AND VELOCITY

H/D = 3 $T_N = 500^{\circ}F$

$P_N/P_\infty = 1.8$

Note: Inlet Locations for S/D = 4, 10, and 15 are not to scale

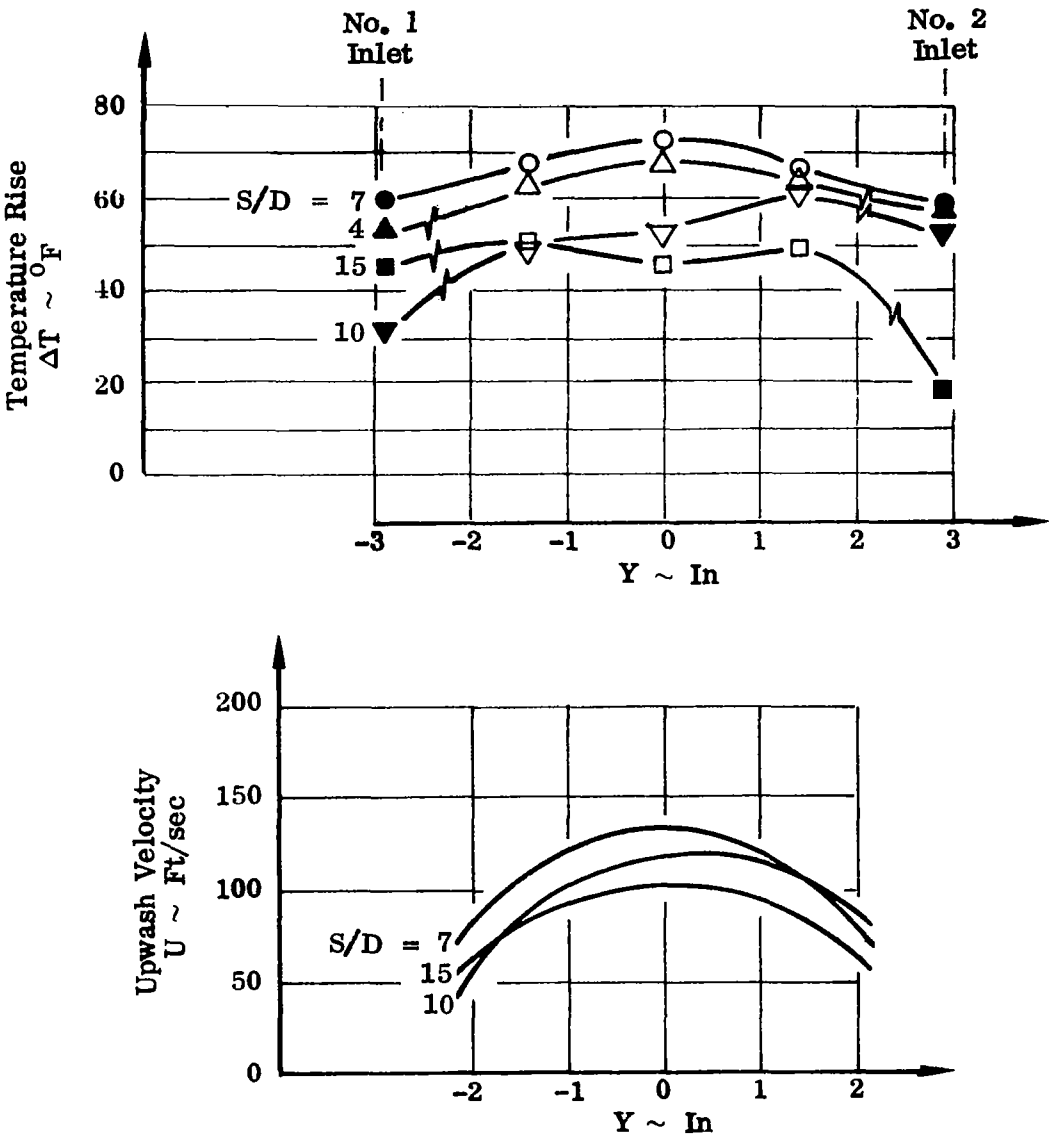

FIGURE 13. EFFECT OF NOZZLE SPACING RATIO S/D ON UPWASH TEMPERATURE RISE AND VELOCITY

$T_N = 500^{\circ}F$

$P_N/P_\infty = 1.8$

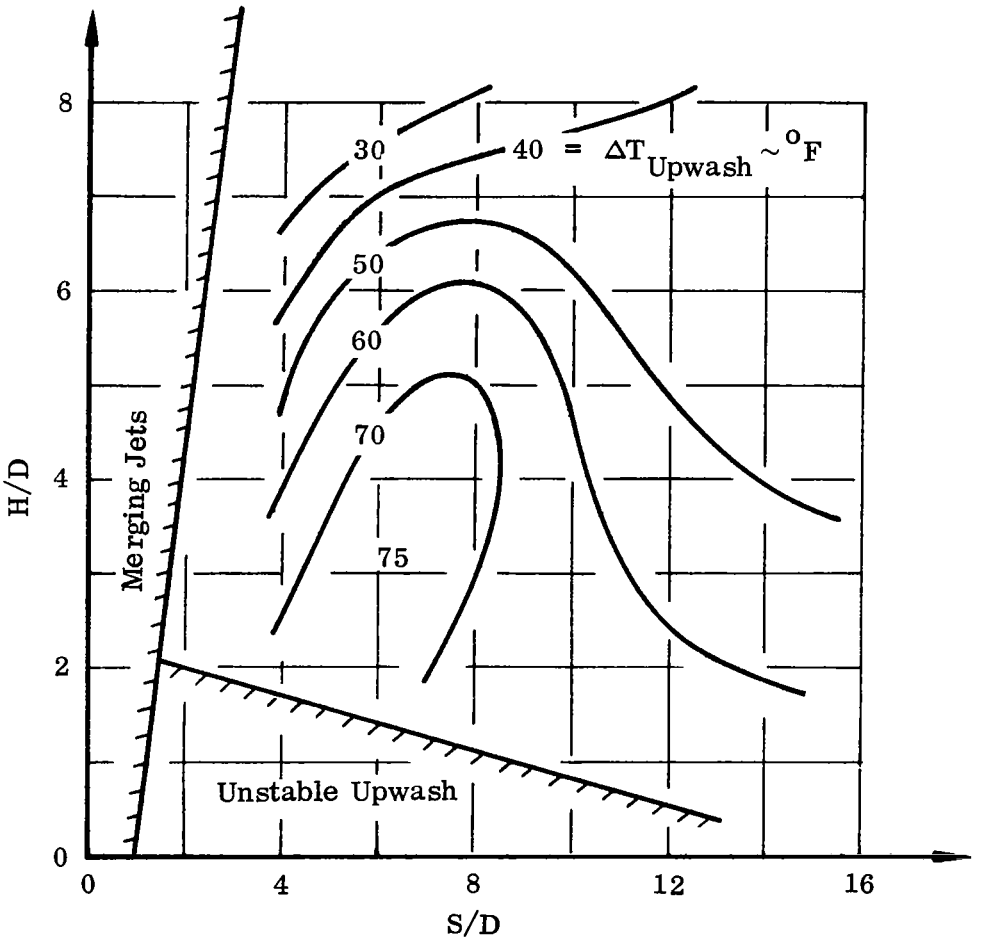

FIGURE 14. MAP OF MAXIMUM UPWASH TEMPERATURE RISE VS. NOZZLE HEIGHT AND SPACING RATIOS

$T_N = 500^oF$

$P_N/P_\infty = 1.8$

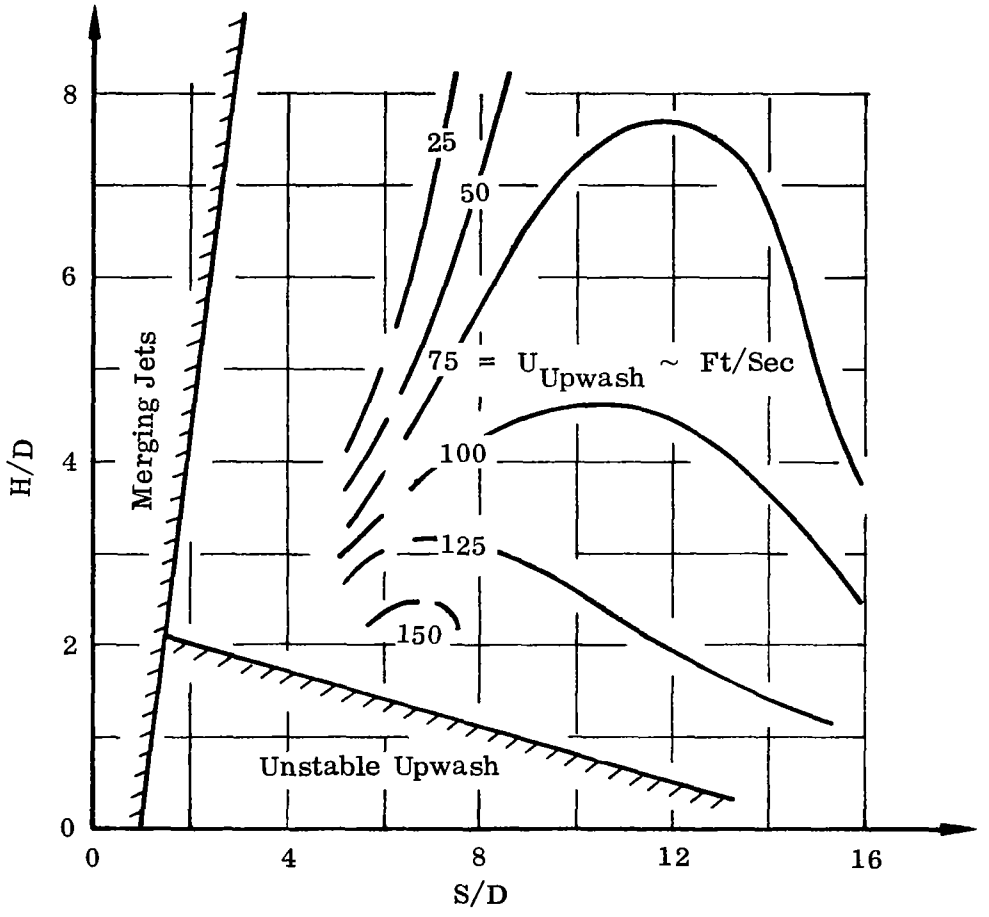

FIGURE 15. MAP OF MAXIMUM UPWASH VELOCITY VS. NOZZLE HEIGHT AND SPACING RATIOS

$T_N = 500^oF$

$P_N/P_\infty = 1.8$

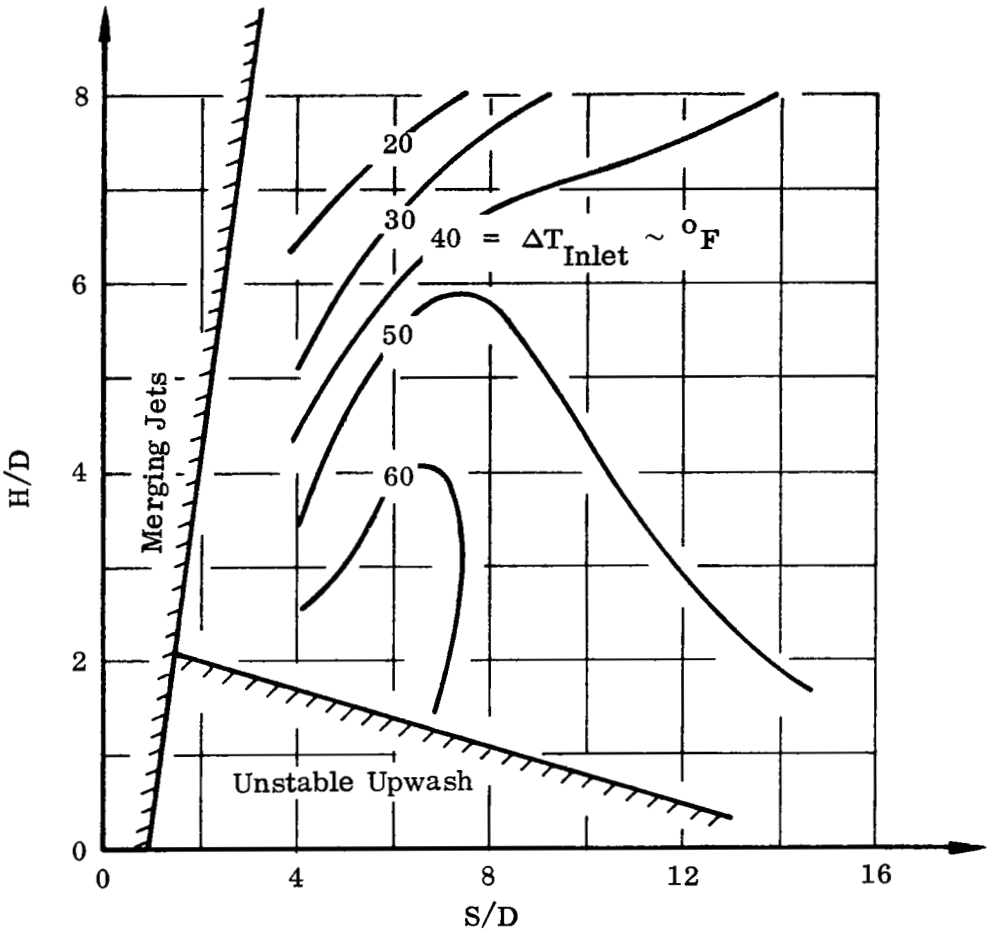

FIGURE 16. MAP OF INLET TEMPERATURE RISE VS. NOZZLE HEIGHT AND SPACING RATIOS

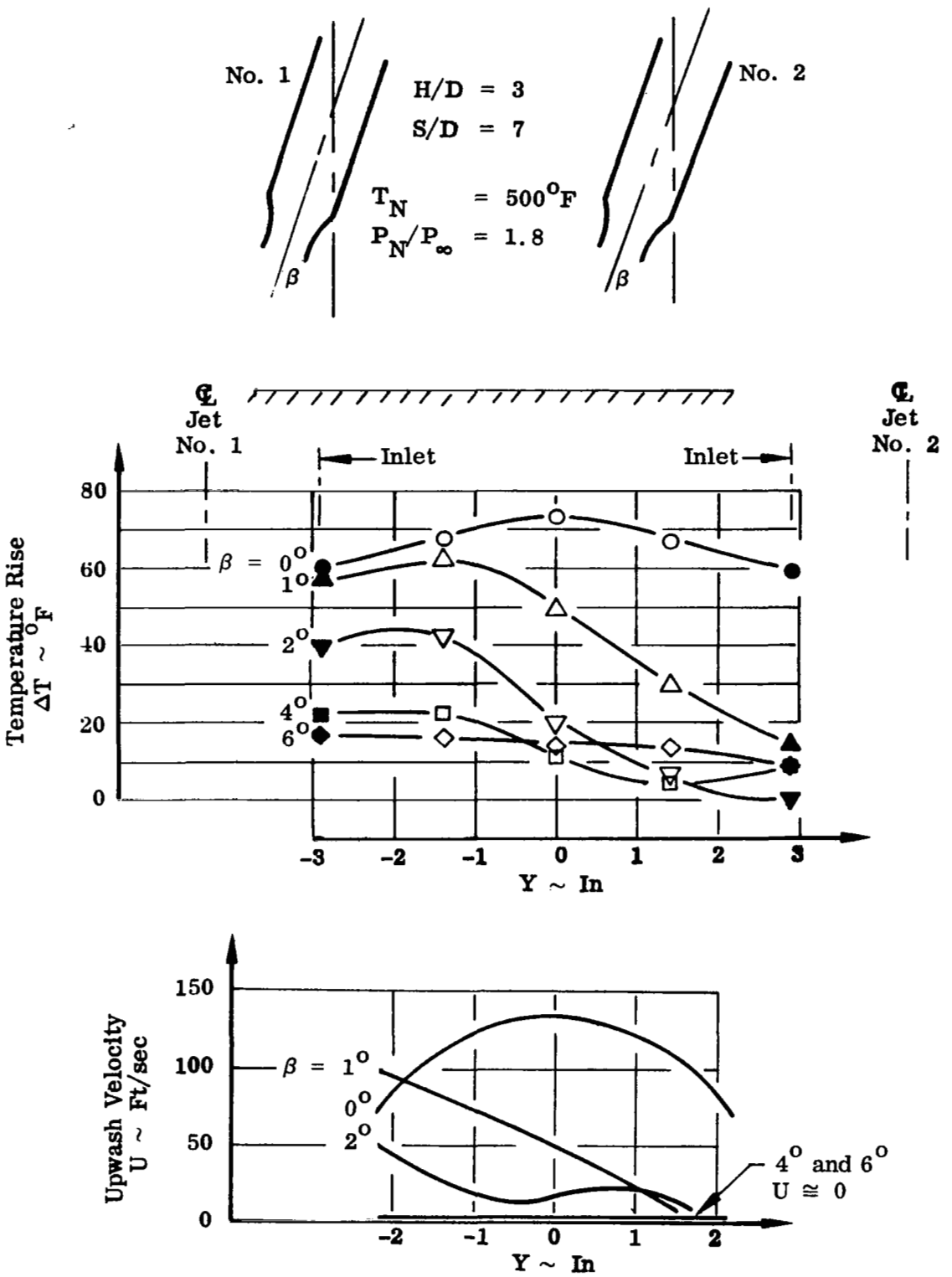

FIGURE 17. EFFECT OF NOZZLE CANT ANGLE β ON UPWASH TEMPERATURE RISE AND VELOCITY

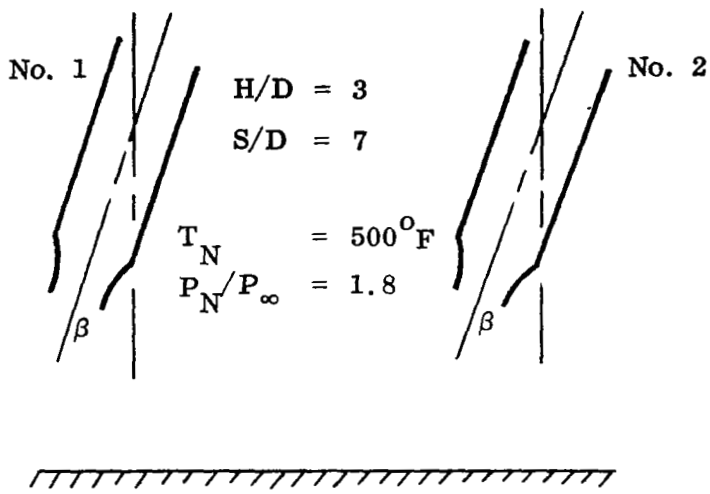

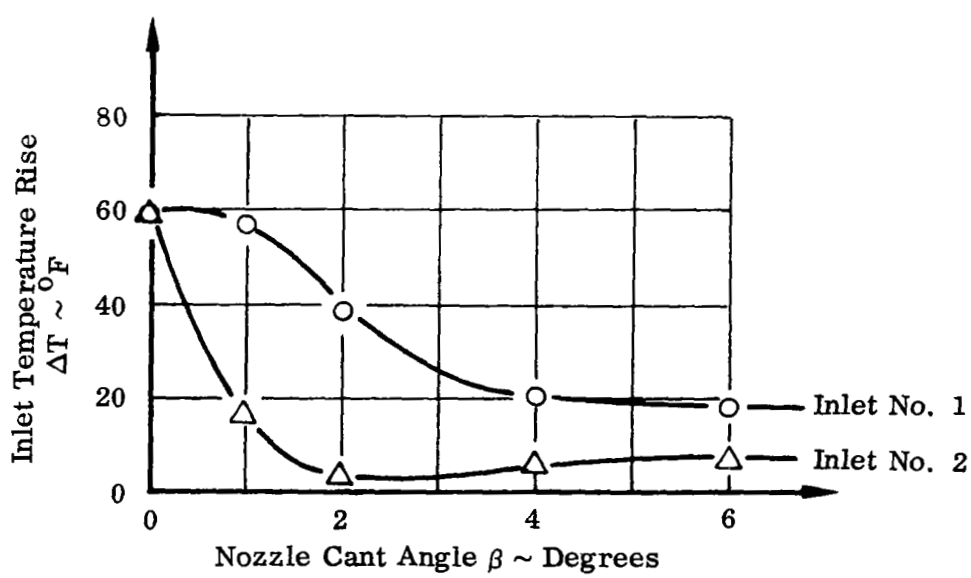

FIGURE 18. INLET TEMPERATURE RISE VS NOZZLE CANT ANGLE

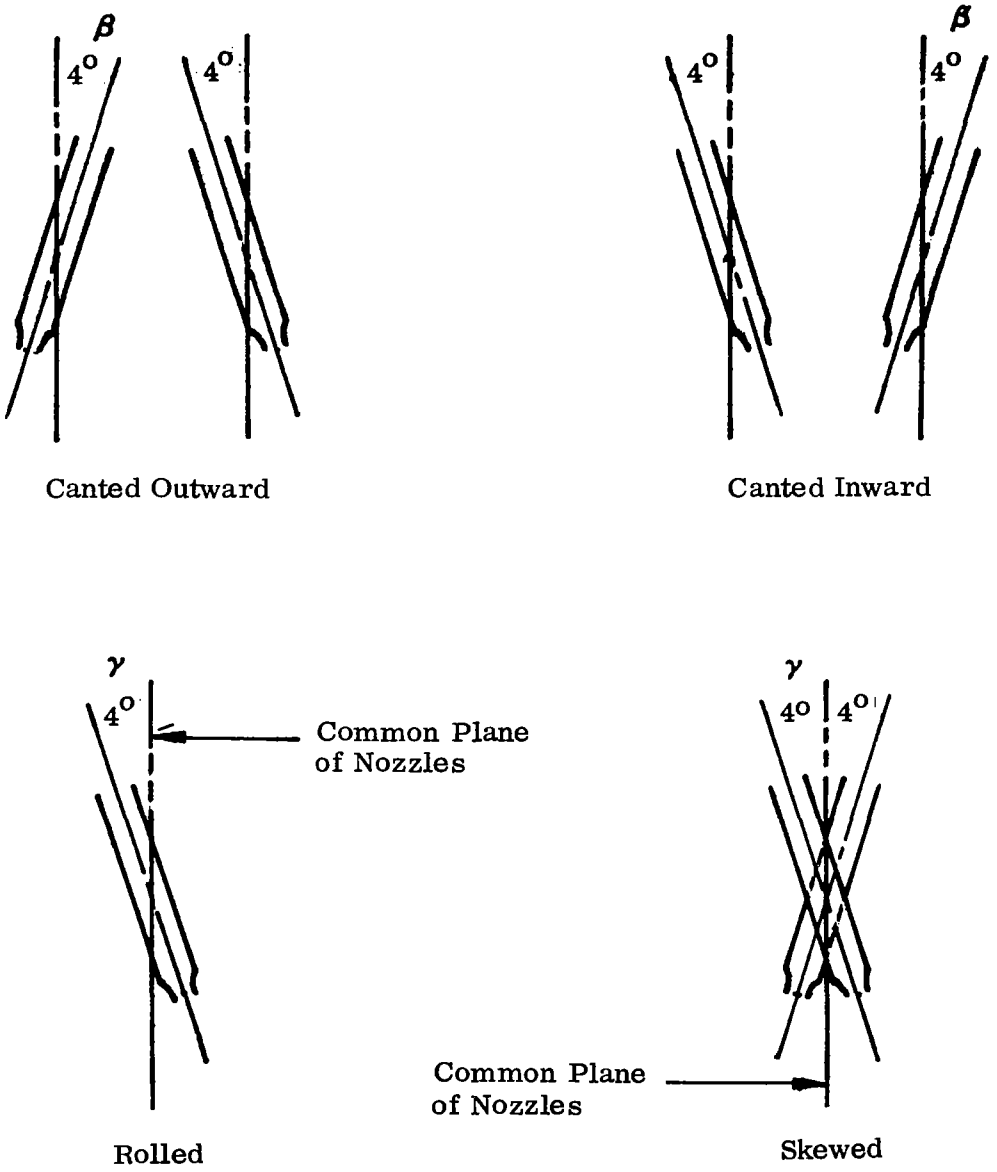

FIGURE 19. NOZZLE CANT CONFIGURATIONS

H/D = 3 T_N = 500°F

S/D = 7 P_N/P = 1.8

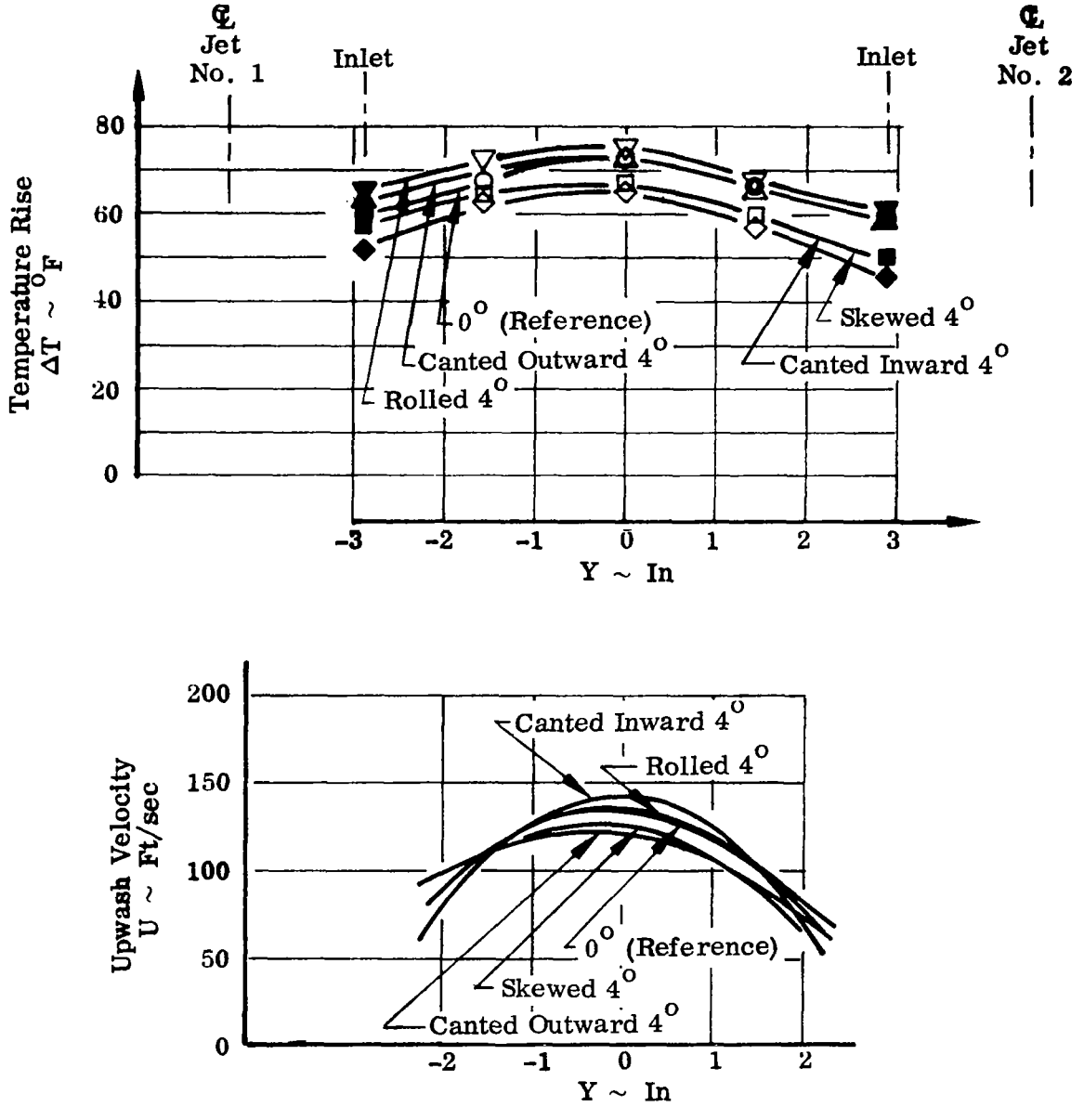

FIGURE 20. EFFECT OF NOZZLE CANT ANGLE ON UPWASH TEMPERATURE RISE AND VELOCITY

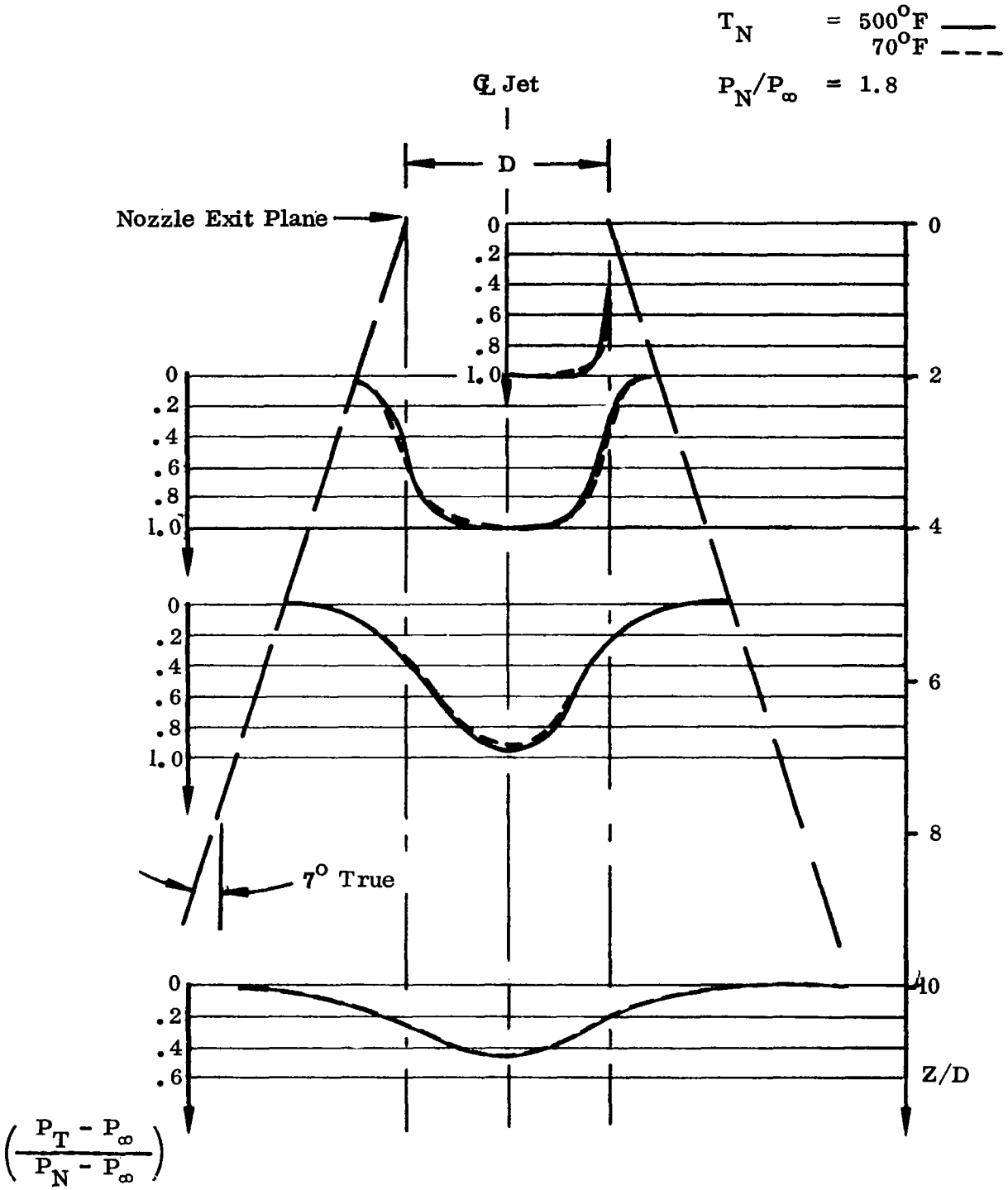

FIGURE 21. DYNAMIC PRESSURE PROFILES - OPEN NOZZLE

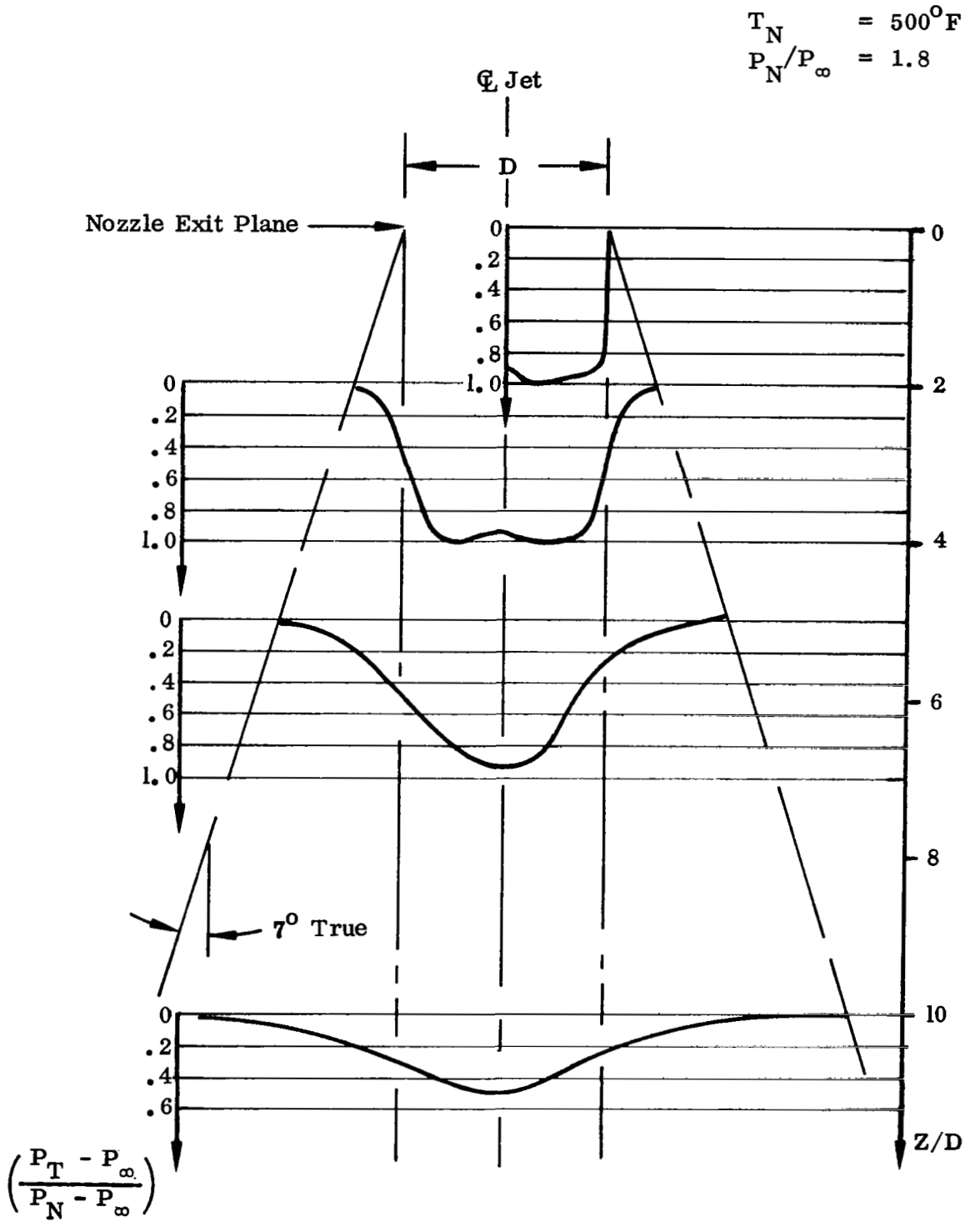

FIGURE 22. DYNAMIC PRESSURE PROFILES - HOT JET, STRAIGHT VANES

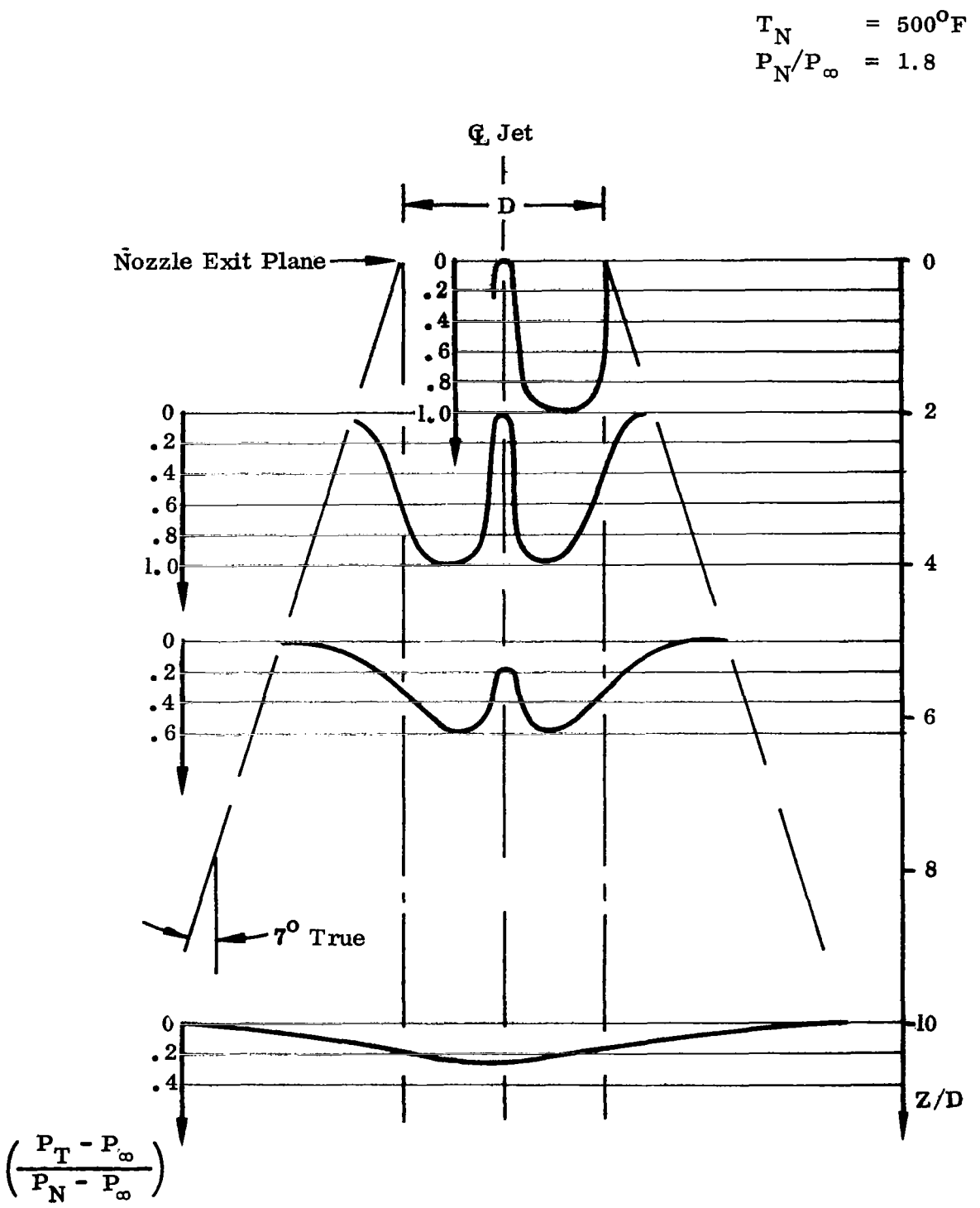

FIGURE 23. DYNAMIC PRESSURE PROFILES - HOT JET, SWIRL VANES

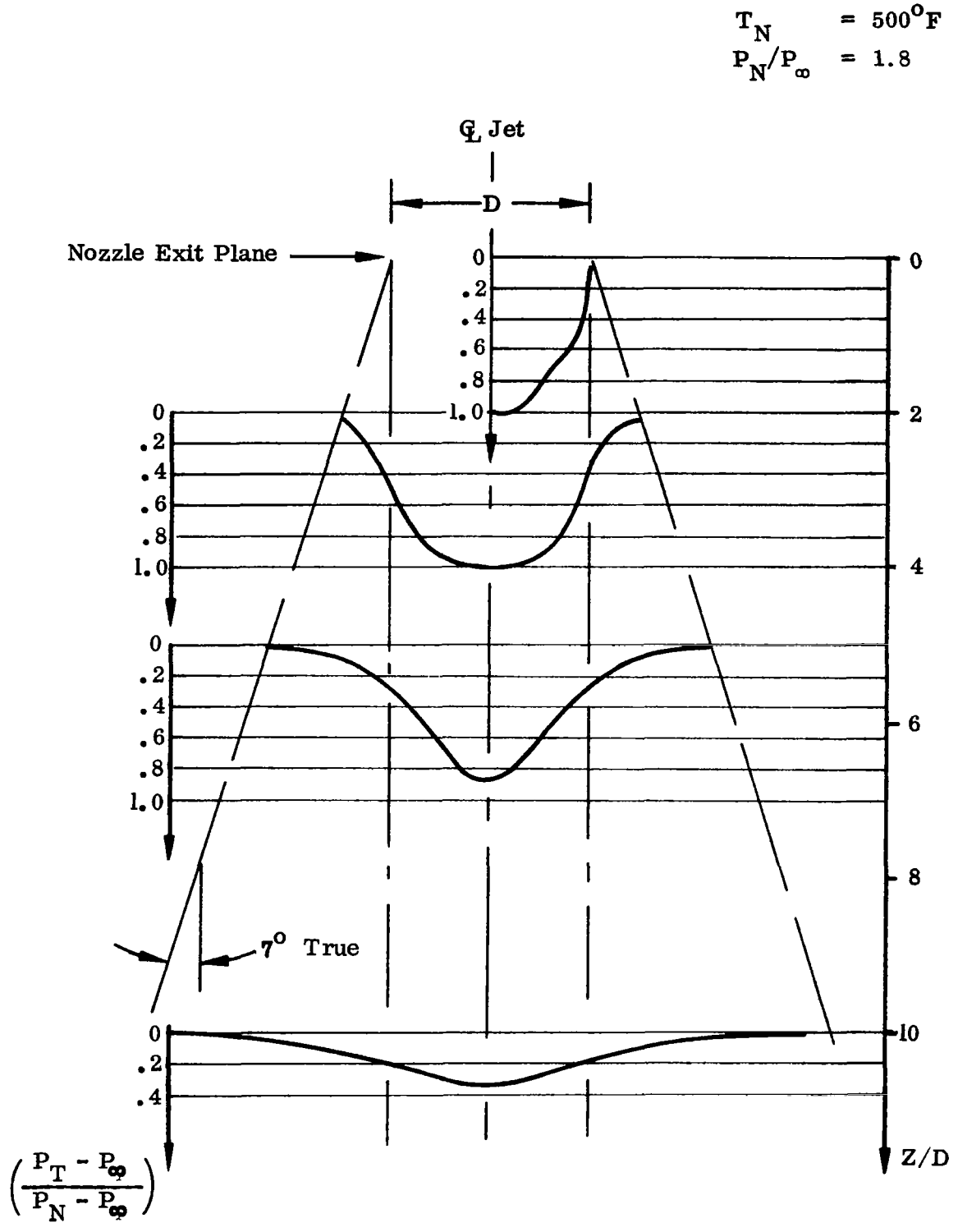

FIGURE 24. DYNAMIC PRESSURE PROFILES - HOT JET, TURBULATOR DISC

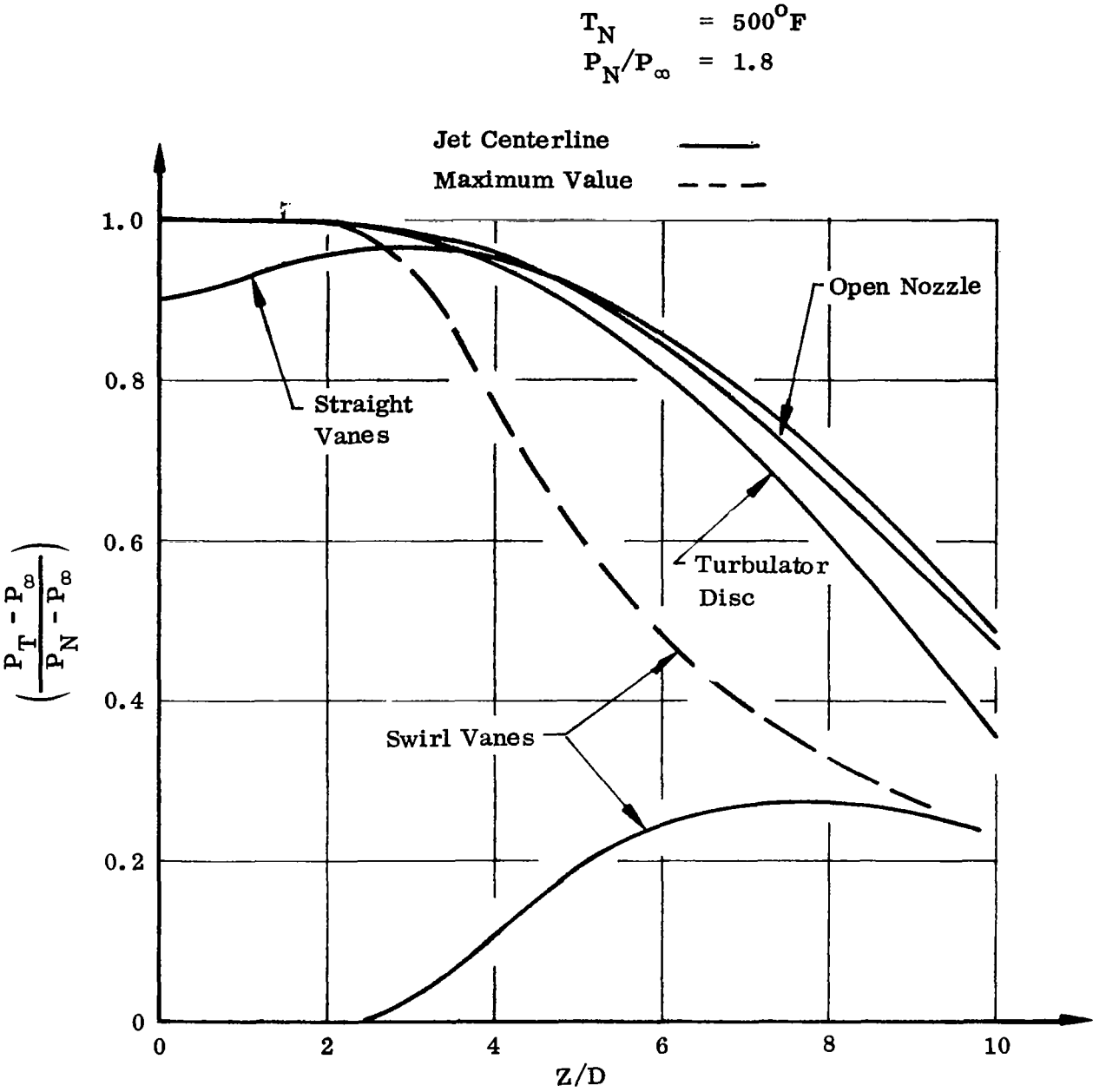

FIGURE 25. JET DYNAMIC PRESSURE DECAY WITH VARIOUS INSERTS ABOVE NOZZLE

$T_N = 500^oF$

$P_N/P_\infty = 1.8$

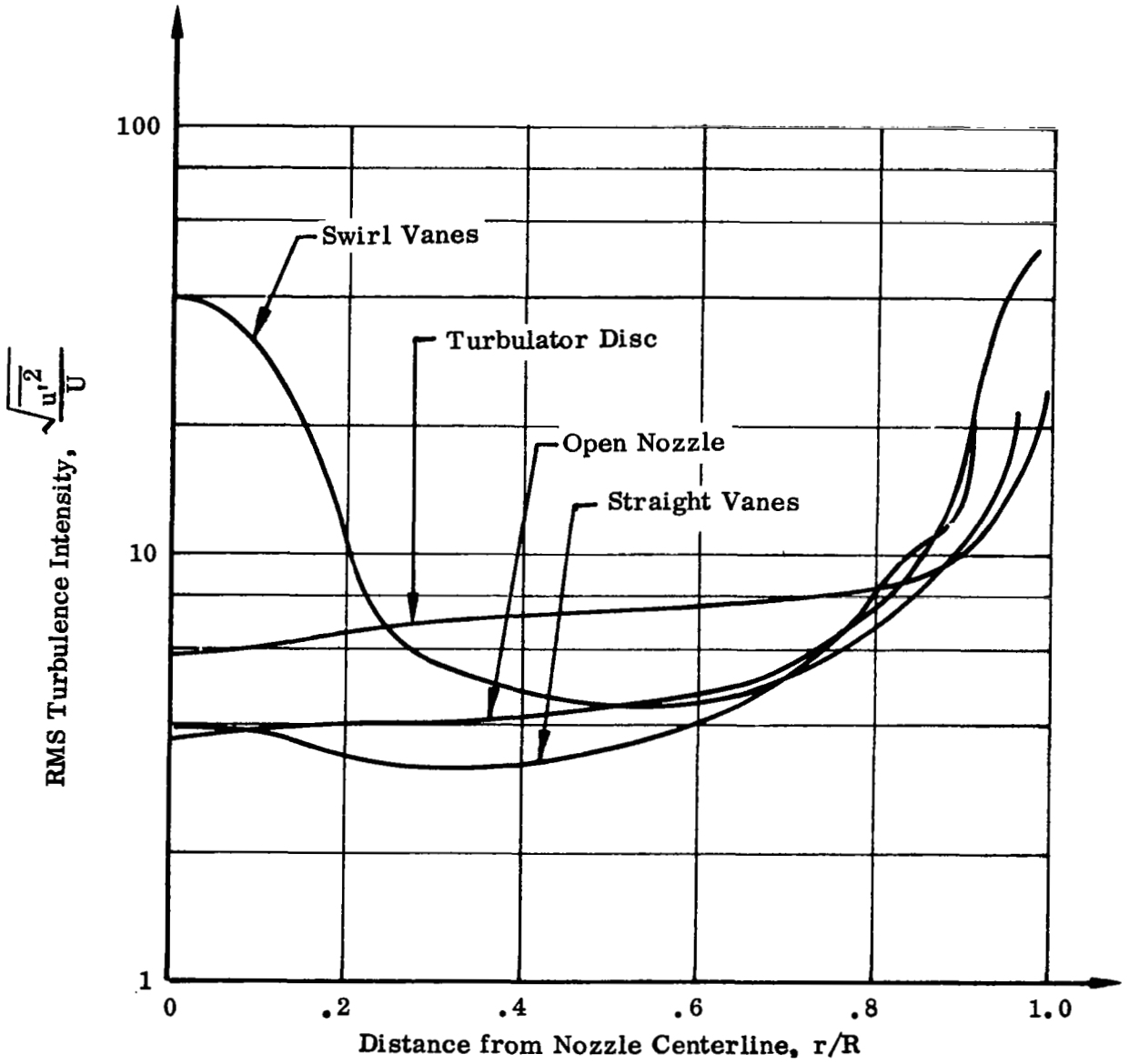

FIGURE 26. RMS TURBULENCE AT NOZZLE EXIT WITH VARIOUS INSERTS ABOVE NOZZLE

H/D = 3, T_N = 500°F

S/D = 7 P_N/P_∞ = 1.8

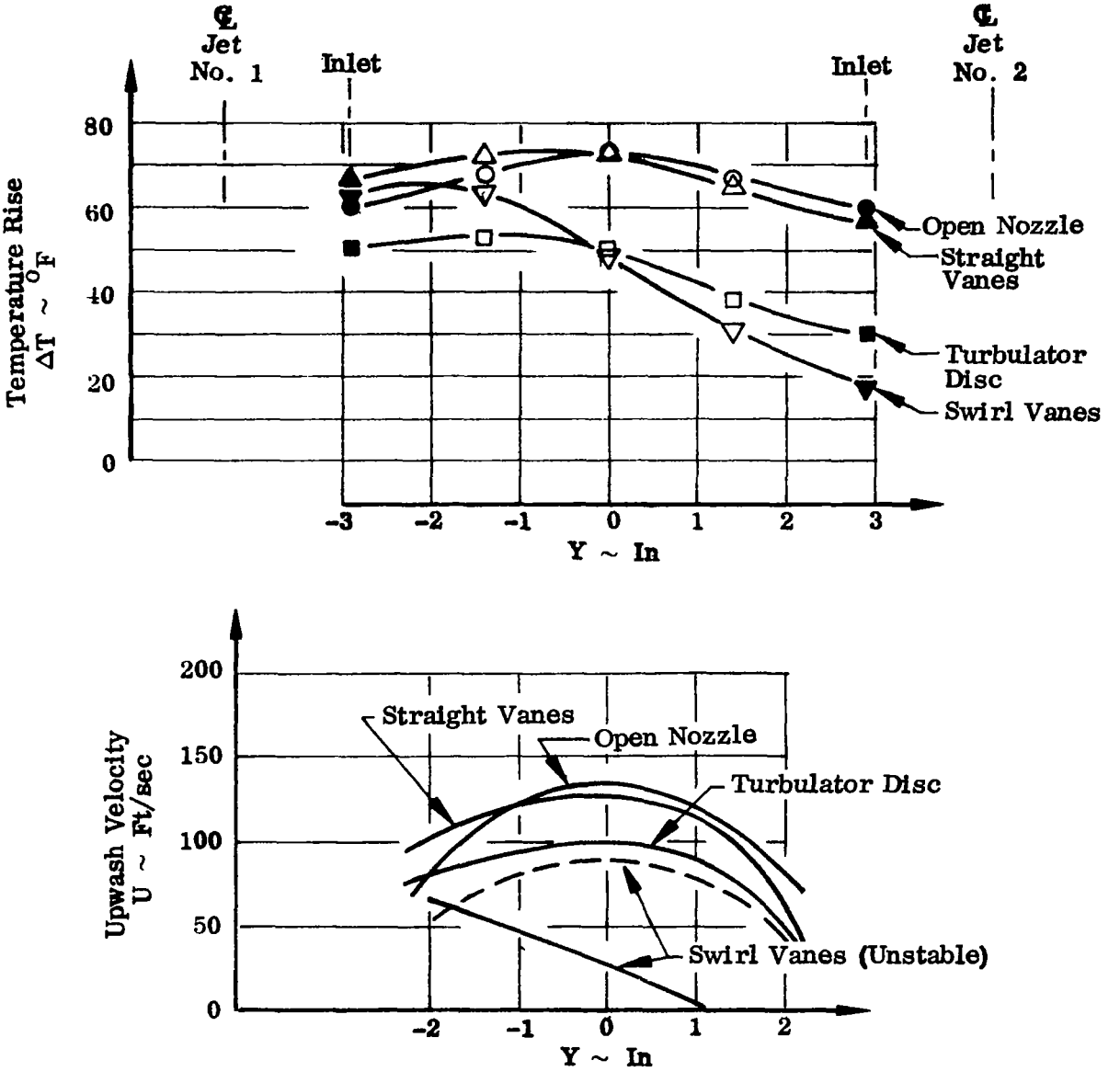

FIGURE 27. EFFECT OF NOZZLE INSERTS ON UPWASH TEMPERATURE RISE AND VELOCITY

S/D = 7 T_N = 500°F

P_N/P_∞ = 1.8

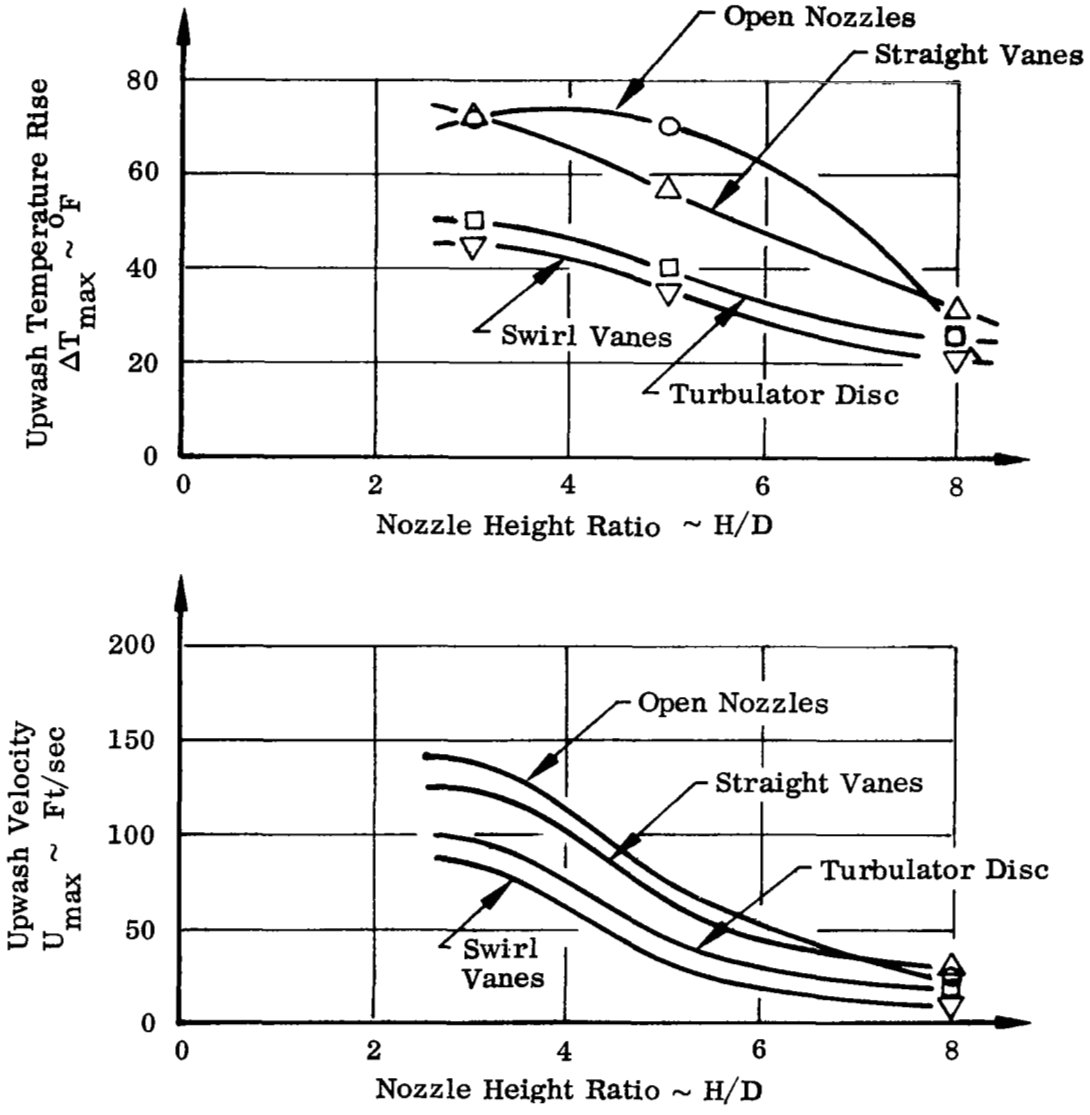

FIGURE 28. EFFECT OF NOZZLE HEIGHT ON UPWASH CHARACTERISTICS MIDWAY BETWEEN INLETS FOR VARIOUS NOZZLE INSERTS

S/D = 7 $T_N = 500^{\circ}F$

$P_N/P_\infty = 1.8$

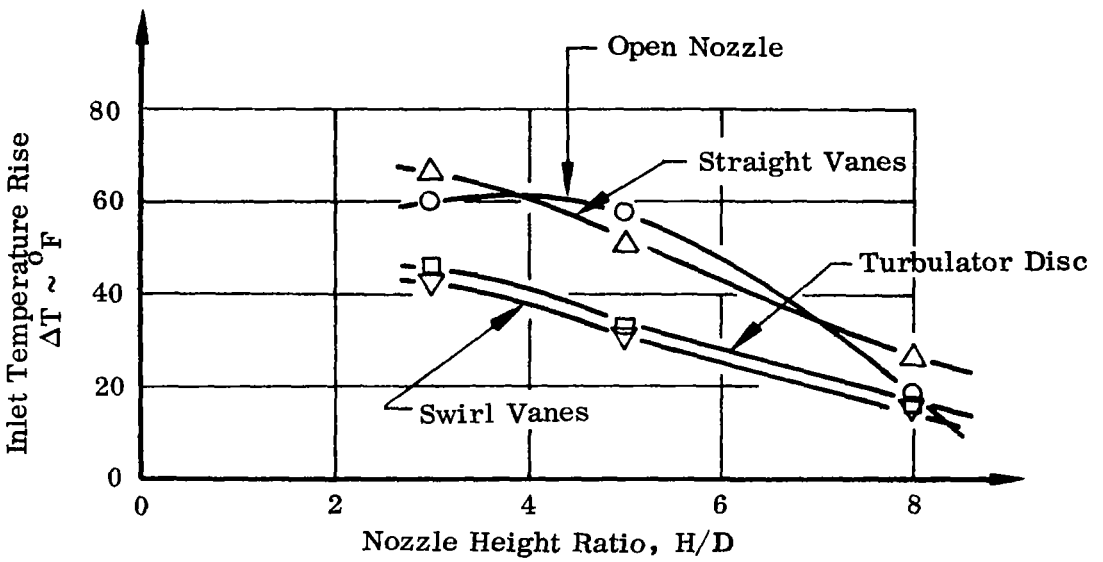

FIGURE 29. EFFECT OF NOZZLE HEIGHT ON INLET TEMPERATURE RISE FOR VARIOUS NOZZLE INSERTS

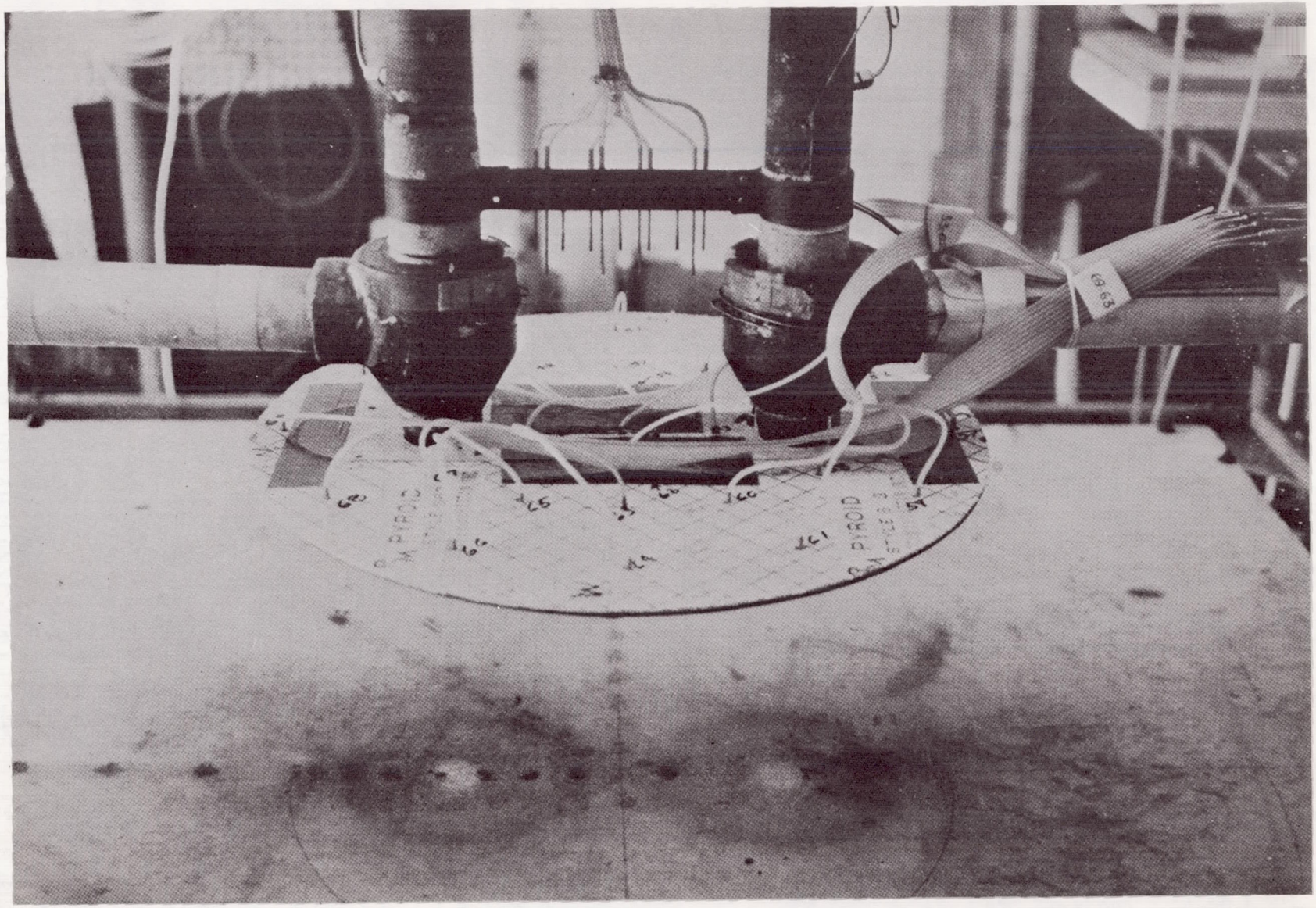

FIGURE 30 18 INCH BLOCKAGE DISC INSTALLATION

$T_N = 500^oF$

$P_N/P_\infty = 1.8$

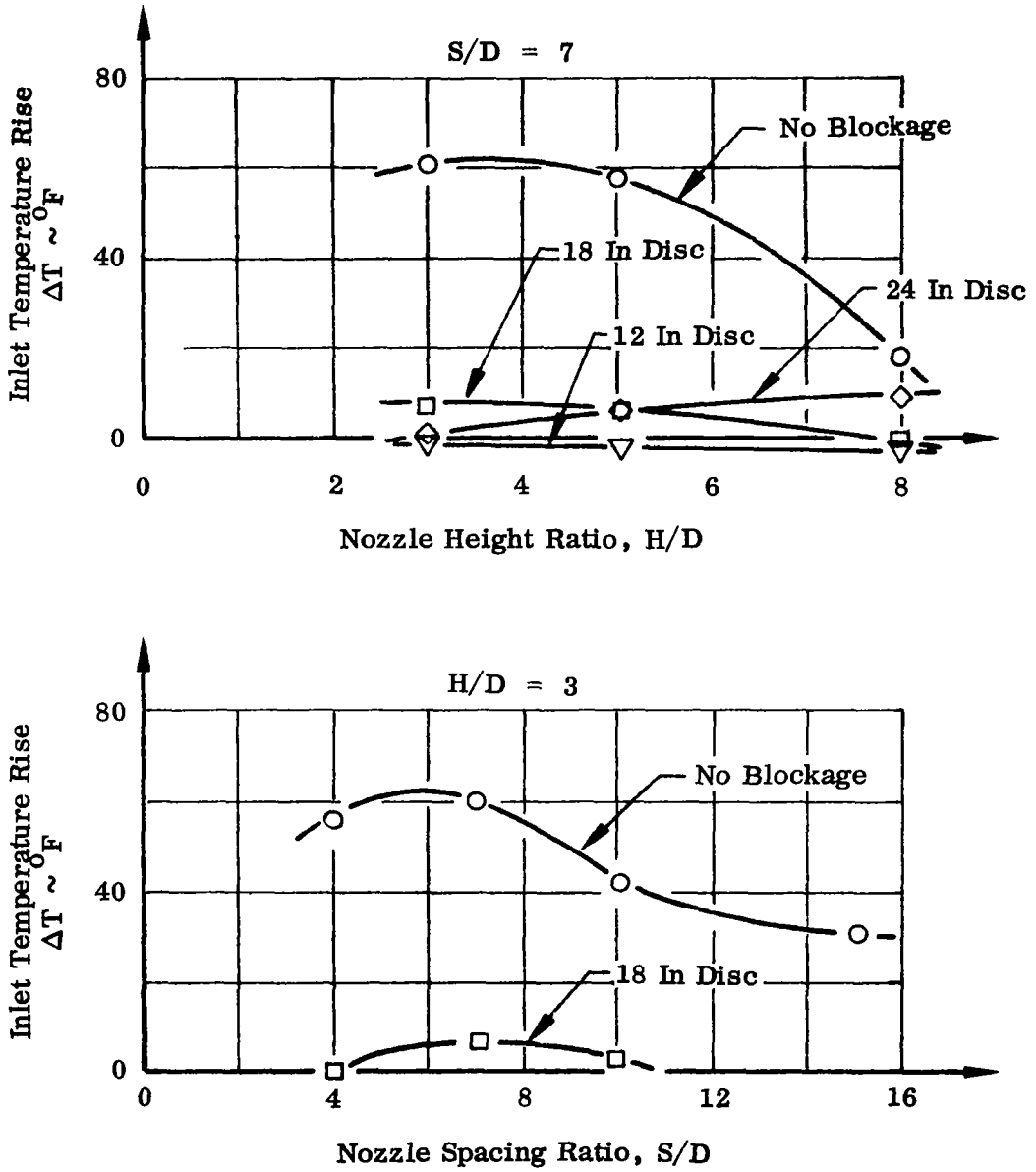

FIGURE 31. EFFECT OF UPWASH BLOCKAGE SURFACES ON INLET TEMPERATURE RISE

H/D = 3 P_N/P_∞ = 1.8

S/D = 7

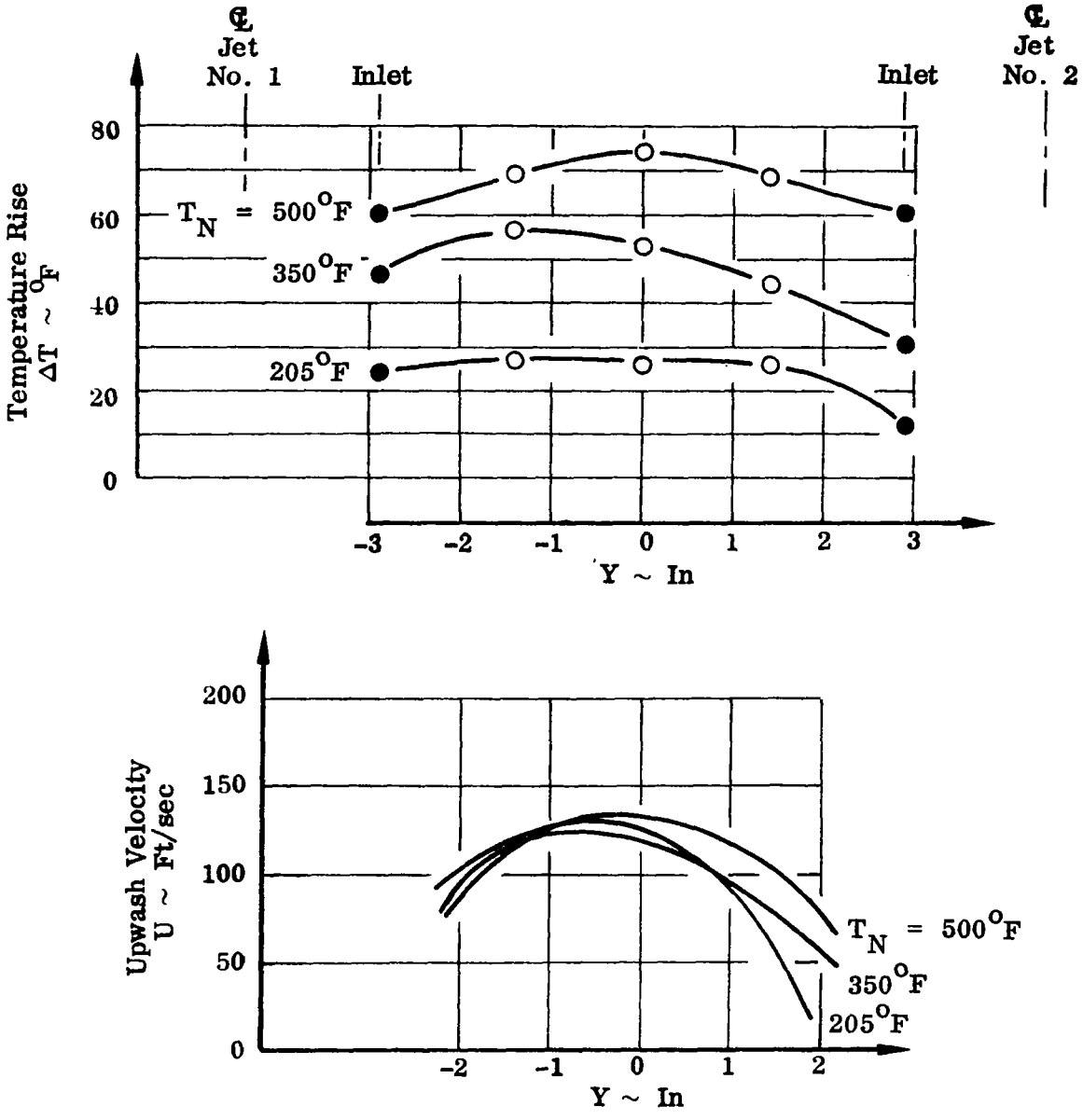

FIGURE 32. EFFECT OF NOZZLE TEMPERATURE LEVEL ON UPWASH TEMPERATURE RISE AND VELOCITY

H/D = 3 P_N/P_∞ = 1.8

S/D = 7

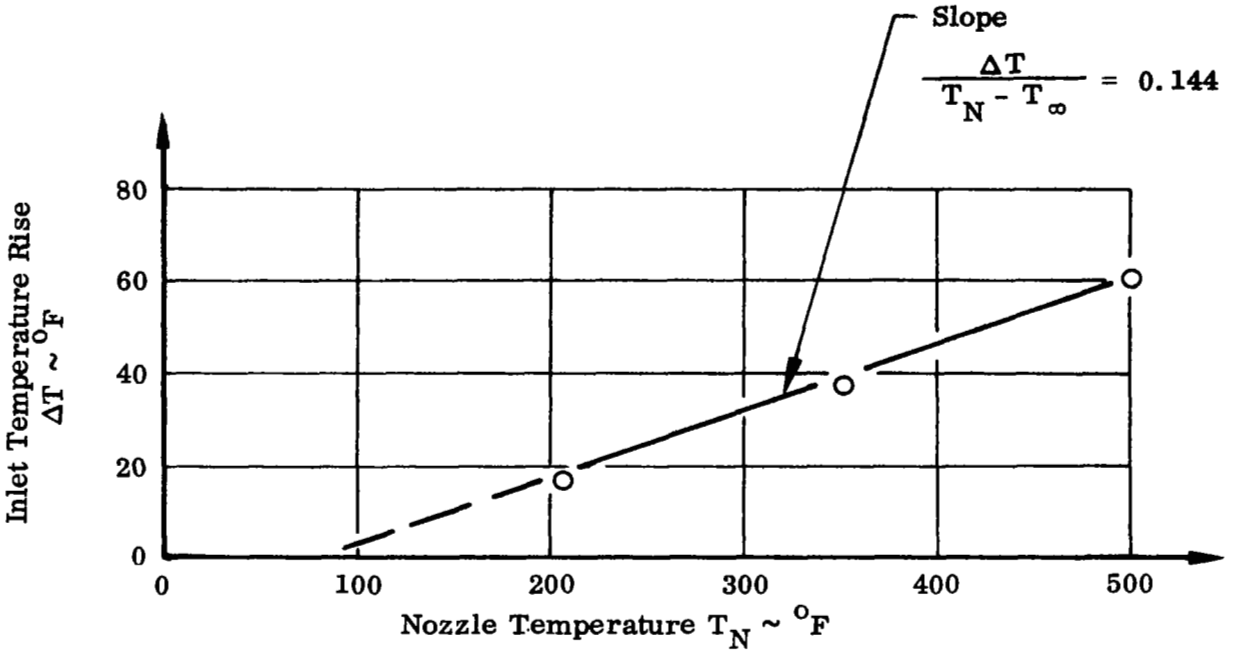

FIGURE 33. EFFECT OF NOZZLE TEMPERATURE LEVEL ON INLET TEMPERATURE RISE

H/D = 3 T_{N_2} = 500°F

S/D = 7 P_N/P_∞ = 1.8

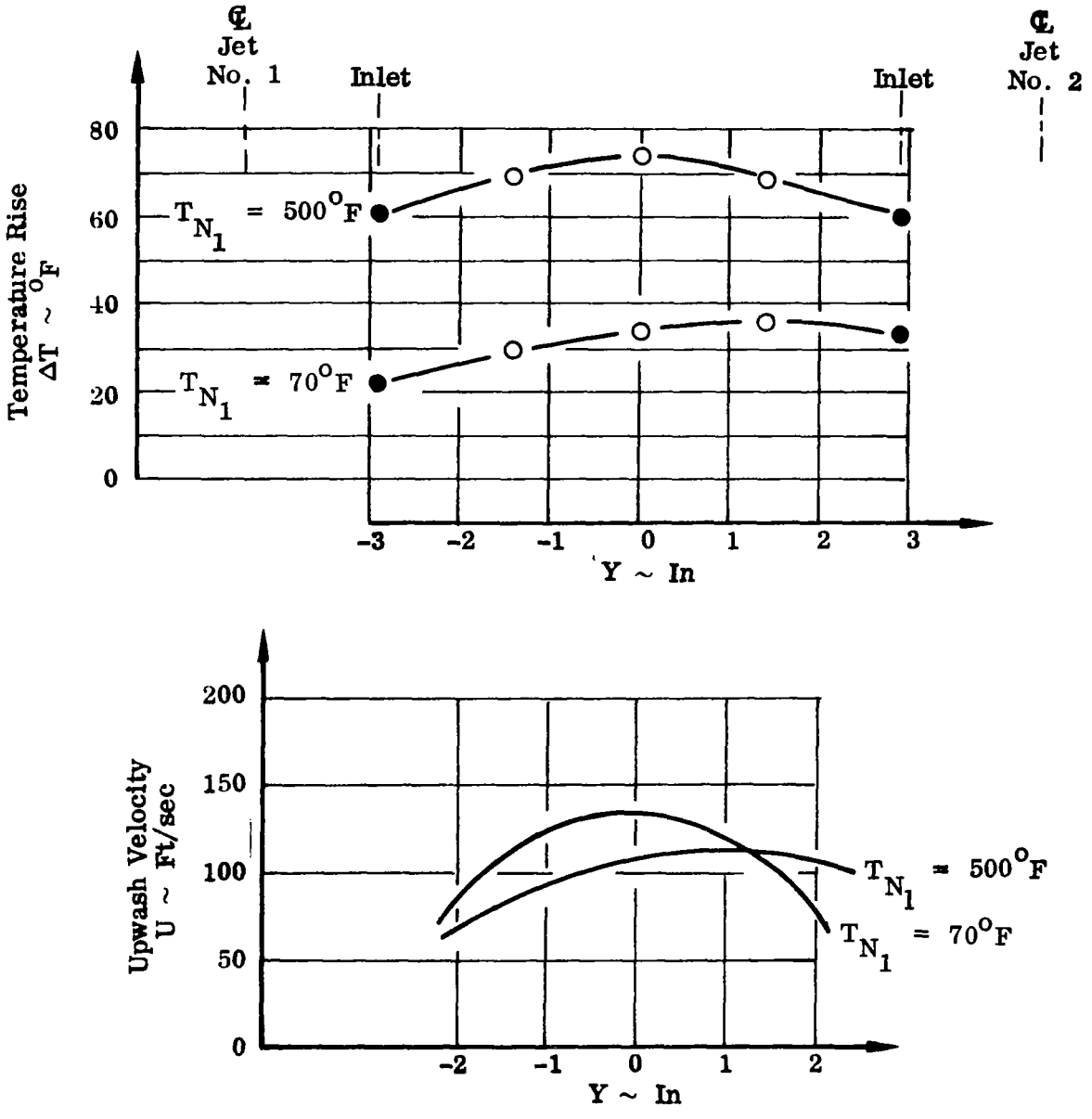

FIGURE 34. EFFECT OF NOZZLE TEMPERATURE BIAS ON UPWASH TEMPERATURE RISE AND VELOCITY

H/D = 3 T_N = 500°F

S/D = 7 $P_{N_1} = P_{N_2}$

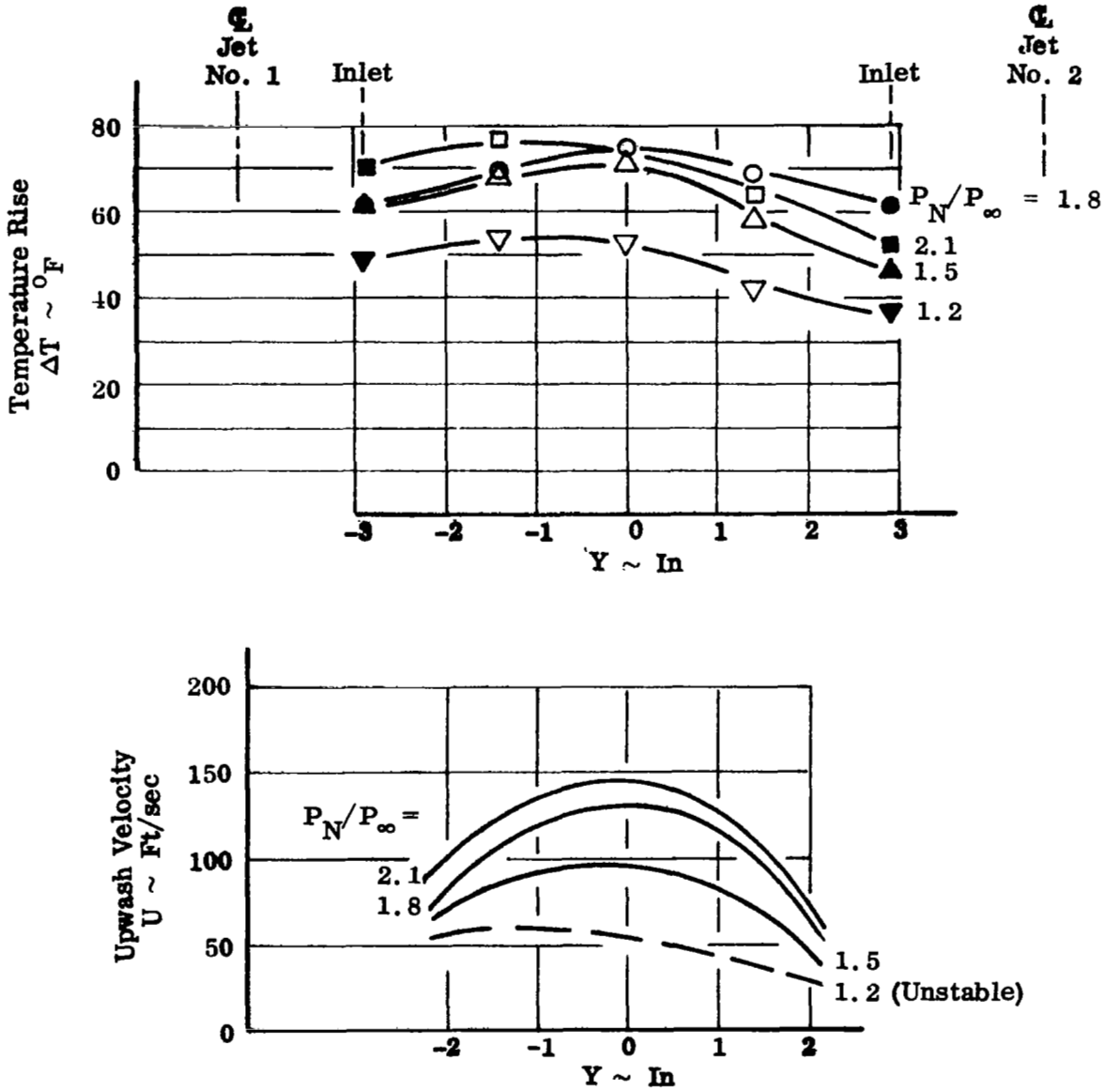

FIGURE 35. EFFECT OF NOZZLE PRESSURE LEVEL ON UPWASH TEMPERATURE RISE AND VELOCITY

H/D = 3 T_N = 500°F

S/D = 7

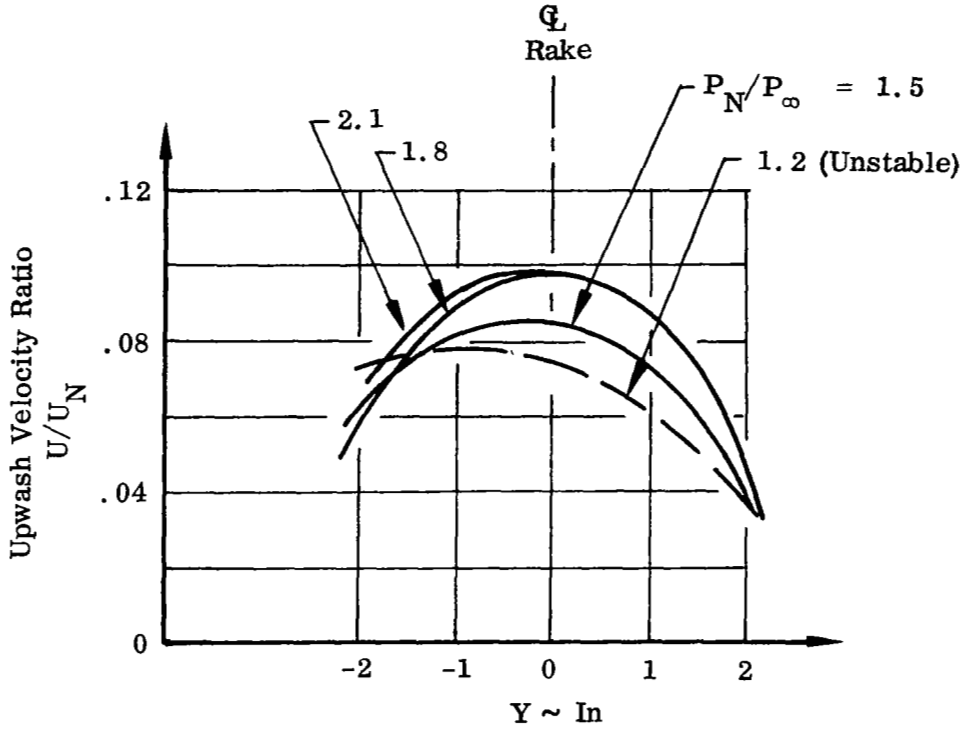

FIGURE 36. EFFECT OF NOZZLE PRESSURE LEVEL ON UPWASH VELOCITY RATIO

H/D = 3 T_N = 500°F

S/D = 7 P_{N_1}/P_∞ = 1.8

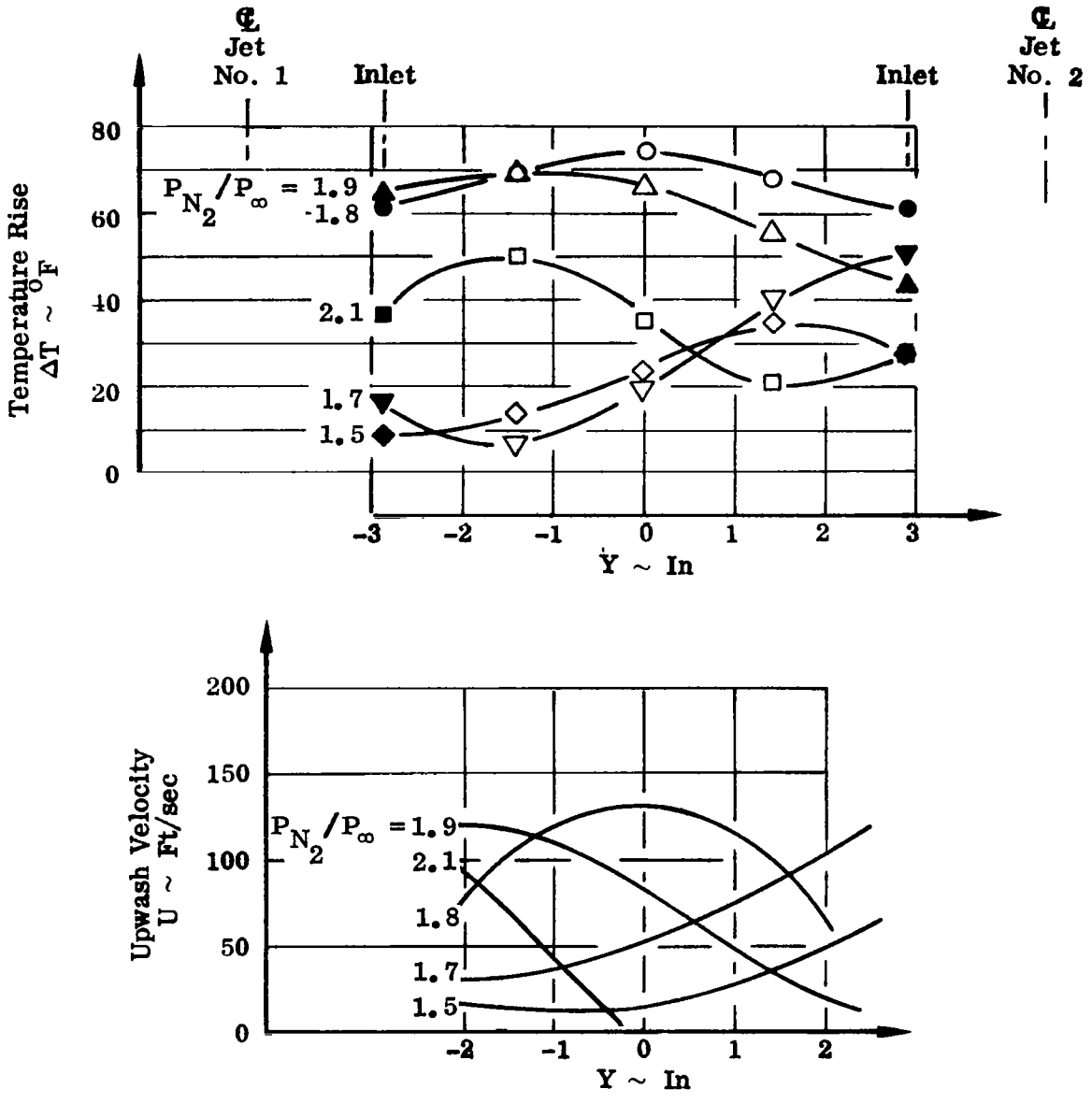

FIGURE 37. EFFECT OF NOZZLE PRESSURE BIAS ON UPWASH TEMPERATURE RISE AND VELOCITY

H/D = 3 T_N = 500°F

S/D = 7

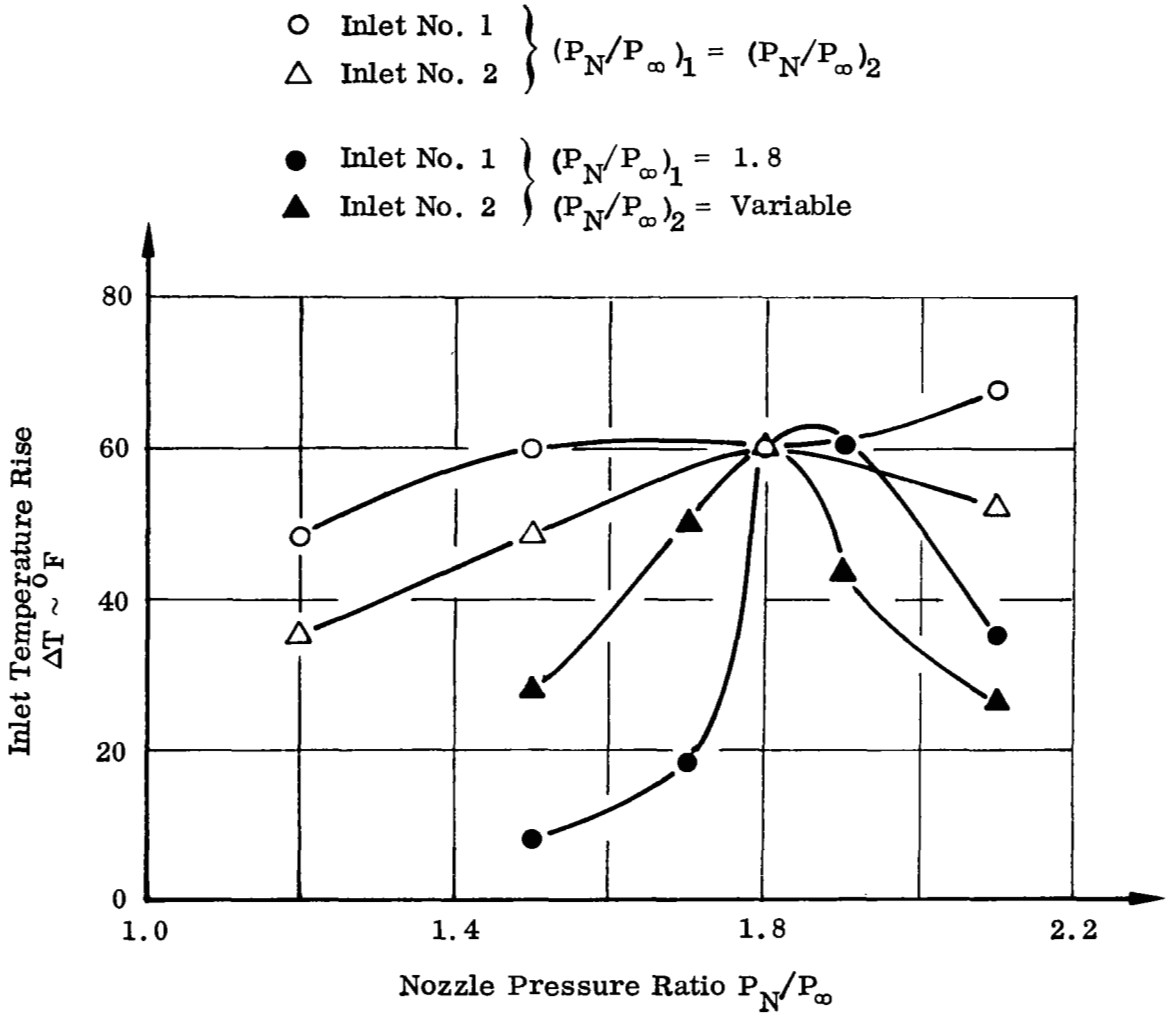

FIGURE 38. EFFECT OF NOZZLE PRESSURE LEVEL AND PRESSURE BIAS ON INLET TEMPERATURE RISE

H/D = 3 T_N = 500°F

S/D = 7 P_N/P_∞ = 1.8

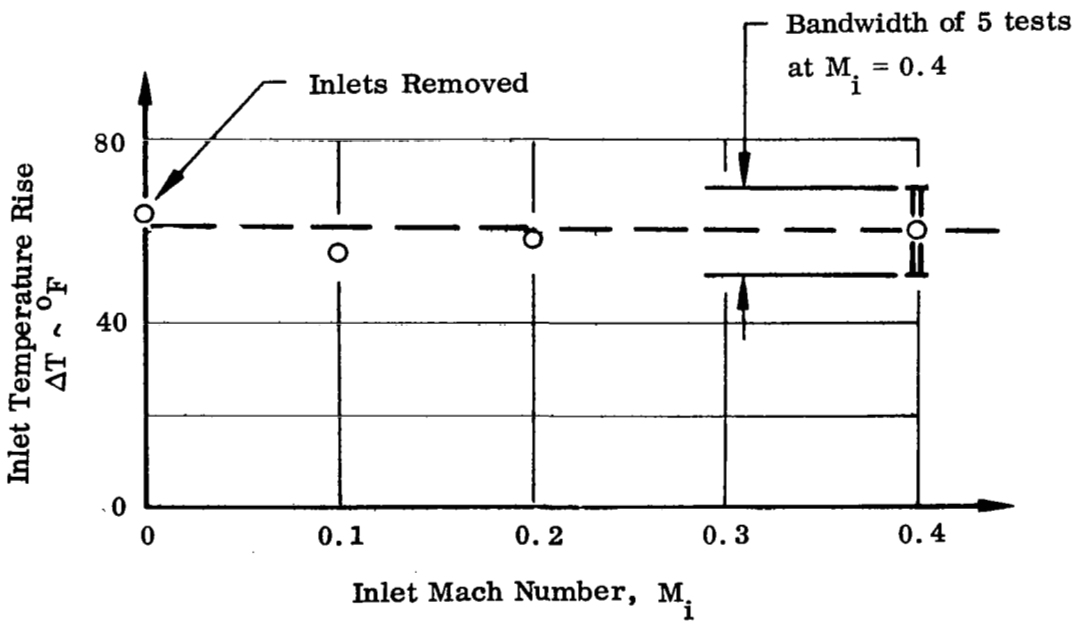

FIGURE 39. EFFECT OF INLET MACH NO. ON INLET TEMPERATURE RISE

H/D = 3	T_N = 500°F
S/D = 7	P_N/P_∞ = 1.8

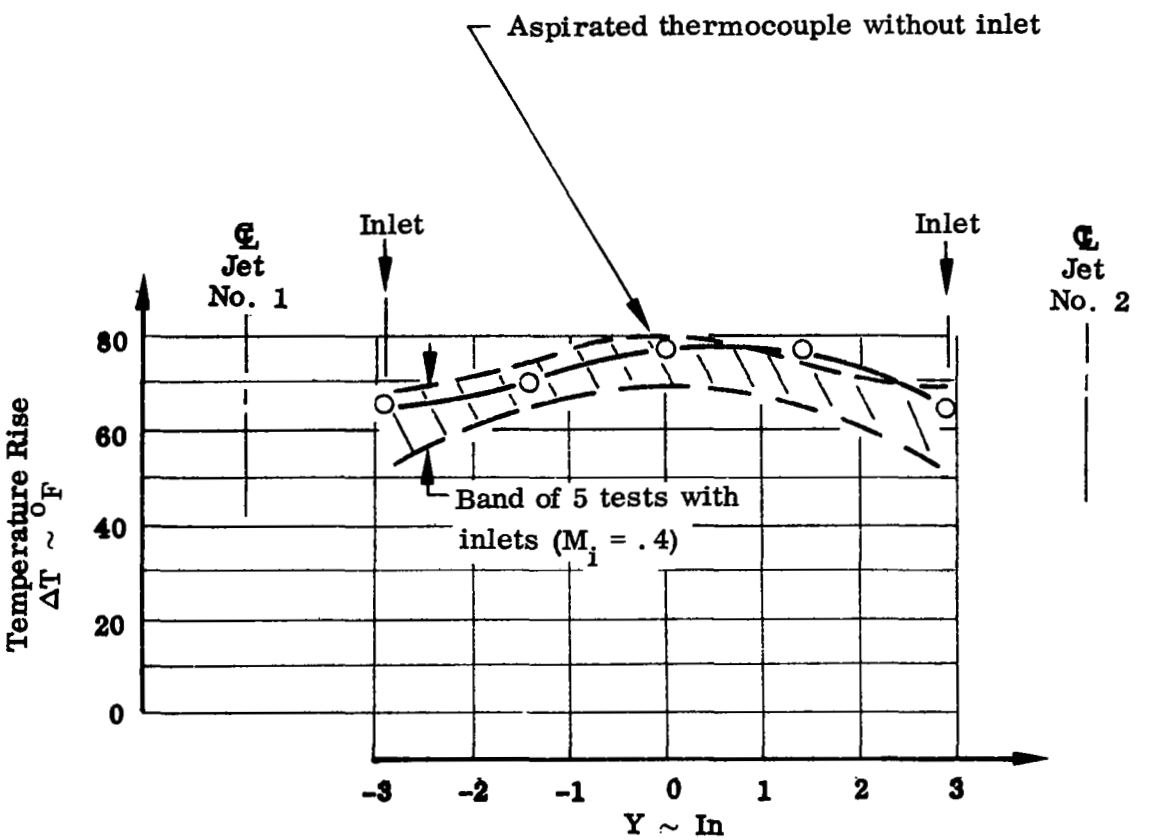

FIGURE 40. EFFECT OF INLETS ON UPWASH TEMPERATURE DISTRIBUTION

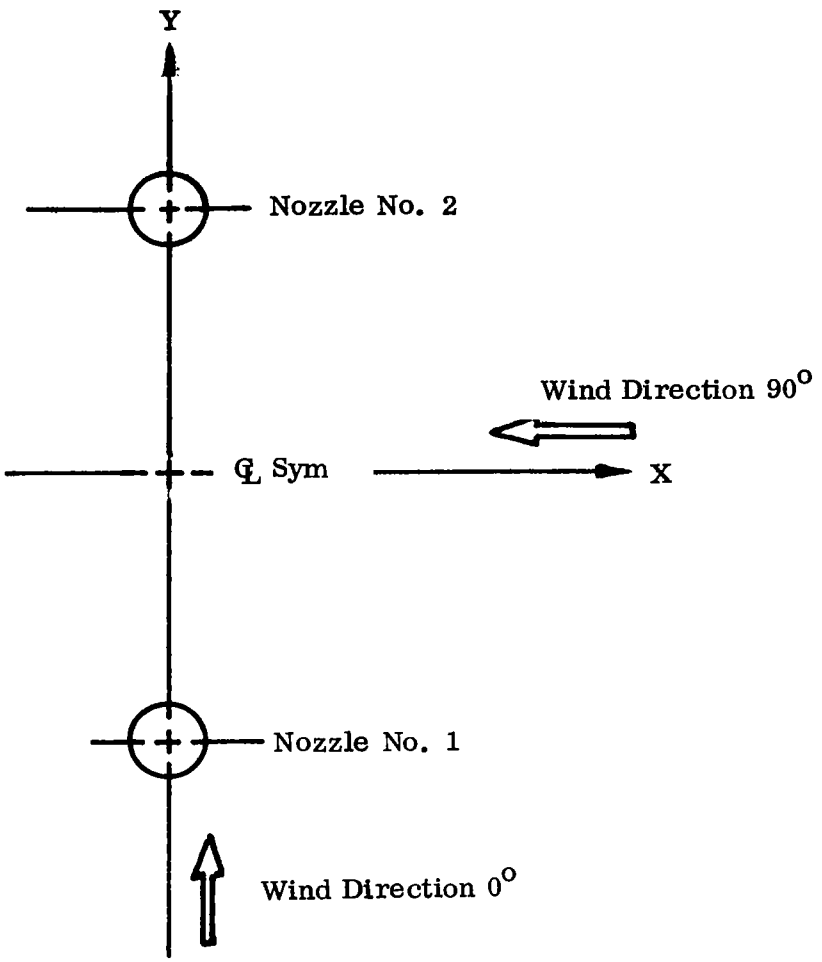

FIGURE 41. PLAN VIEW SHOWING WIND DIRECTIONS

H/D = 3 T_N = 500°F

S/D = 7 P_N/P_∞ = 1.8

Wind Direction = 0°

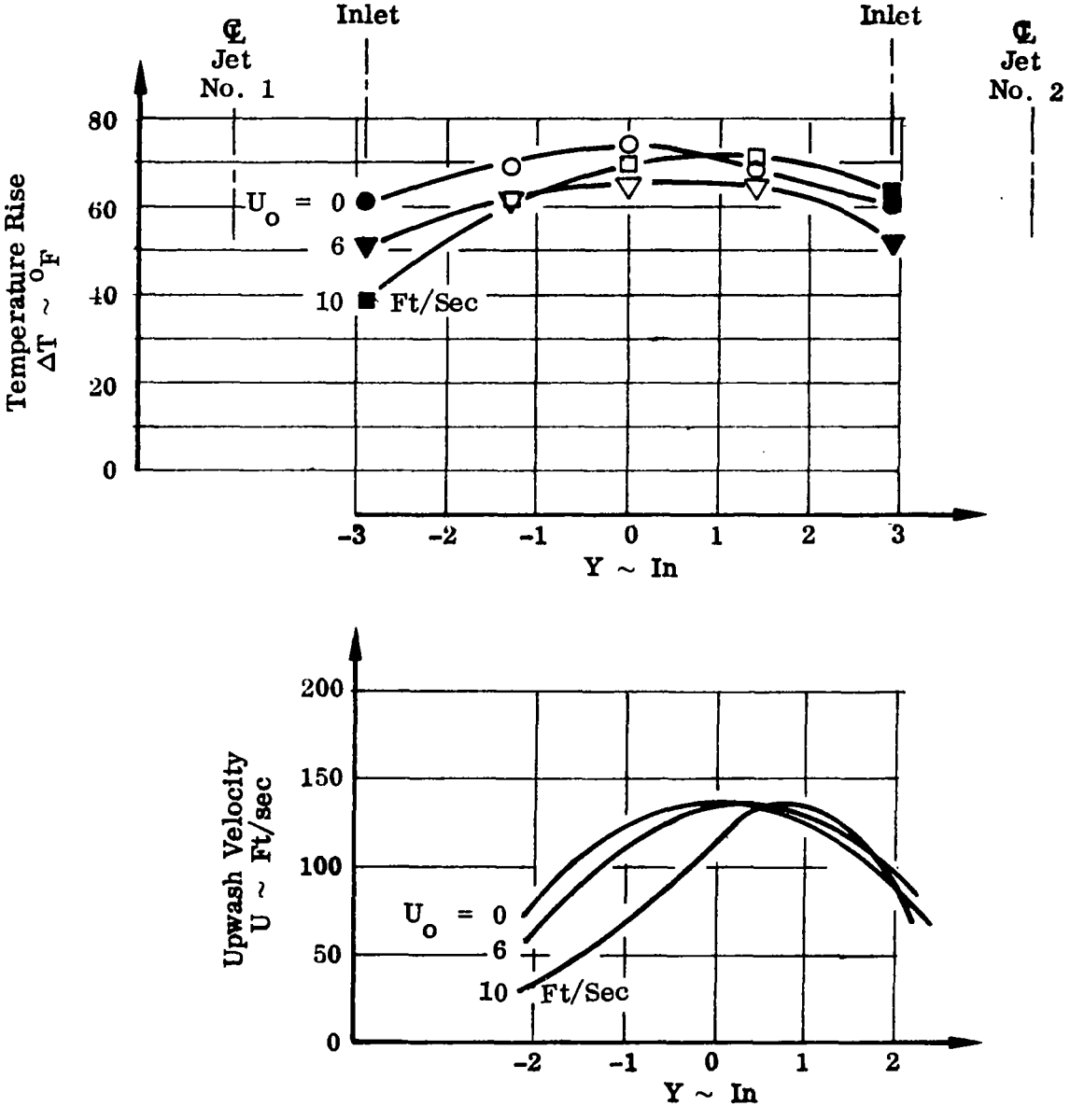

FIGURE 42. EFFECT OF WIND VELOCITY ON UPWASH TEMPERATURE RISE AND VELOCITY

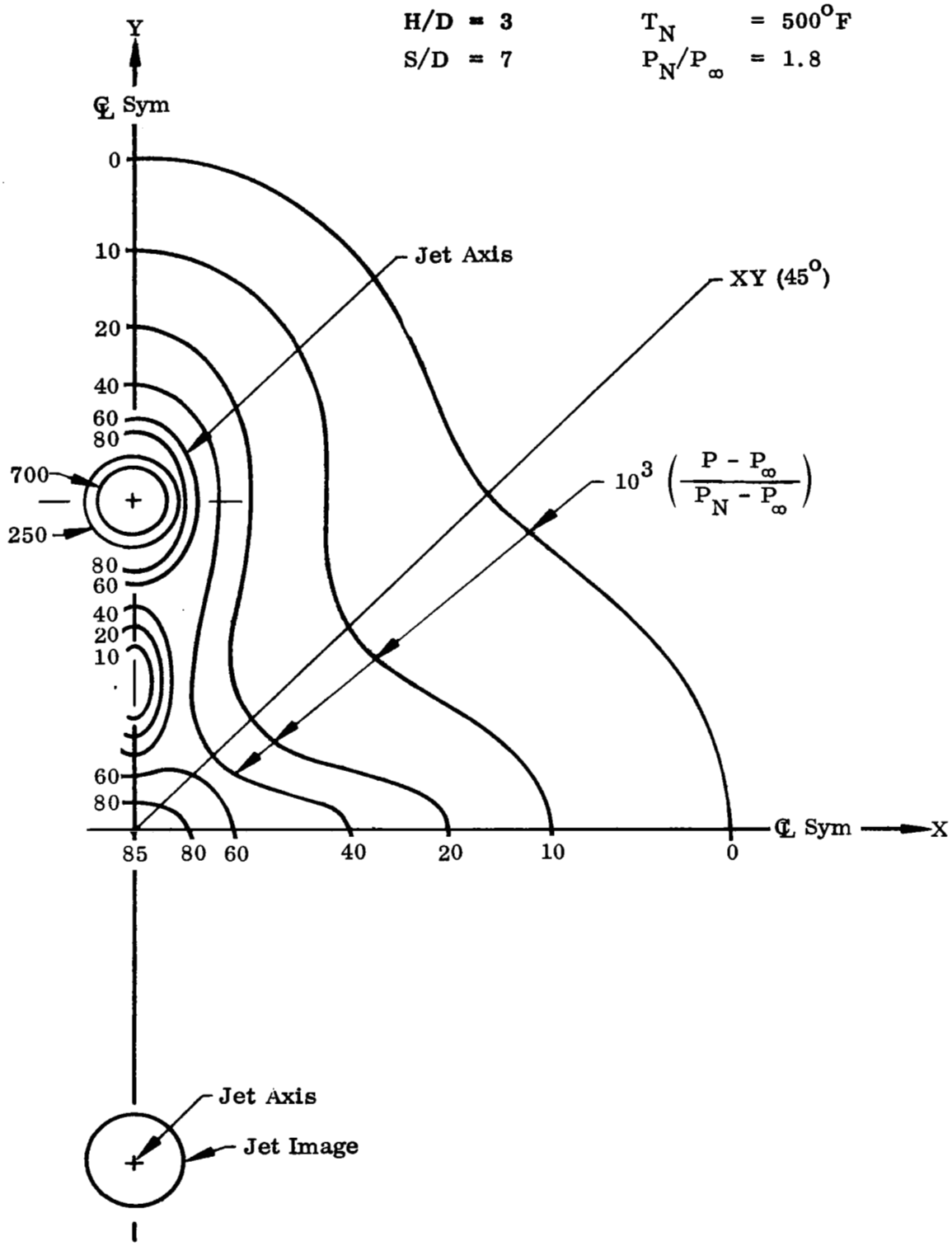

FIGURE 43. GROUND PLANE PRESSURE MAP

H/D = 1 ○
3 △
5 ▽
8 □

S/D = 7

T_N = 500°F

P_N/P_∞ = 1.8

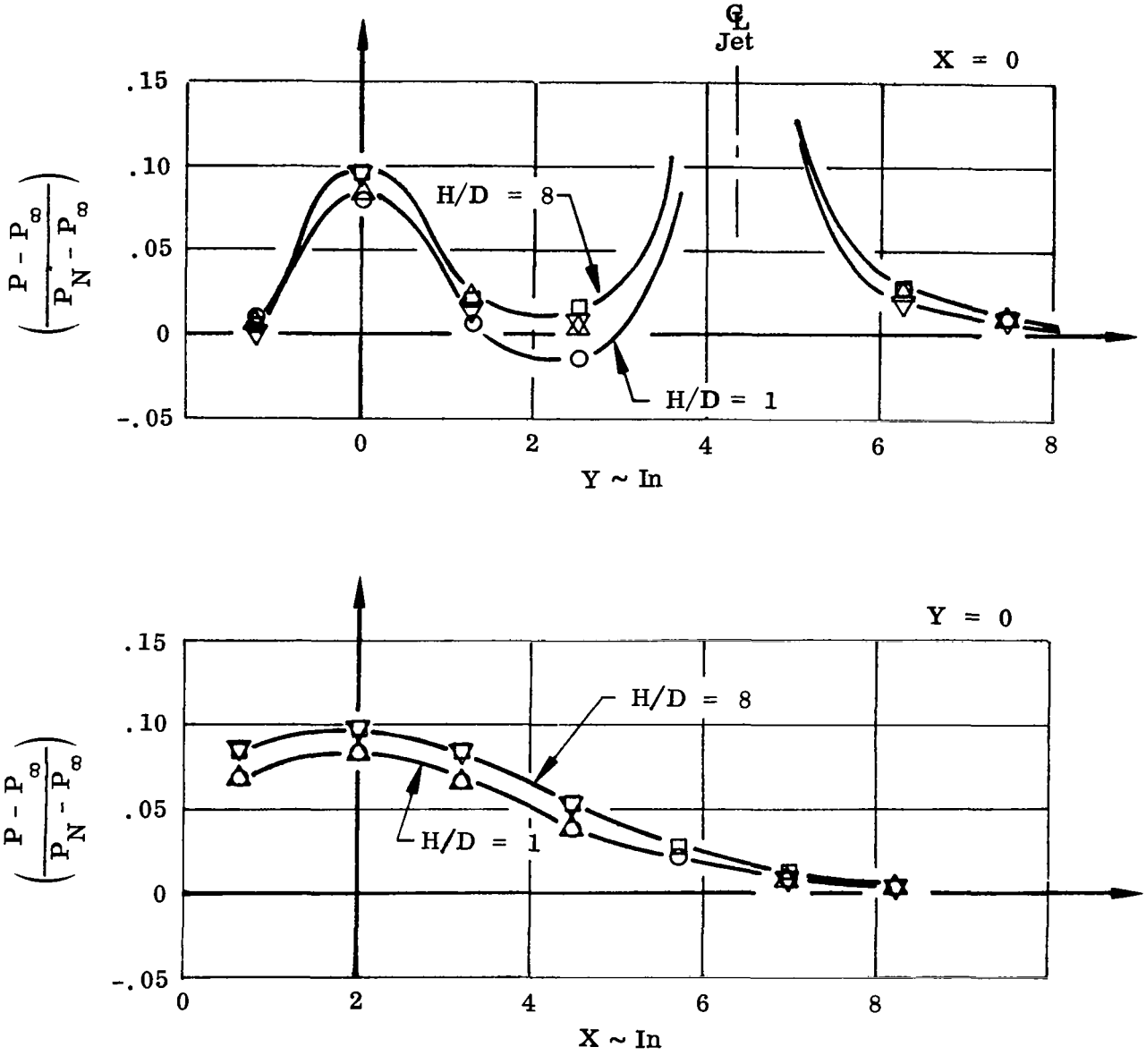

FIGURE 44. EFFECT OF H/D ON GROUND PRESSURE DISTRIBUTION

H/D = 3

T_N = 500°F

P_N/P_∞ = 1.8

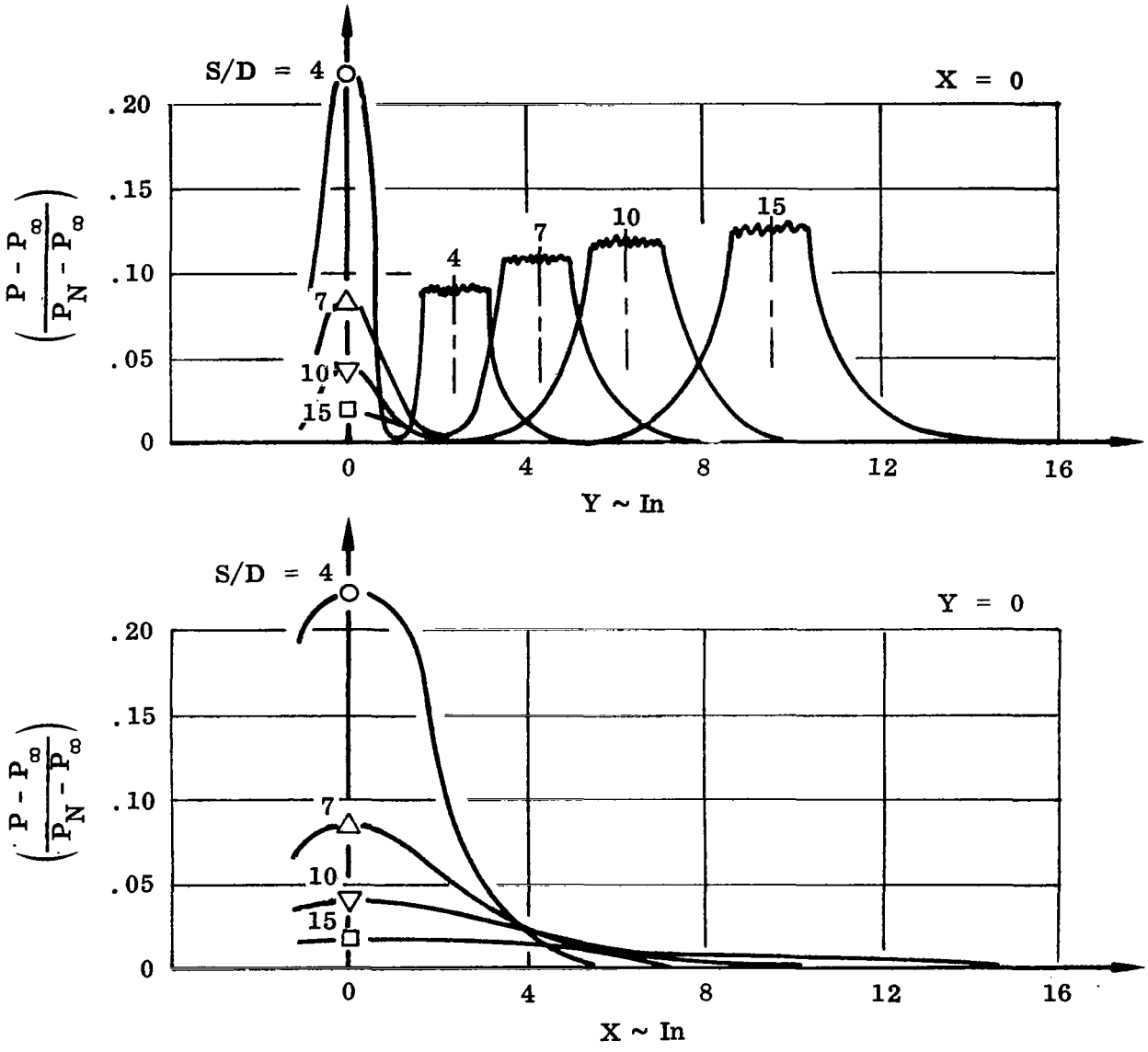

FIGURE 45. EFFECT OF S/D ON GROUND PRESSURE DISTRIBUTION

X = 0 T_N = 500°F

Y = 0 P_N/P_∞ = 1.8

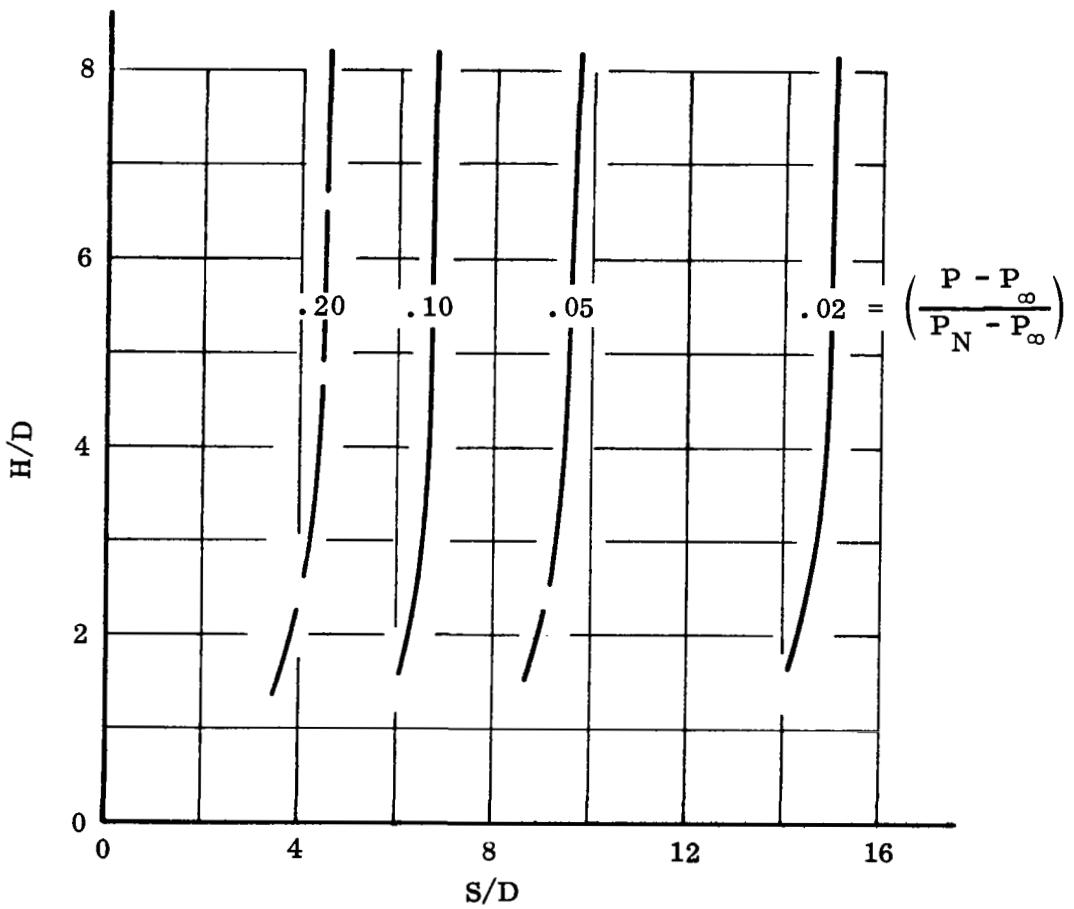

FIGURE 46. GROUND PLANE CENTER PRESSURE VARIATION WITH H/D AND S/D

H/D = 3 T_N = 500°F

S/D = 7 P_N/P_∞ = 1.8

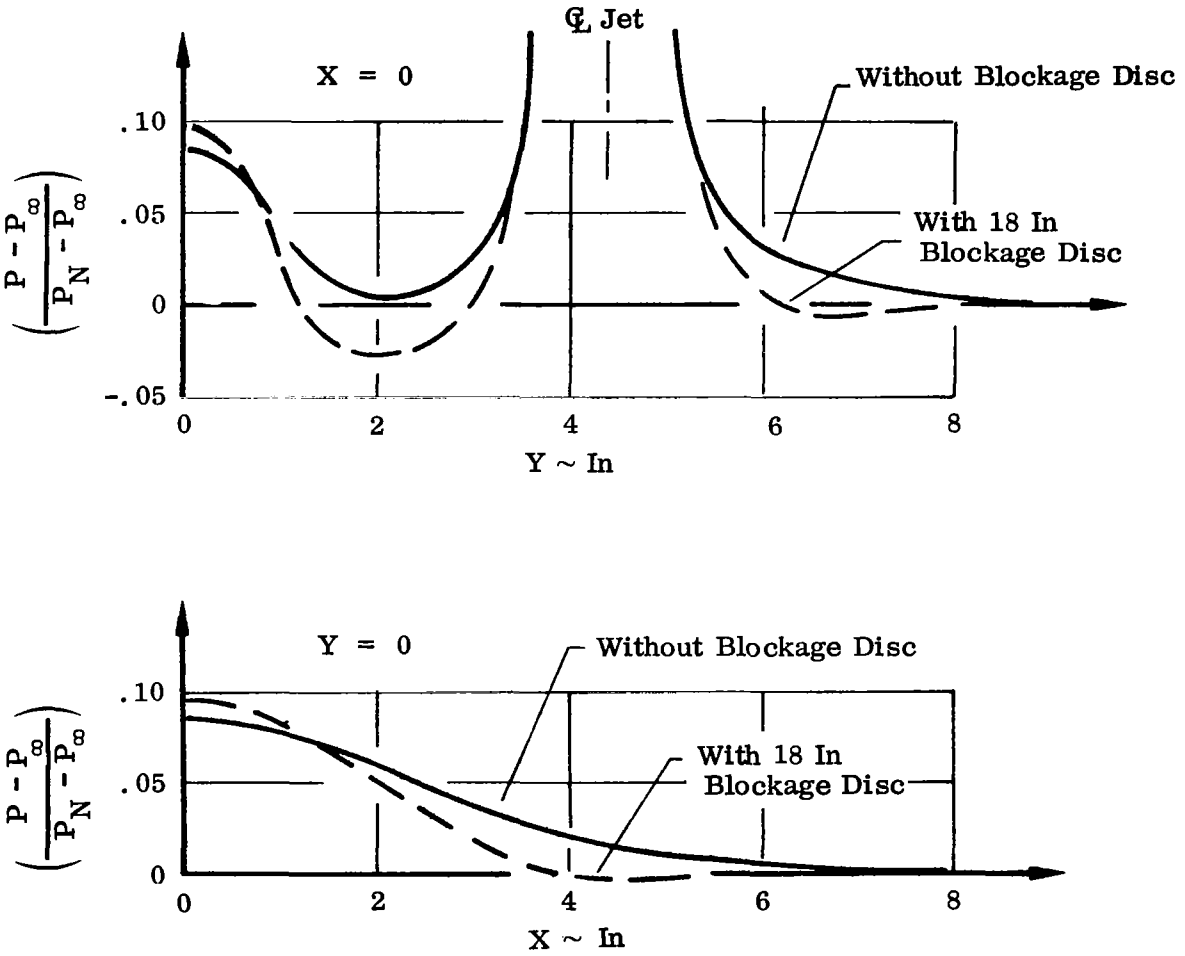

FIGURE 47. EFFECT OF BLOCKAGE DISC ON GROUND PRESSURE DISTRIBUTION

H/D = 3 $T_N = 500^oF$

S/D = 7 $P_N/P_\infty = 1.8$

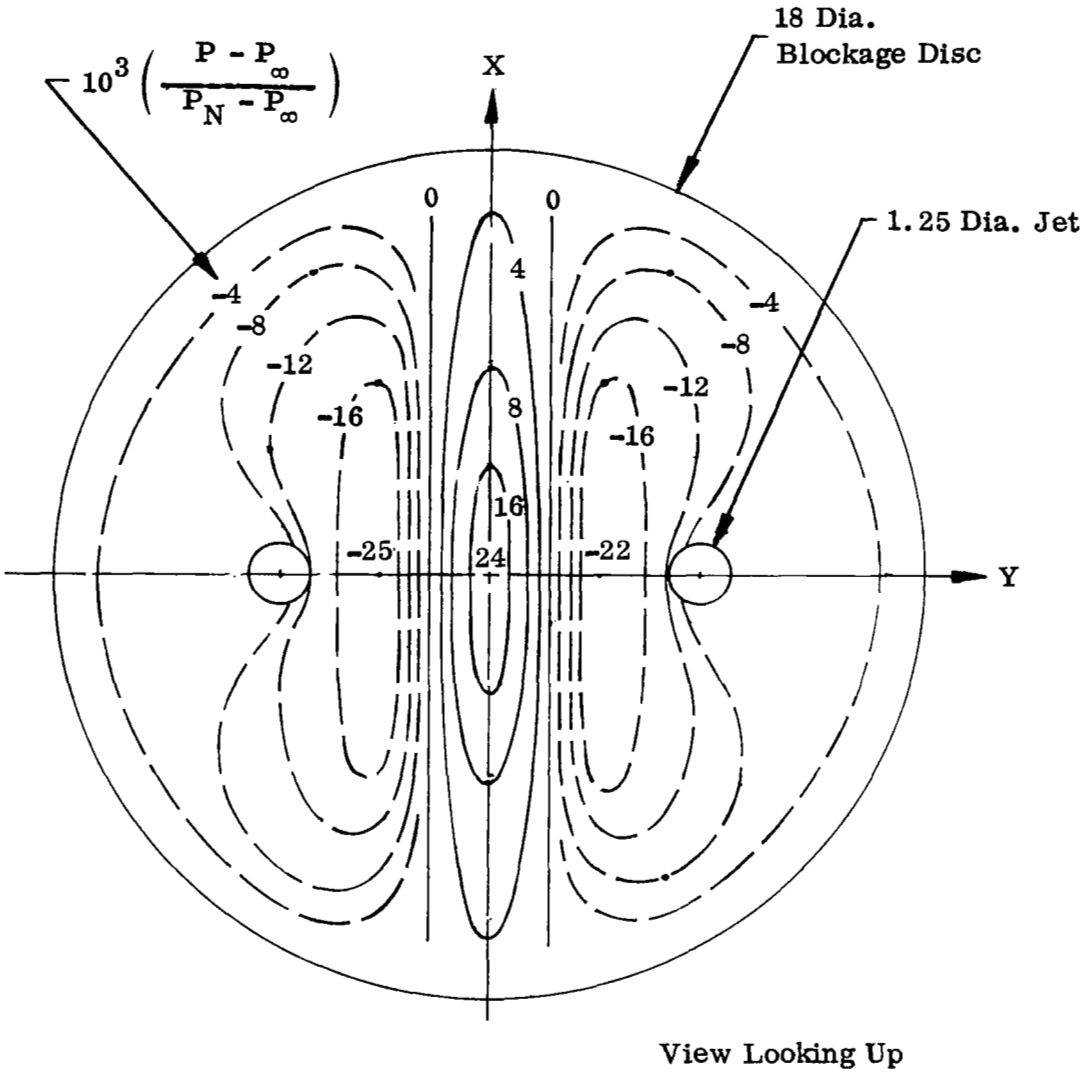

FIGURE 48. PRESSURE MAP ON LOWER SURFACE OF 18 INCH BLOCKAGE DISC

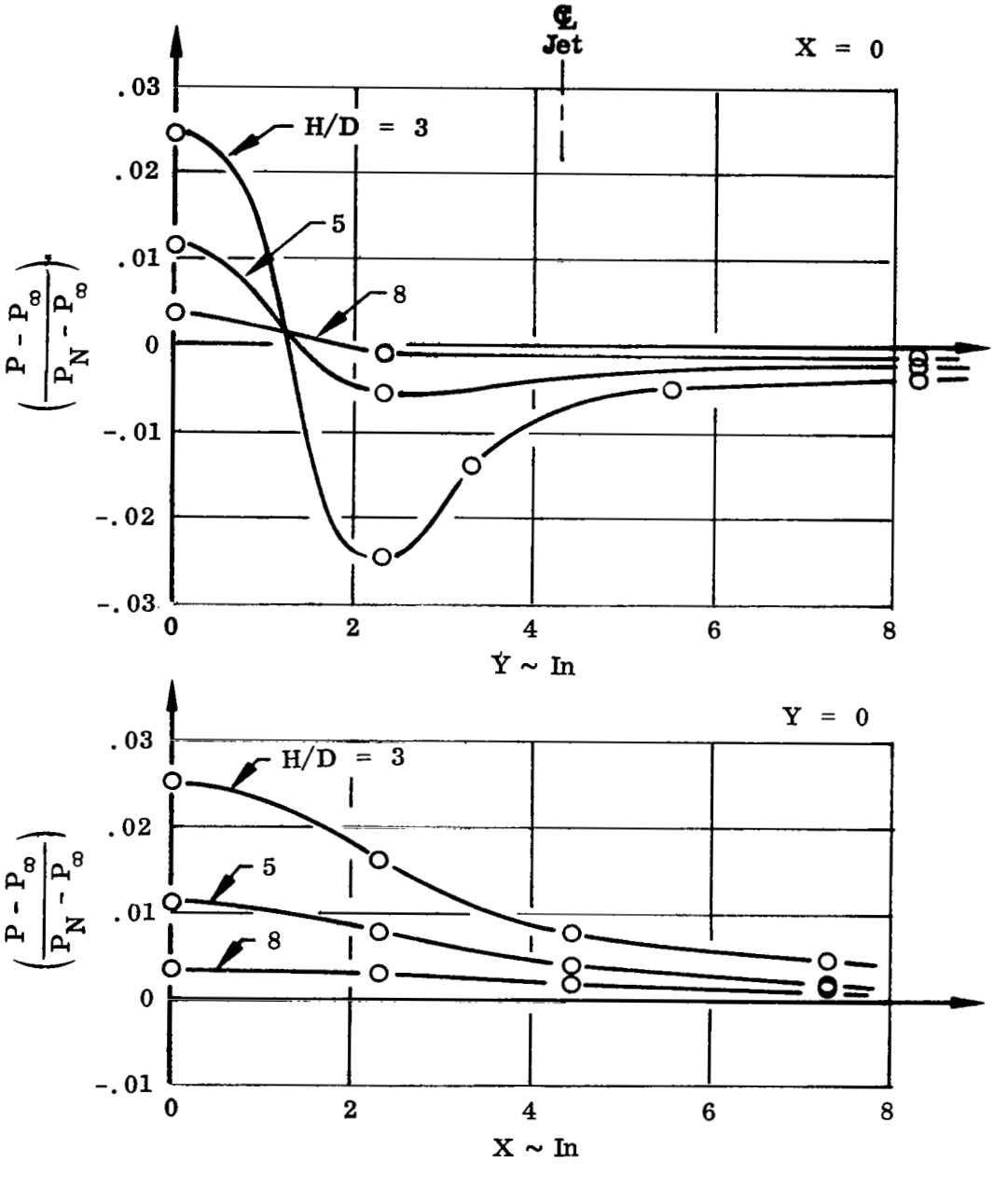

FIGURE 49. EFFECT OF H/D ON PRESSURE DISTRIBUTION ON LOWER SURFACE OF 1⅛ INCH BLOCKAGE DISC

H/D = 3 T_N = 500°F

P_N/P_∞ = 1.8

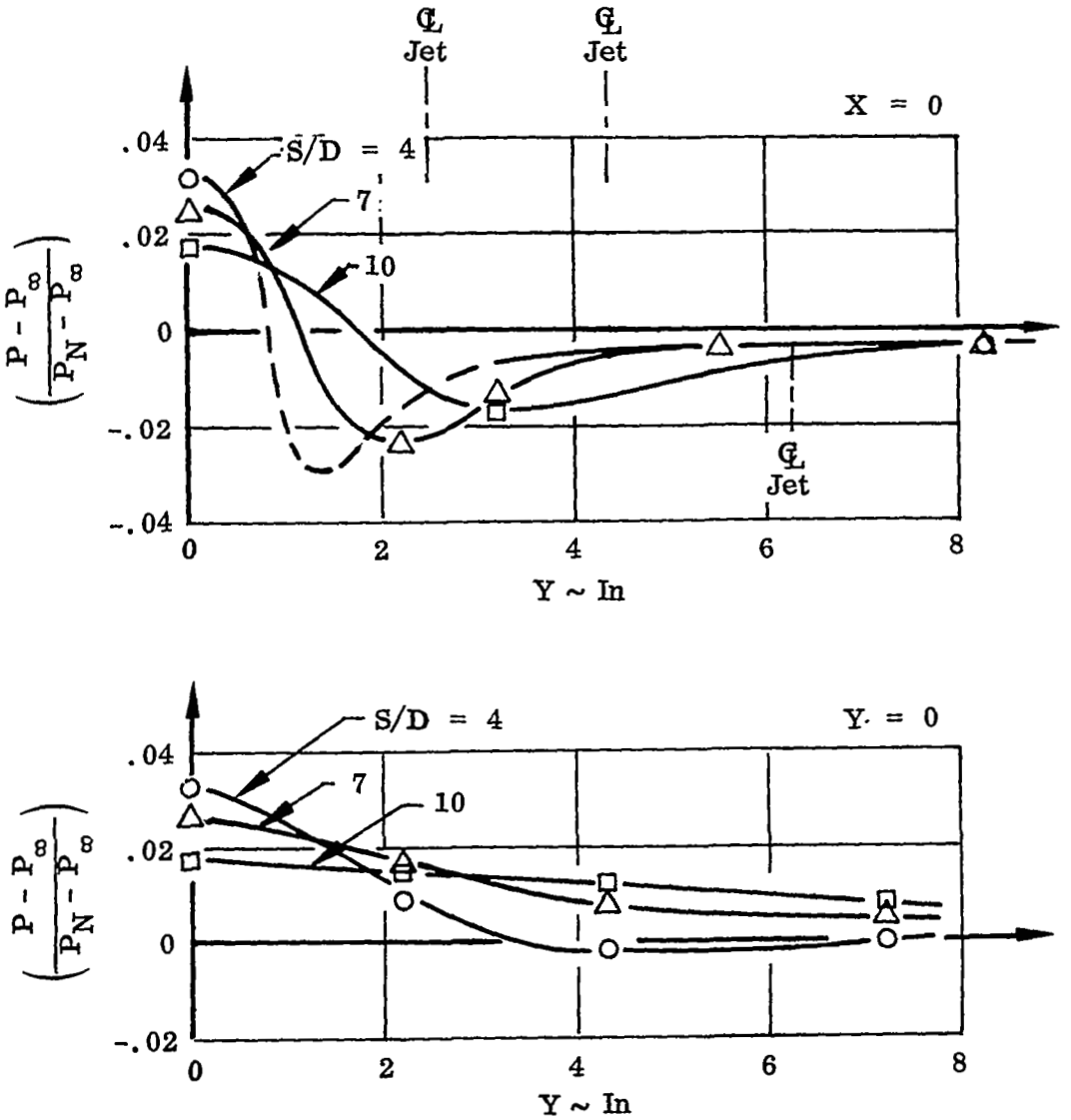

FIGURE 50. EFFECT OF S/D ON PRESSURE DISTRIBUTION ON LOWER SURFACE OF 18 INCH BLOCKAGE DISC

X = 0
Y = 0

T_N = 500°F
P_N/P_∞ = 1.8

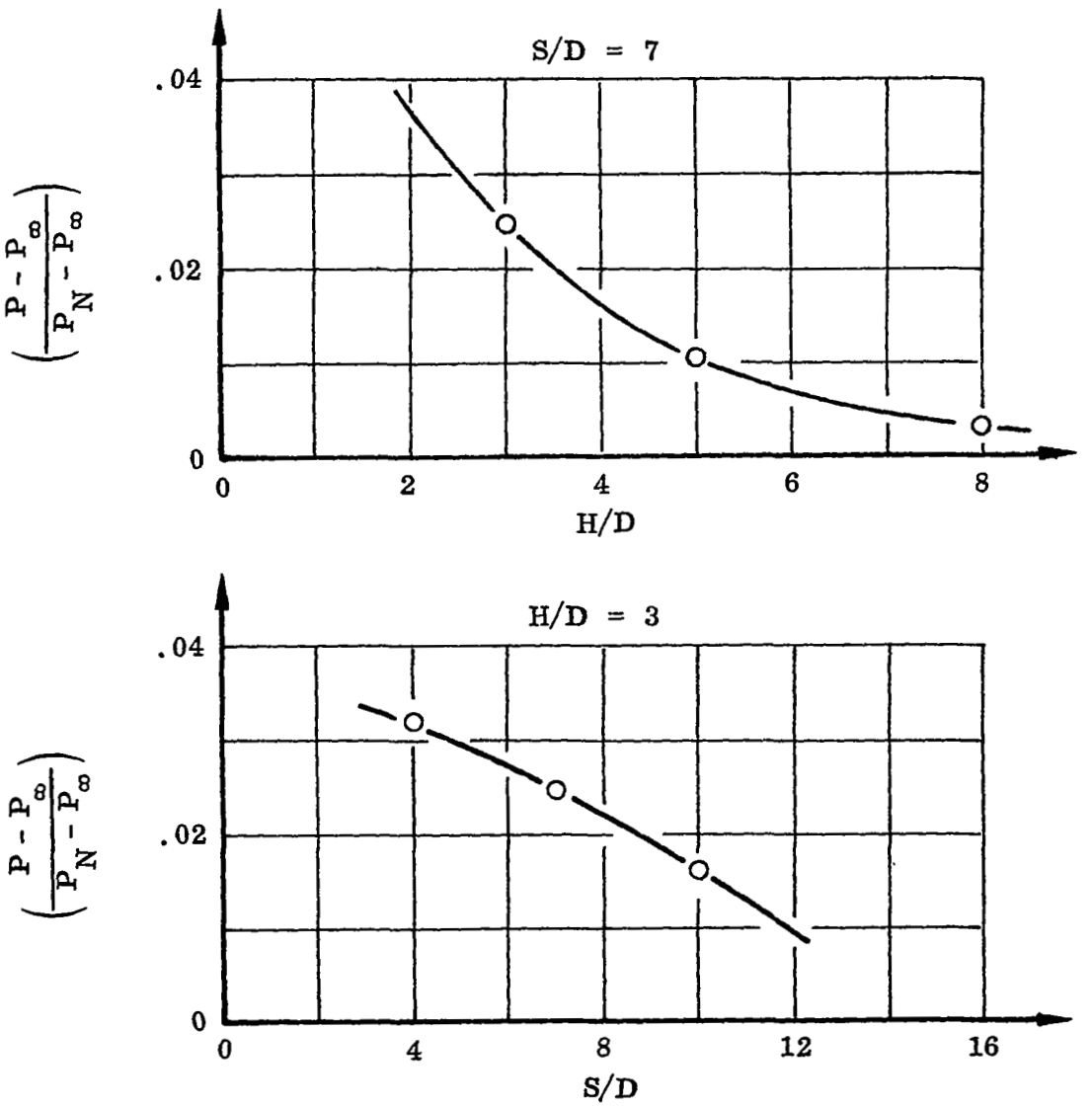

FIGURE 51. CENTER PRESSURE VARIATION WITH H/D AND S/D - 18 INCH BLOCKAGE DISC LOWER SURFACE

Area Ratio A_p/A_e = 103

O Current Investigation, S/D = 7

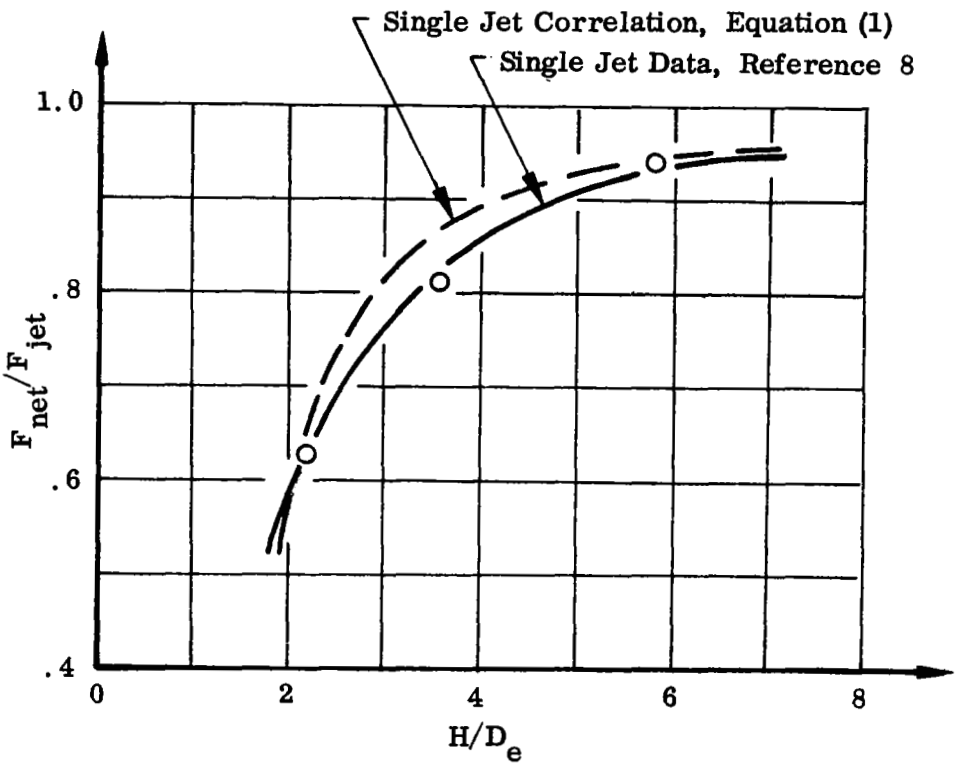

FIGURE 52. THRUST RATIO VS HEIGHT RATIO - 18 INCH BLOCKAGE DISC

H/D_e = 2.12

Area Ratio A_p/A_e = 103

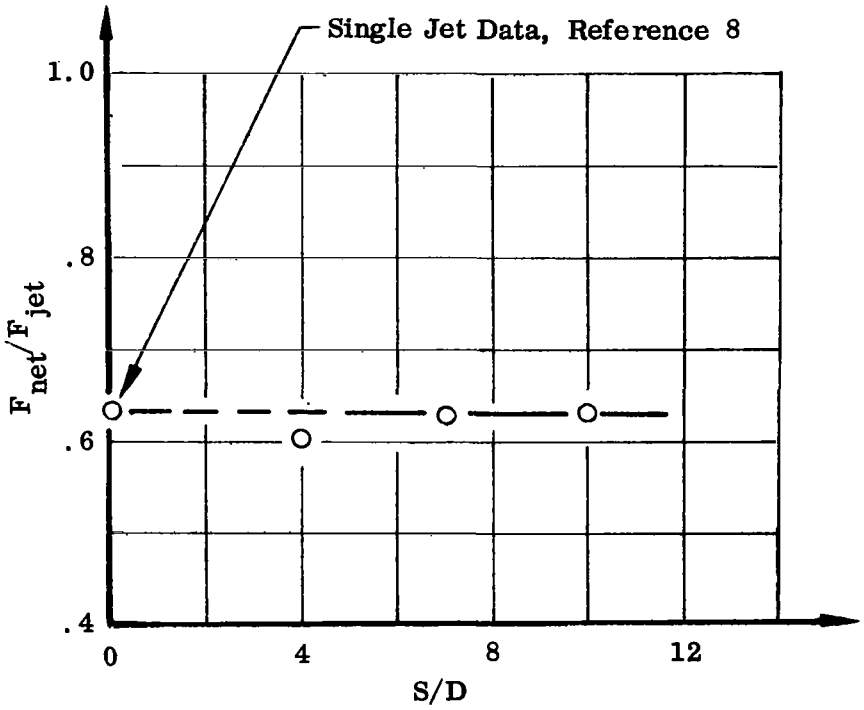

FIGURE 53. THRUST RATIO VS SPACING RATIO - 18 INCH BLOCKAGE DISC

H/D = 5

T_N = 600°F

P_N/P_∞ = 2.0

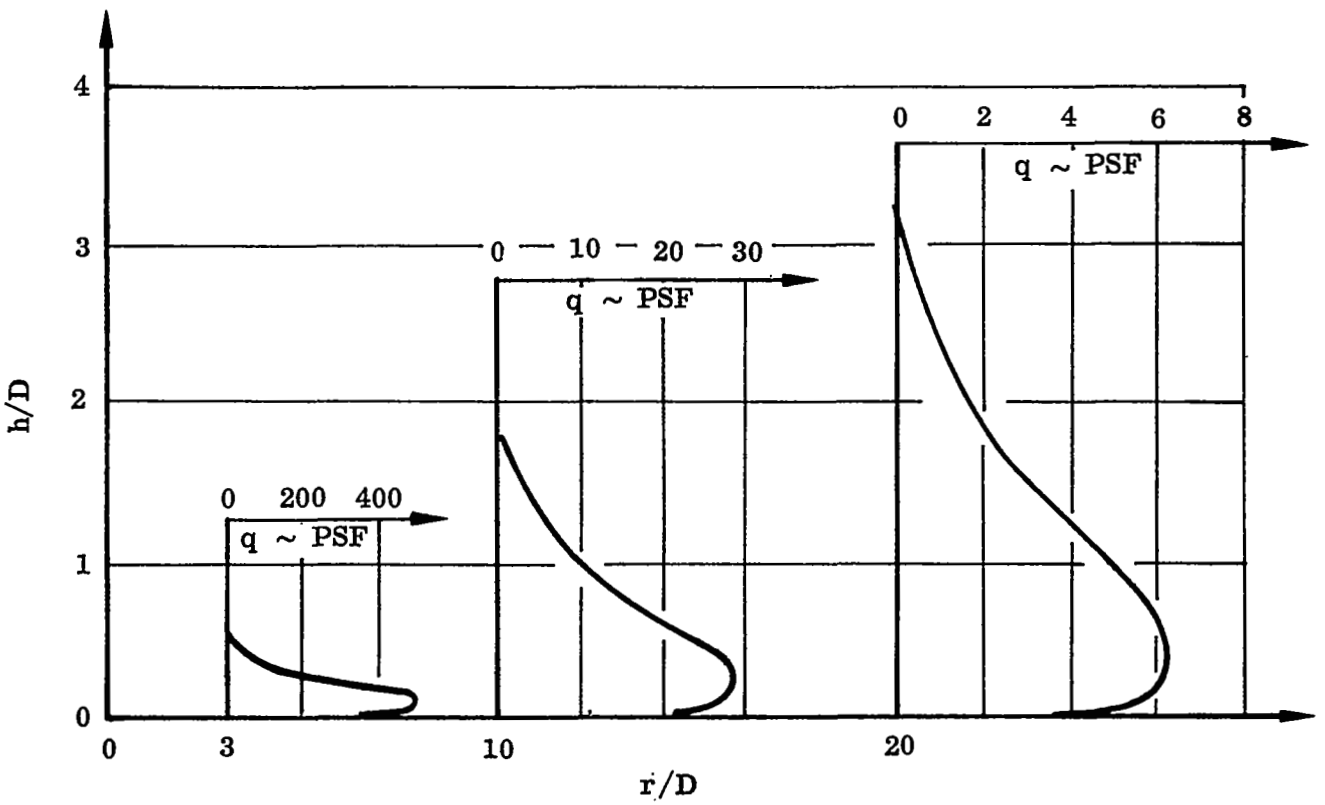

FIGURE 54. GROUND-JET DYNAMIC PRESSURE PROFILES - SINGLE JET

H/D = 5 T_N = 600°F

S/D = 7 P_N/P_∞ = 2.0

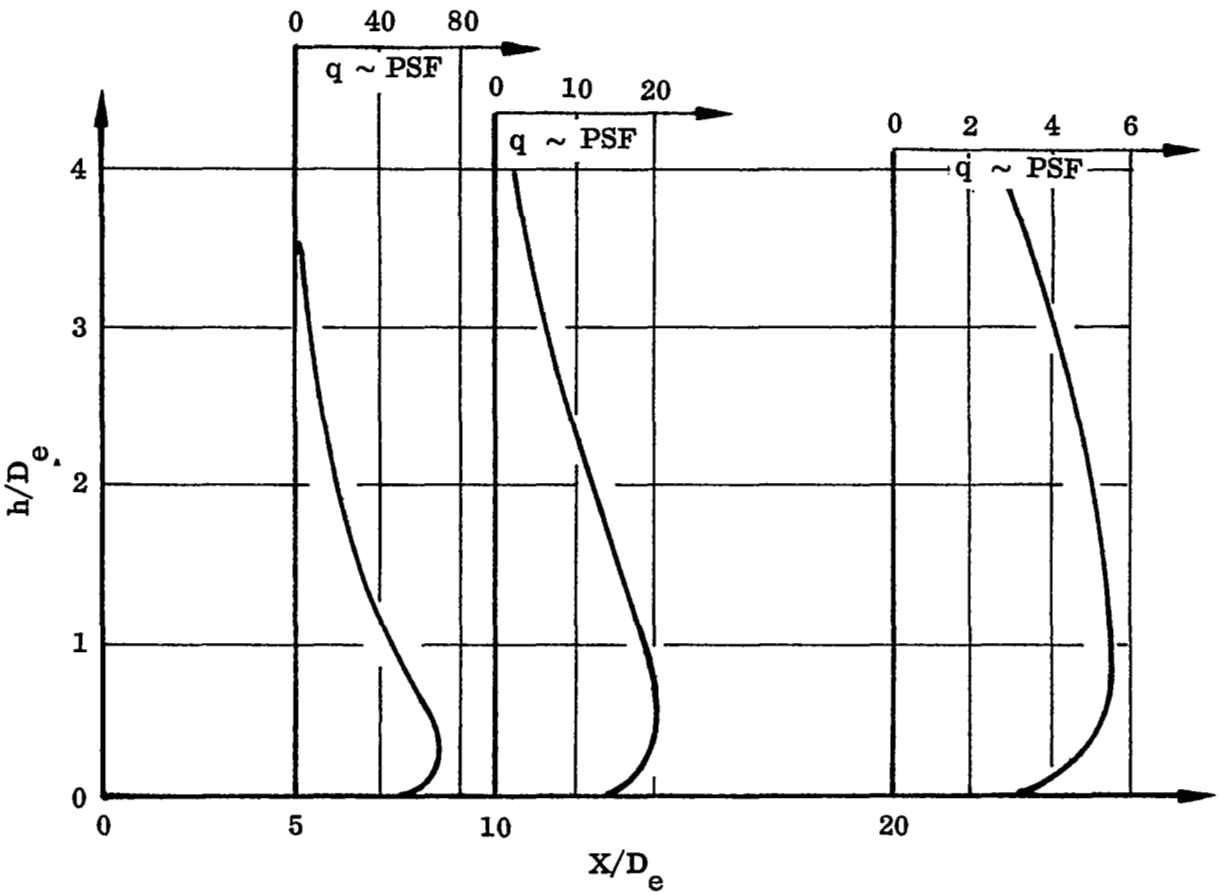

FIGURE 55. GROUND-JET DYNAMIC PRESSURE PROFILES - DUALJETS (INTERACTION PLANE)

H/D = 5

T_N = 600°F

P_N/P_∞ = 2.0

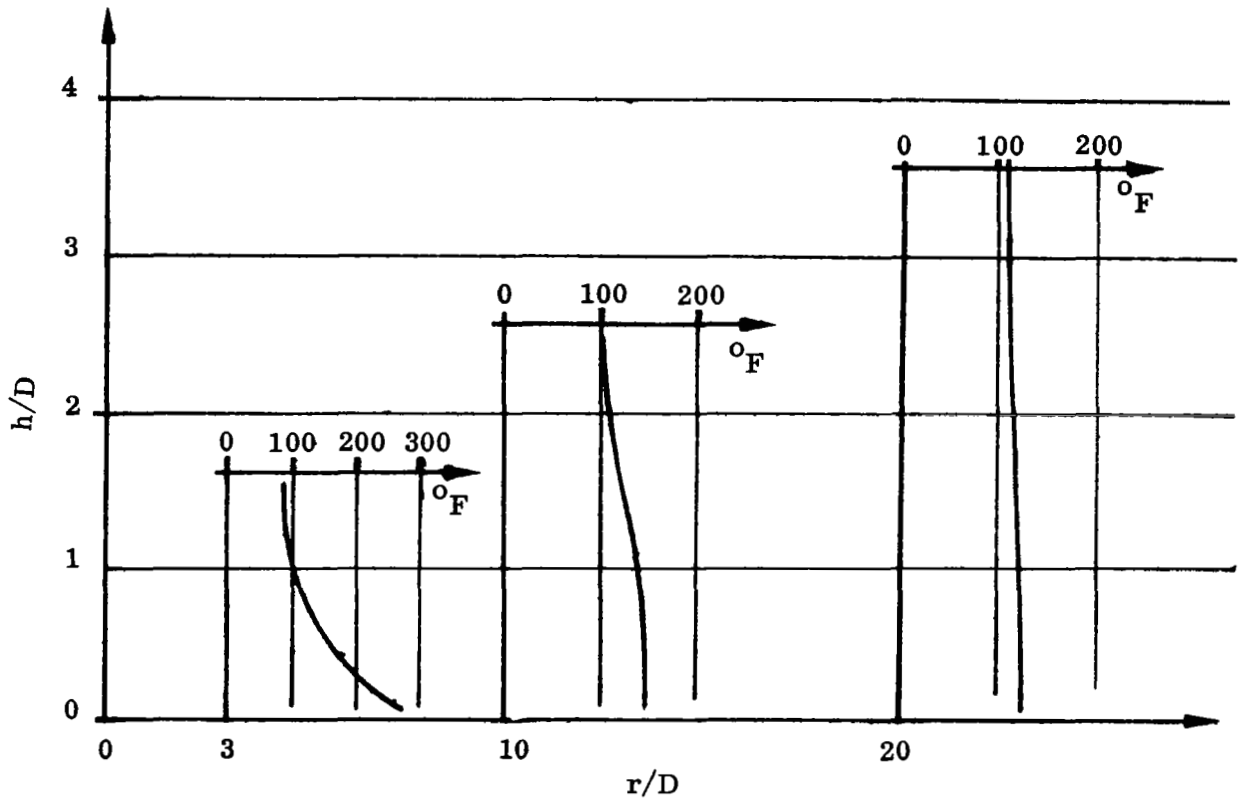

FIGURE 56. GROUND-JET TEMPERATURE PROFILES - SINGLE-JET

H/D = 5	T_N = 600°F
S/D = 7	P_N/P_∞ = 2.0

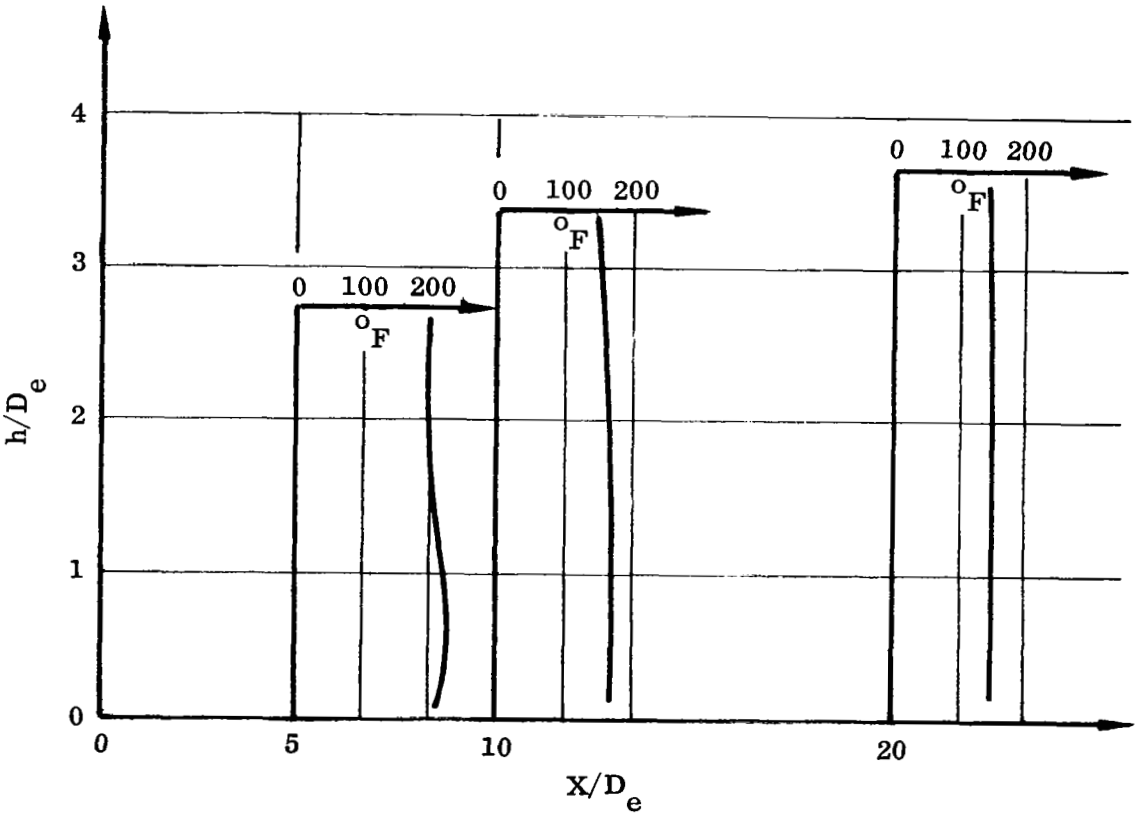

FIGURE 57. GROUND-JET TEMPERATURE PROFILES - DUAL JETS (INTERACTION PLANE)

H/D = 5

T_N = 600°F

P_N/P_∞ = 2.0

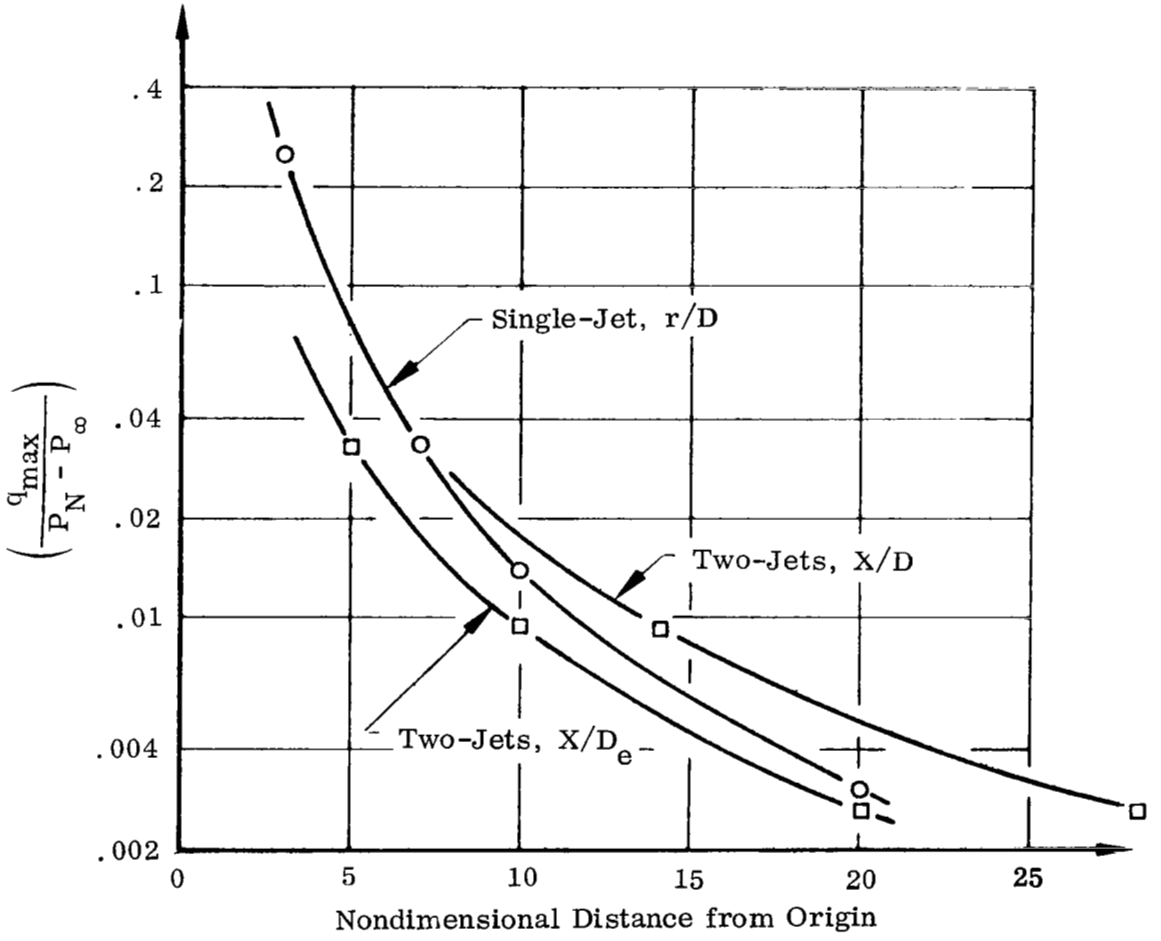

FIGURE 58. GROUND-JET DYNAMIC PRESSURE DECAY

H/D = 5 $T_N = 600^{\circ}F$

$P_N/P_\infty = 2.0$

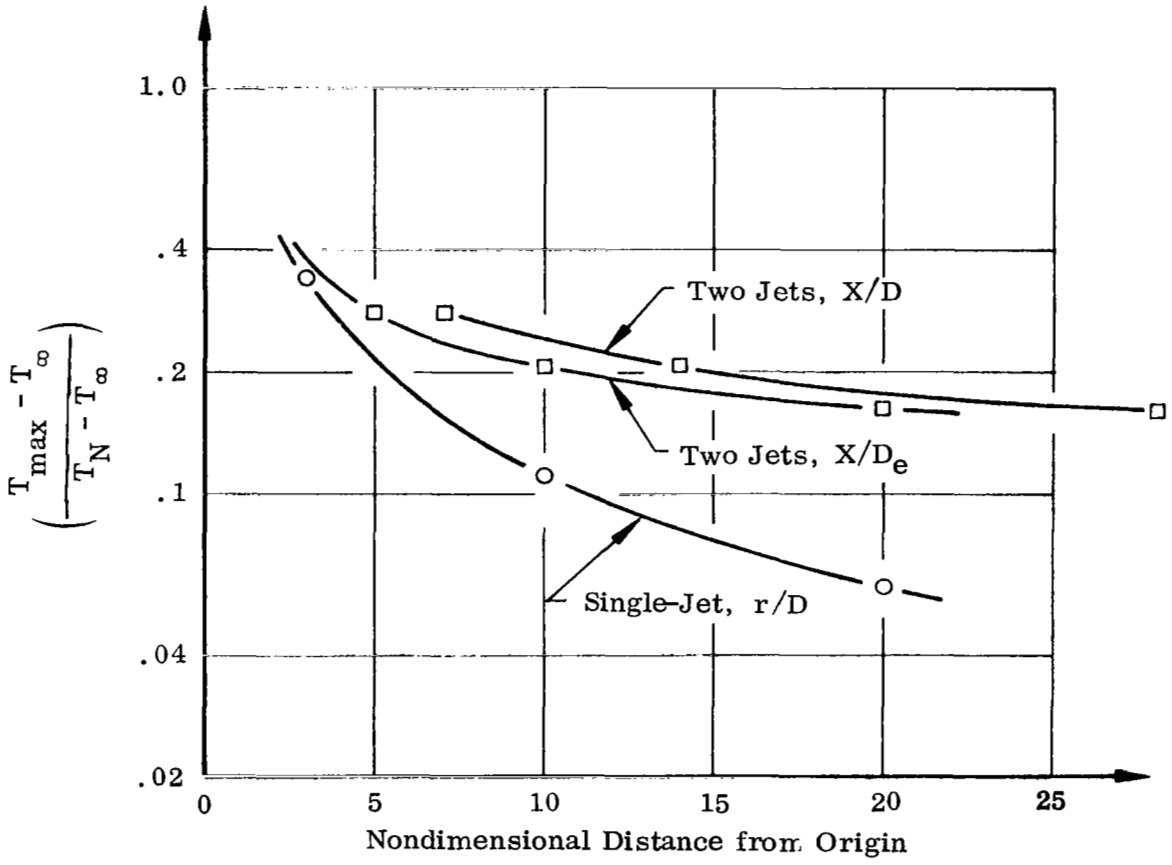

FIGURE 59. GROUND-JET TEMPERATURE DECAY

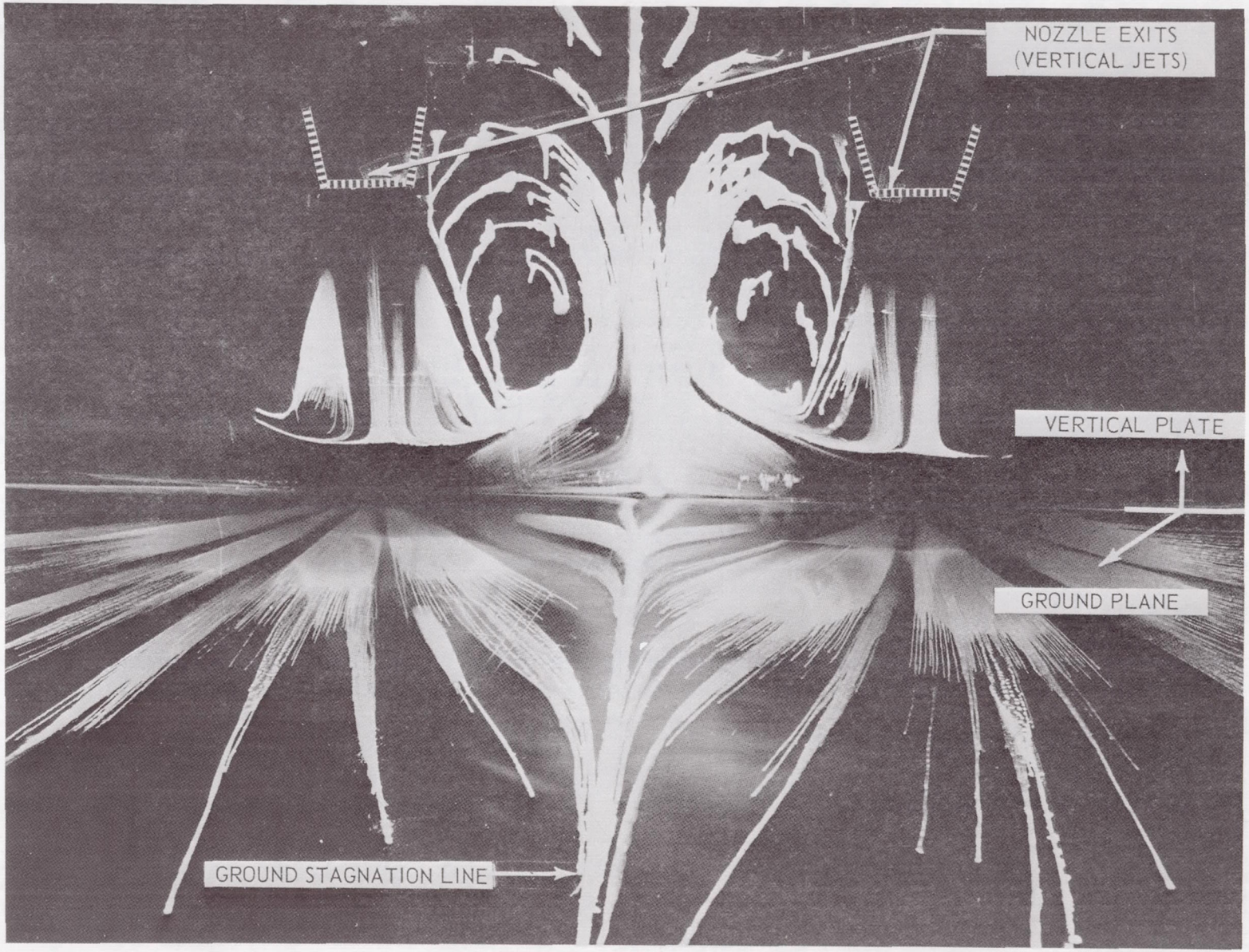

FIGURE 60 NOMINAL FLOW FIELD WITH VERTICAL NOZZLES AND EQUAL NOZZLE PRESSURES

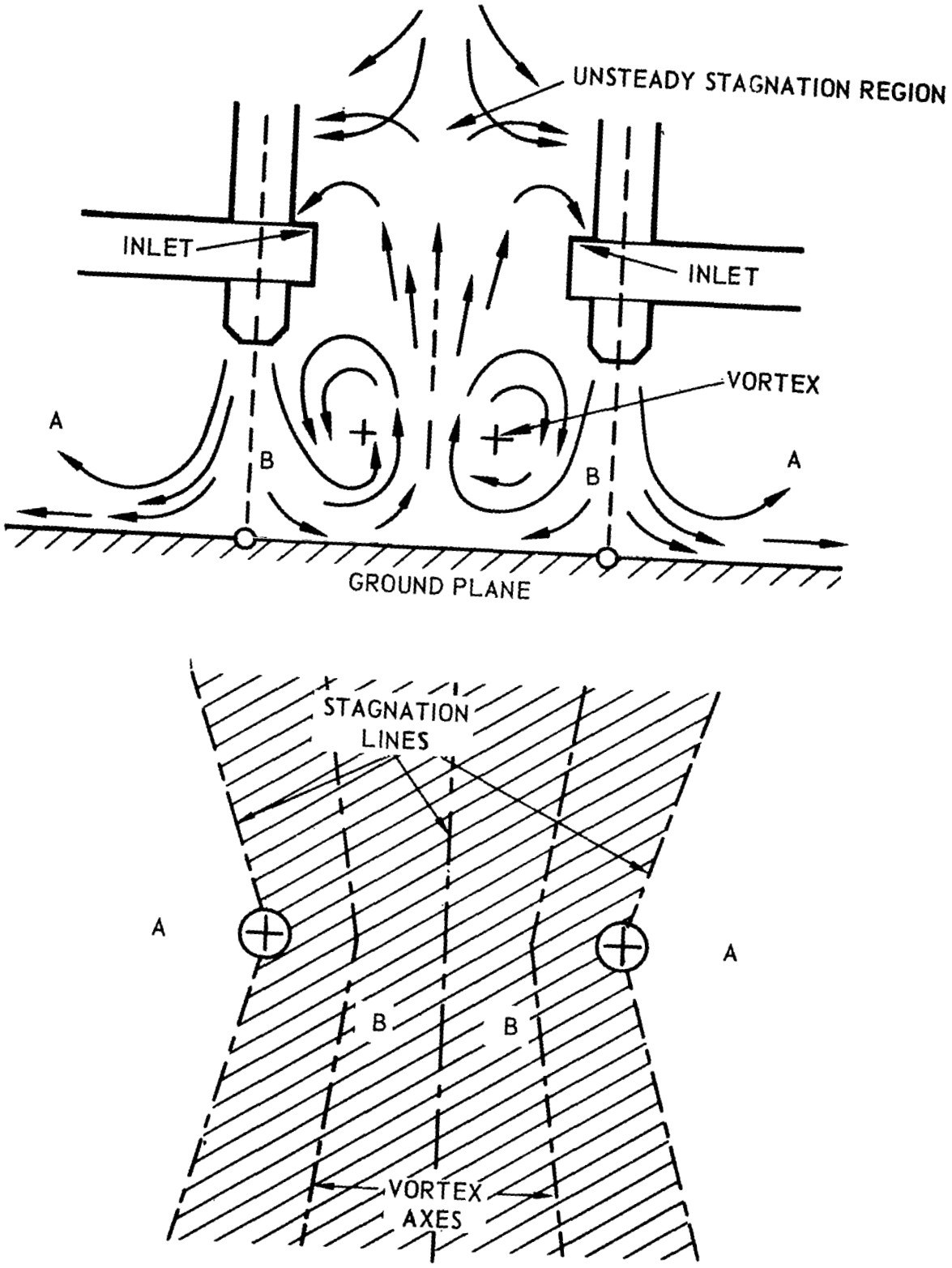

FIGURE 61. NOMINAL FLOW FIELD WITH VERTICAL NOZZLES AND EQUAL NOZZLE PRESSURES

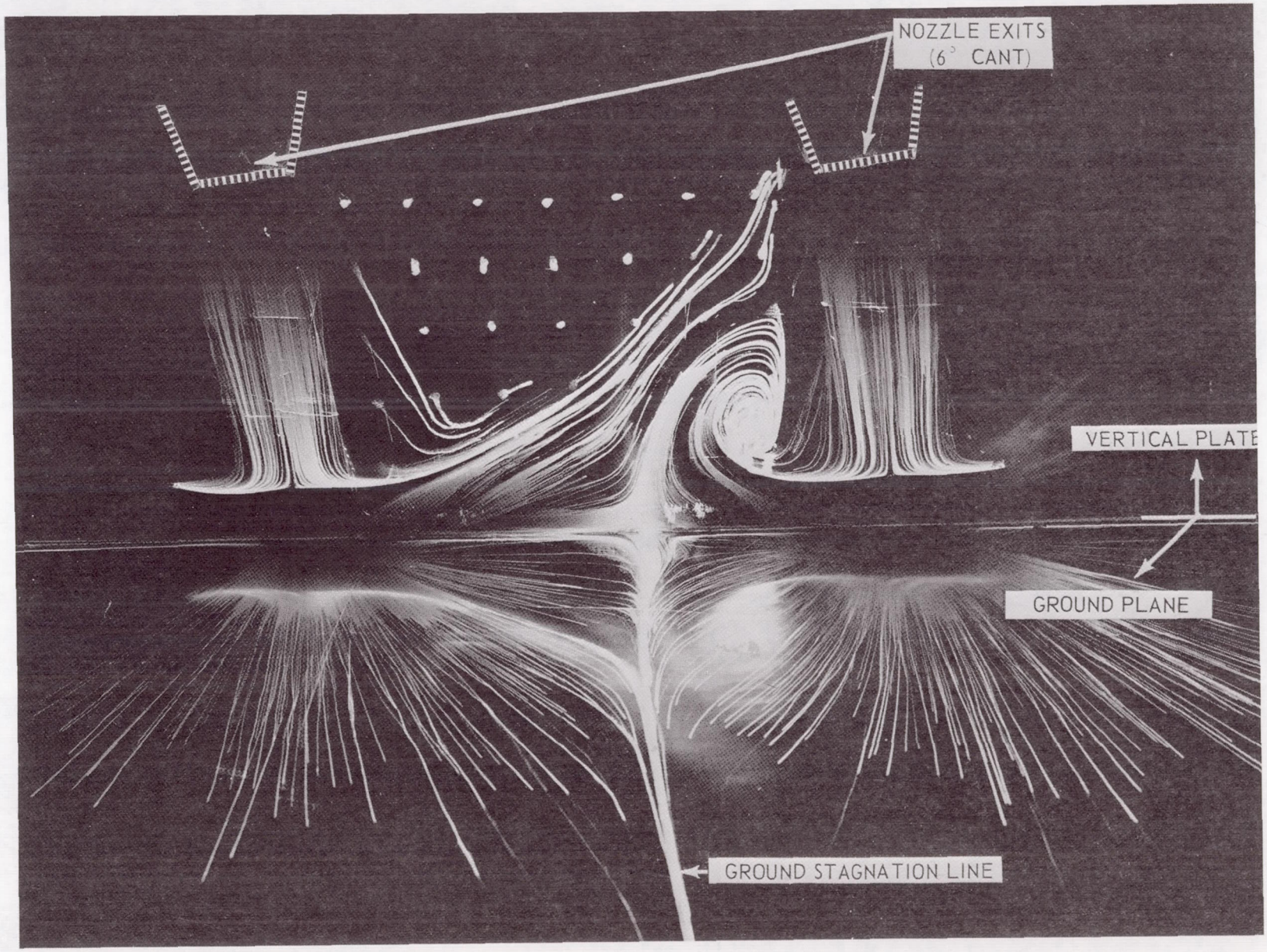

FIGURE 62 FLOW FIELD WITH CANTED NOZZLES AND EQUAL NOZZLE PRESSURES

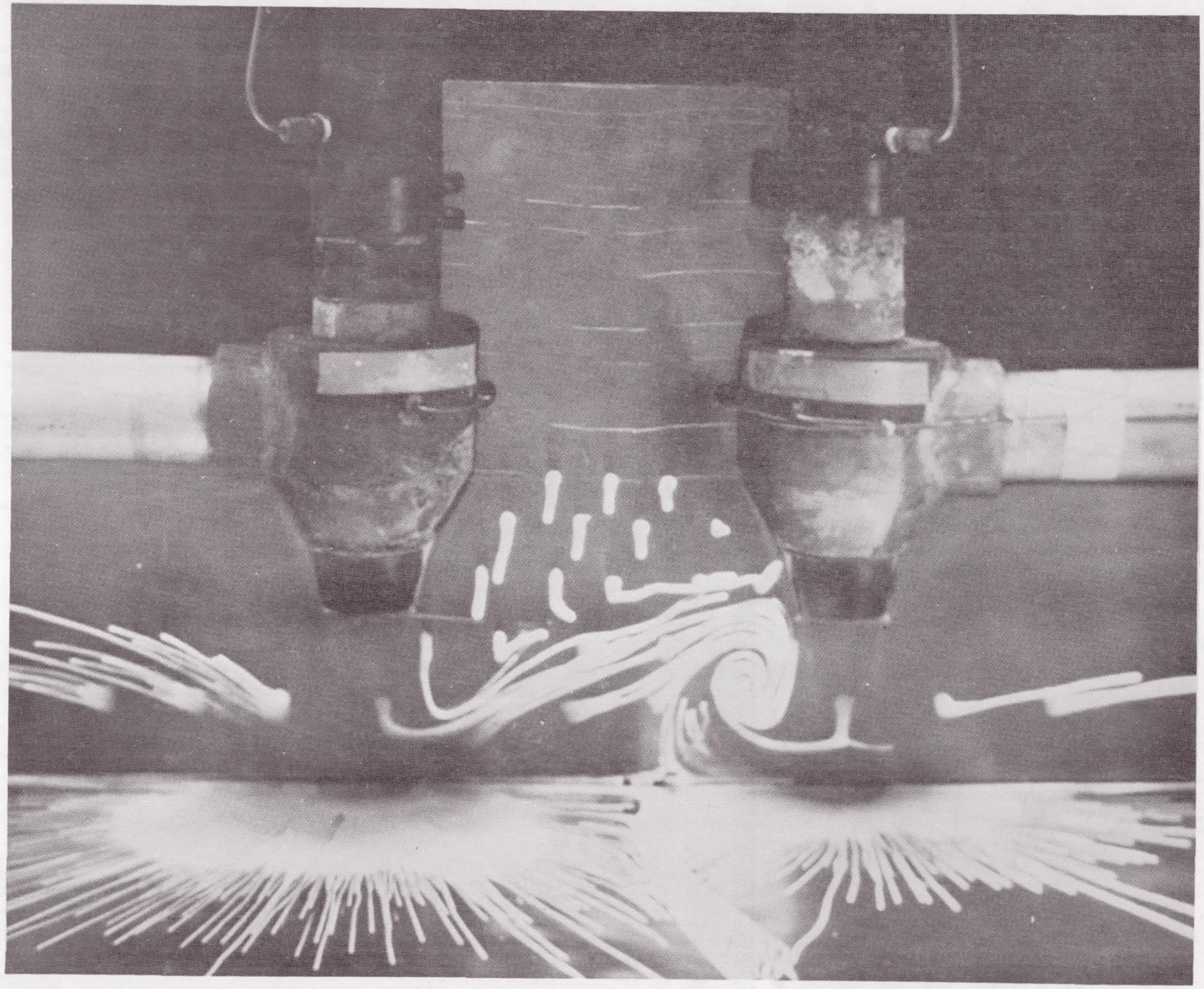

FIGURE 63 FLOW FIELD WITH VERTICAL NOZZLES AND NOZZLE PRESSURE IMBALANCE

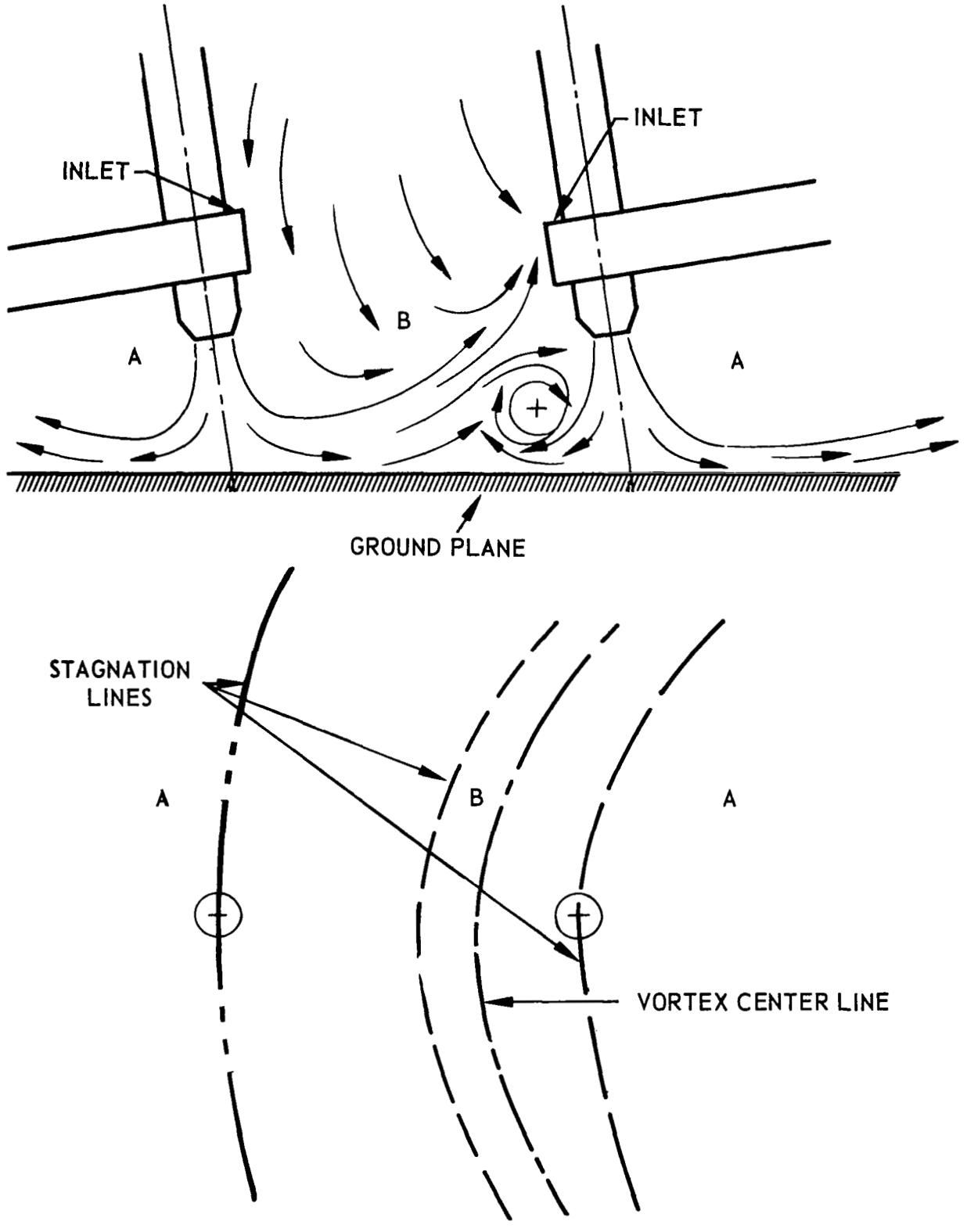

FIGURE 64. FLOW FIELD WITH CANTED NOZZLES OR NOZZLE PRESSURE IMBALANCE

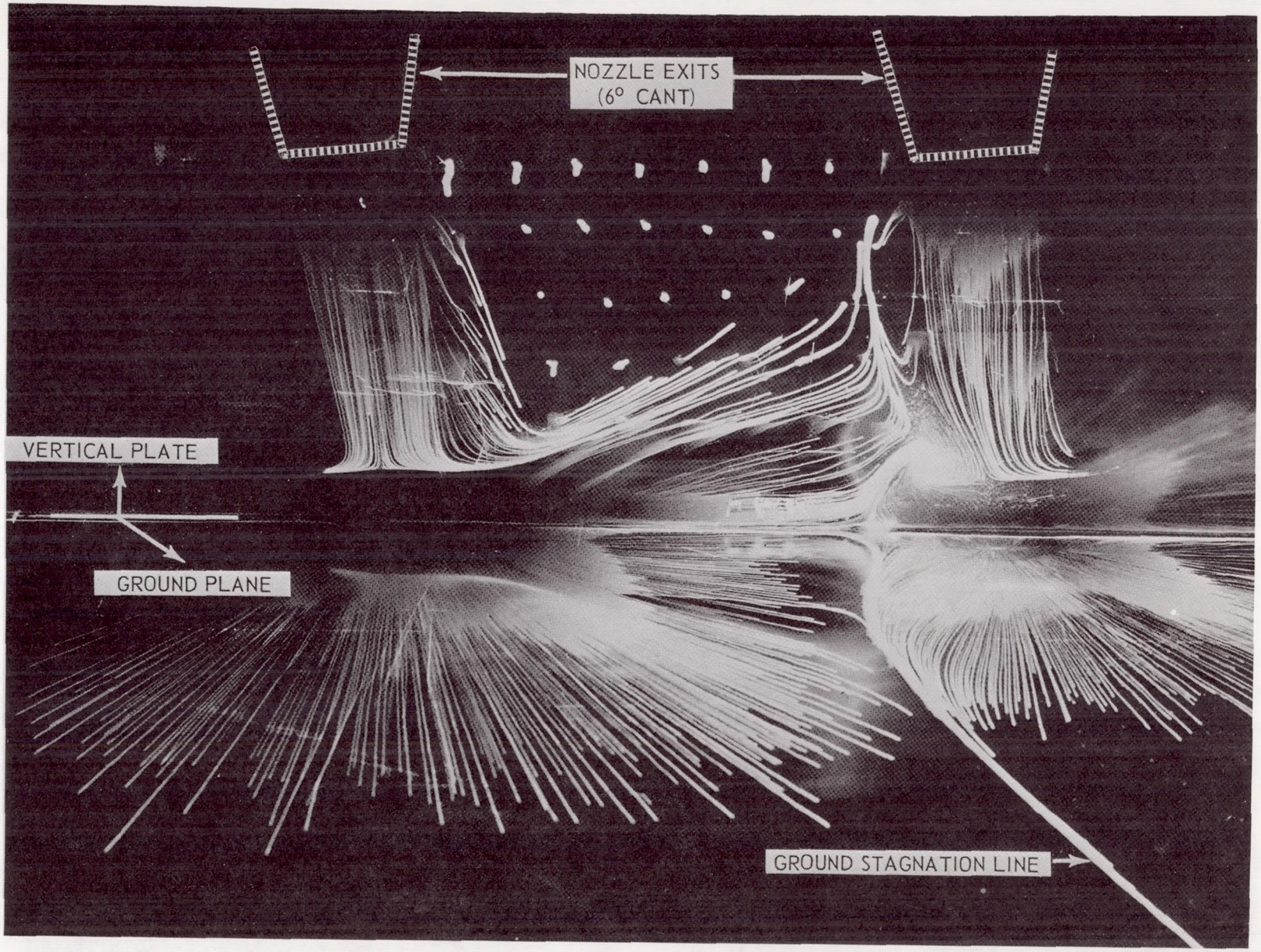

FIGURE 65 FLOW FIELD WITH CANTED NOZZLES AND NOZZLE PRESSURE IMBALANCE

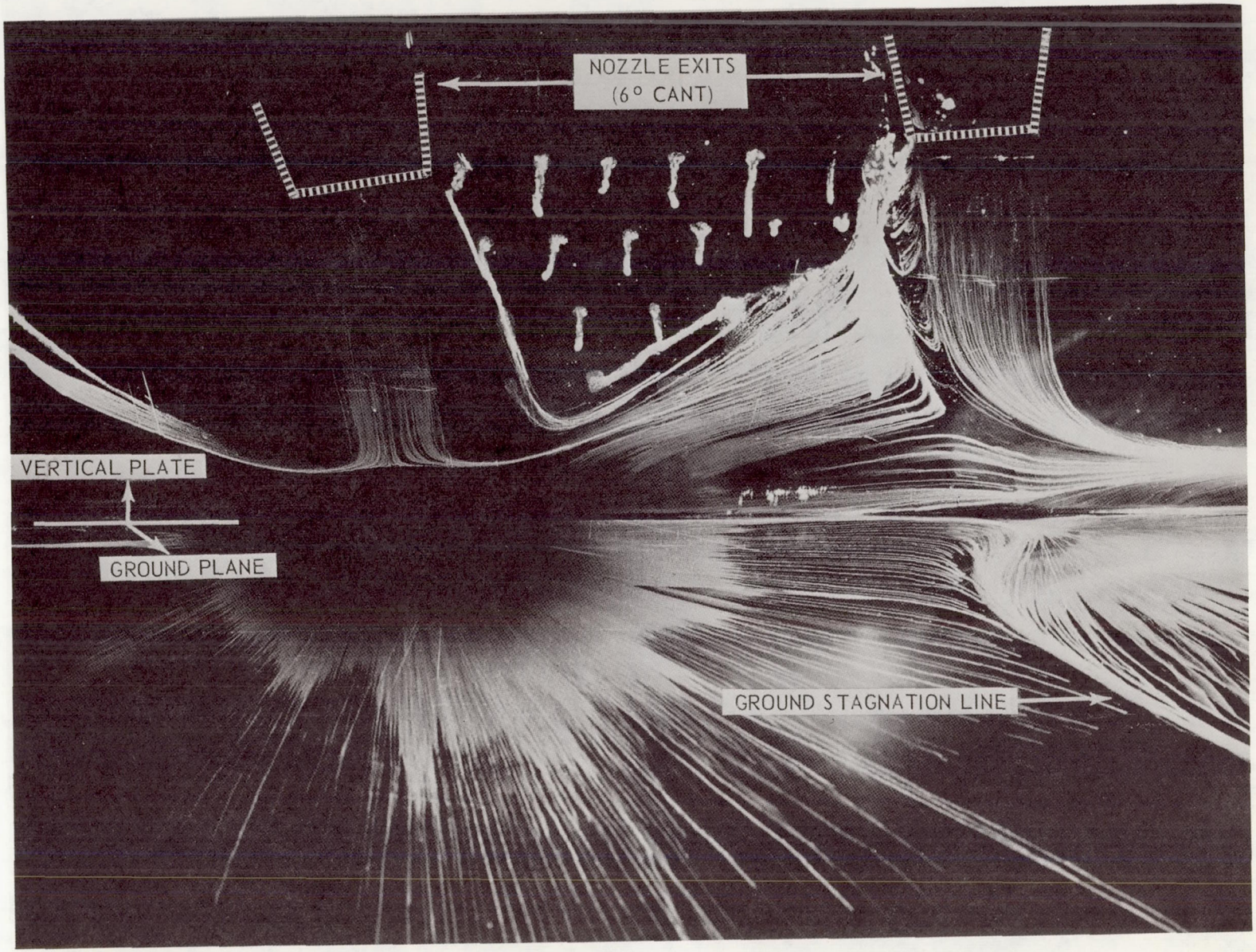

FIGURE 66 FLOW FIELD WITH CANTED NOZZLES AND INCREASED NOZZLE PRESSURE IMBALANCE

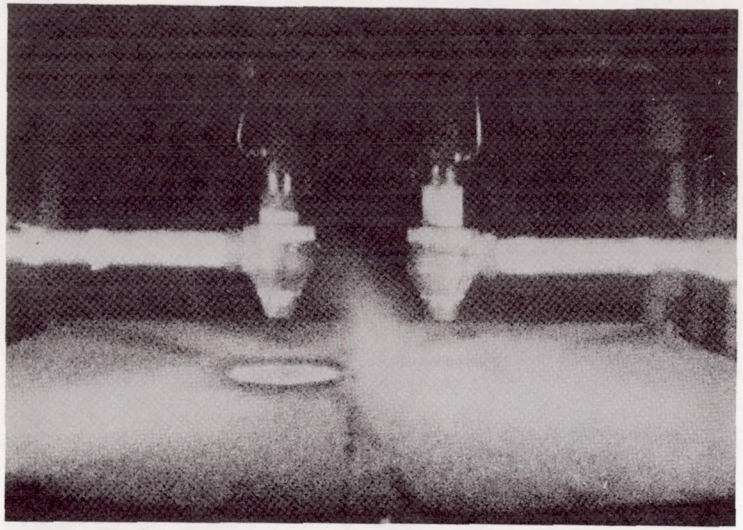

(a)

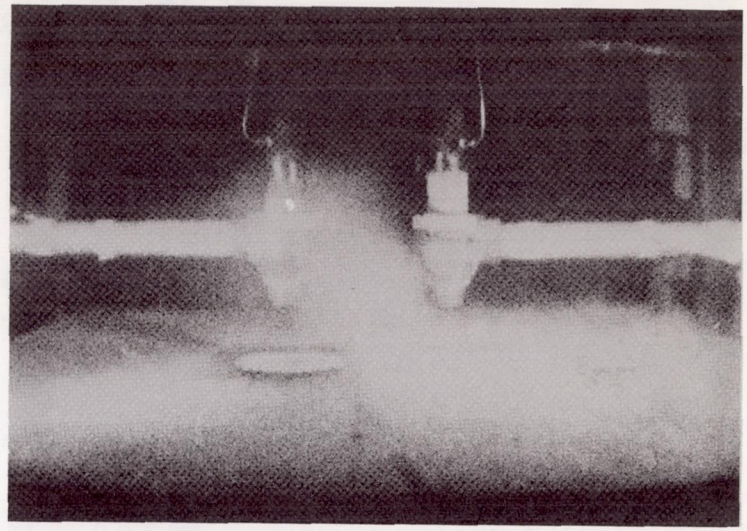

(b)

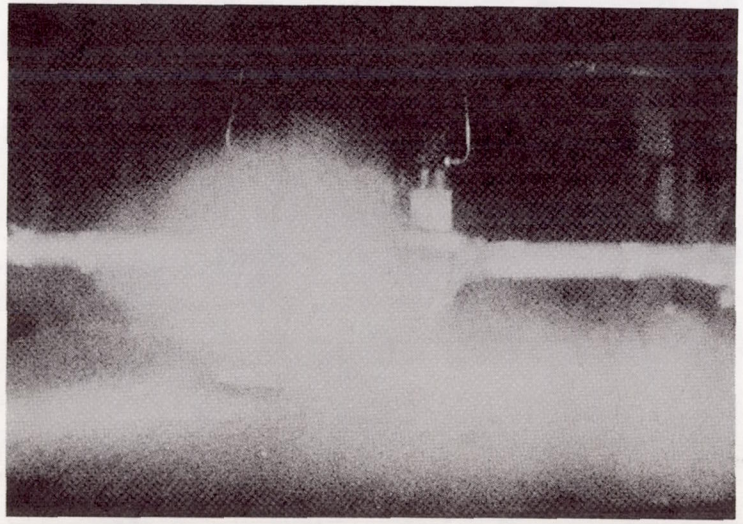

(c)

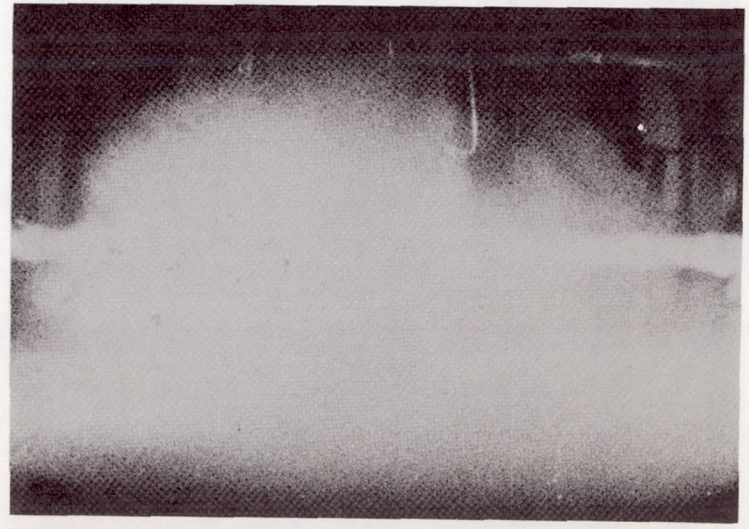

(d)

FIGURE 67 FLOW VISUALIZATION – VERTICAL NOZZLES AND EQUAL NOZZLE PRESSURES (SMOKE INTRODUCED FROM RIGHT NOZZLE)

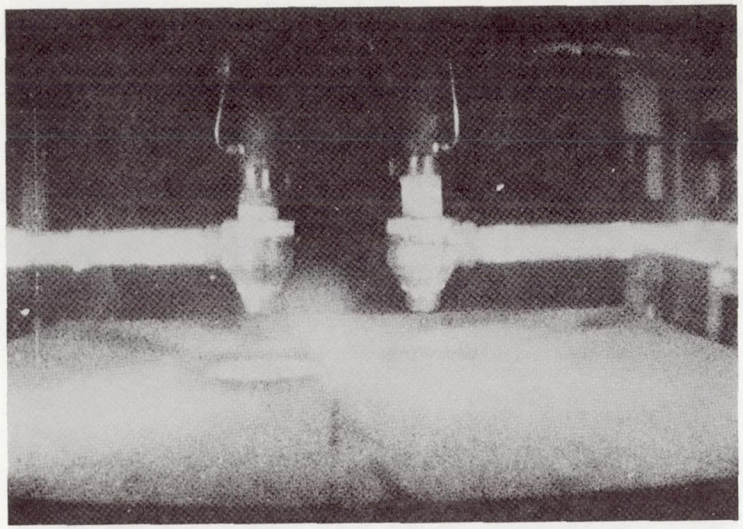

(a)

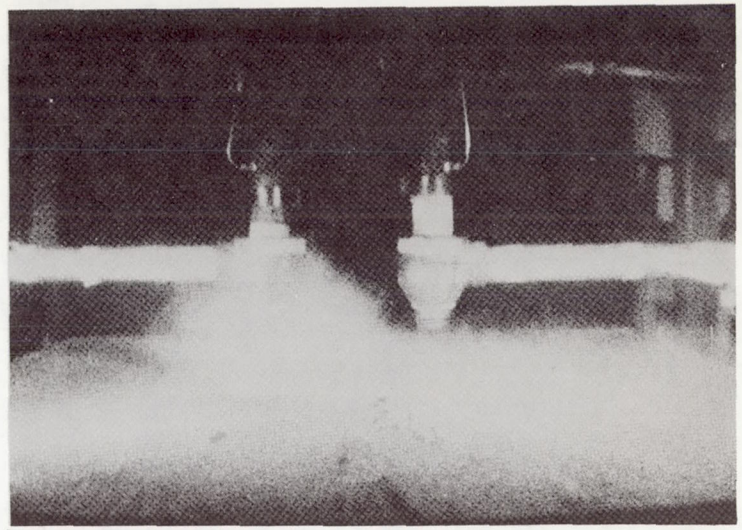

(b)

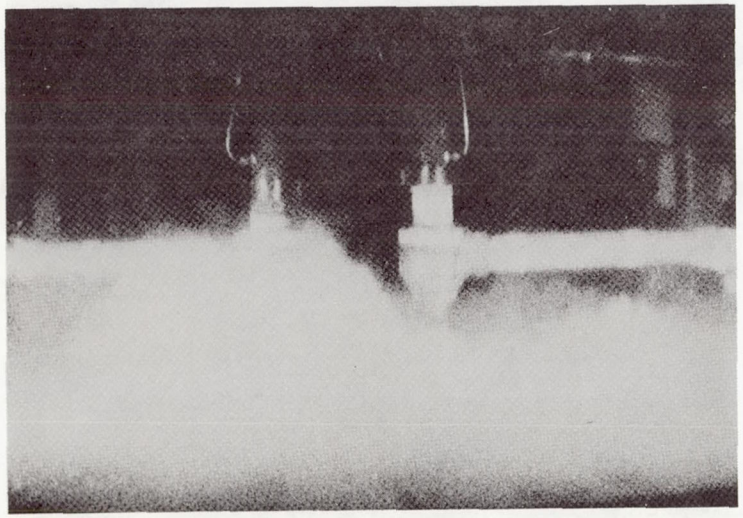

(c)

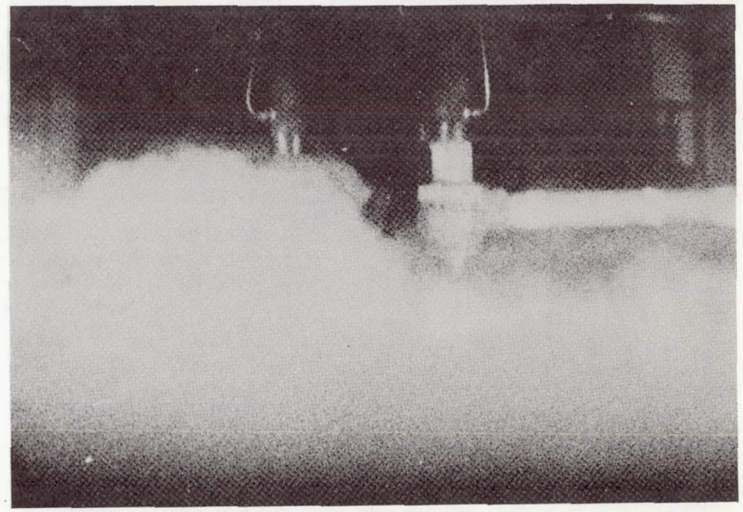

(d)

FIGURE 68 FLOW VISUALIZATION – VERTICAL NOZZLES AND NOZZLE PRESSURE IMBALANCE
(SMOKE INTRODUCED FROM RIGHT NOZZLE)

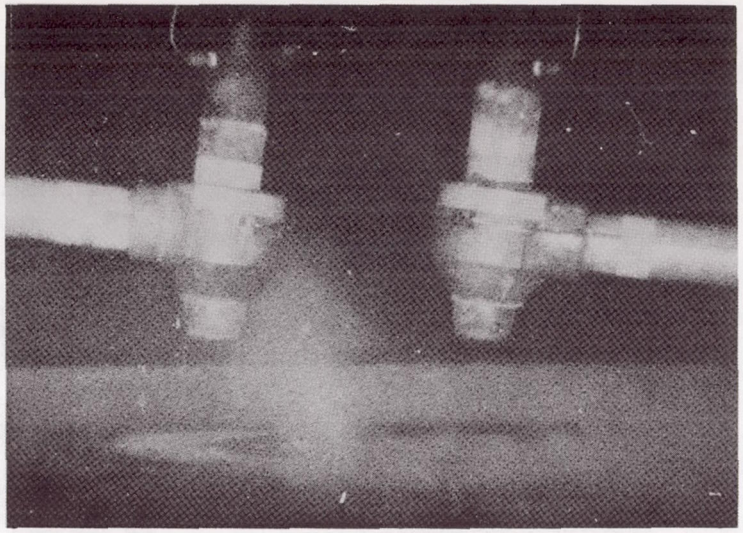

(a)

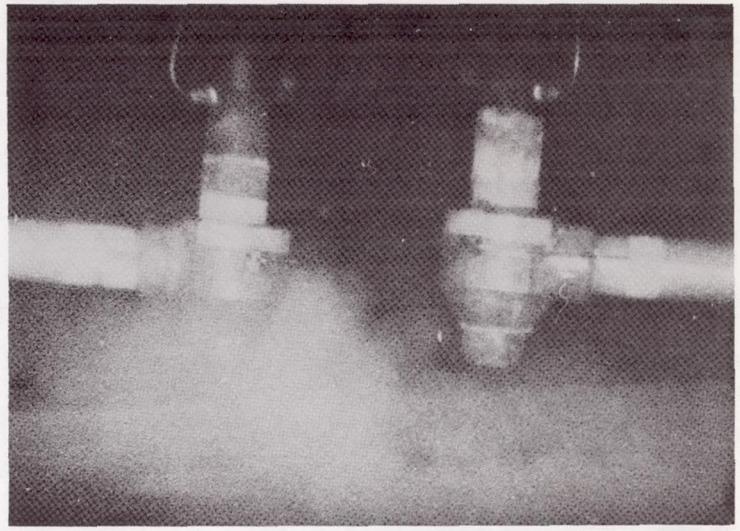

(b)

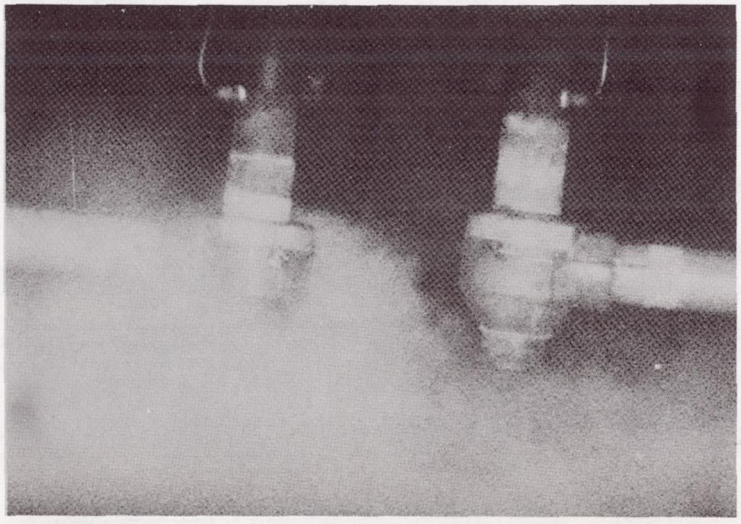

(c)

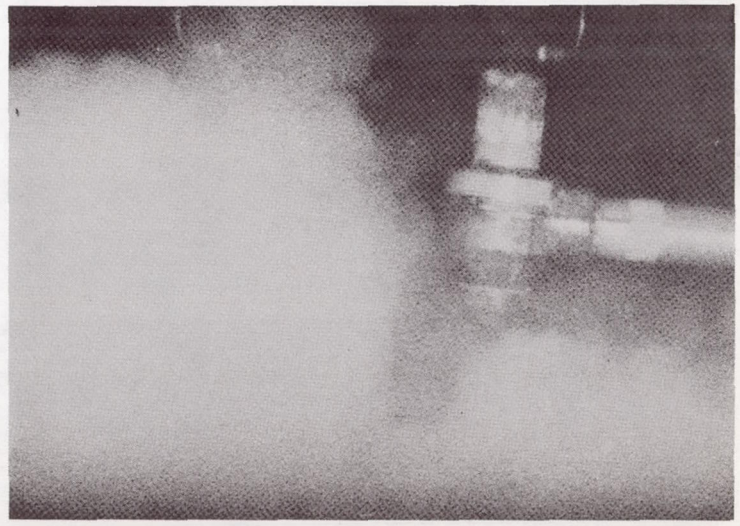

(d)

FIGURE 69 FLOW VISUALIZATION – NOZZLE CANT ANGLE AND EQUAL NOZZLE PRESSURES (SMOKE INTRODUCED FROM RIGHT NOZZLE)

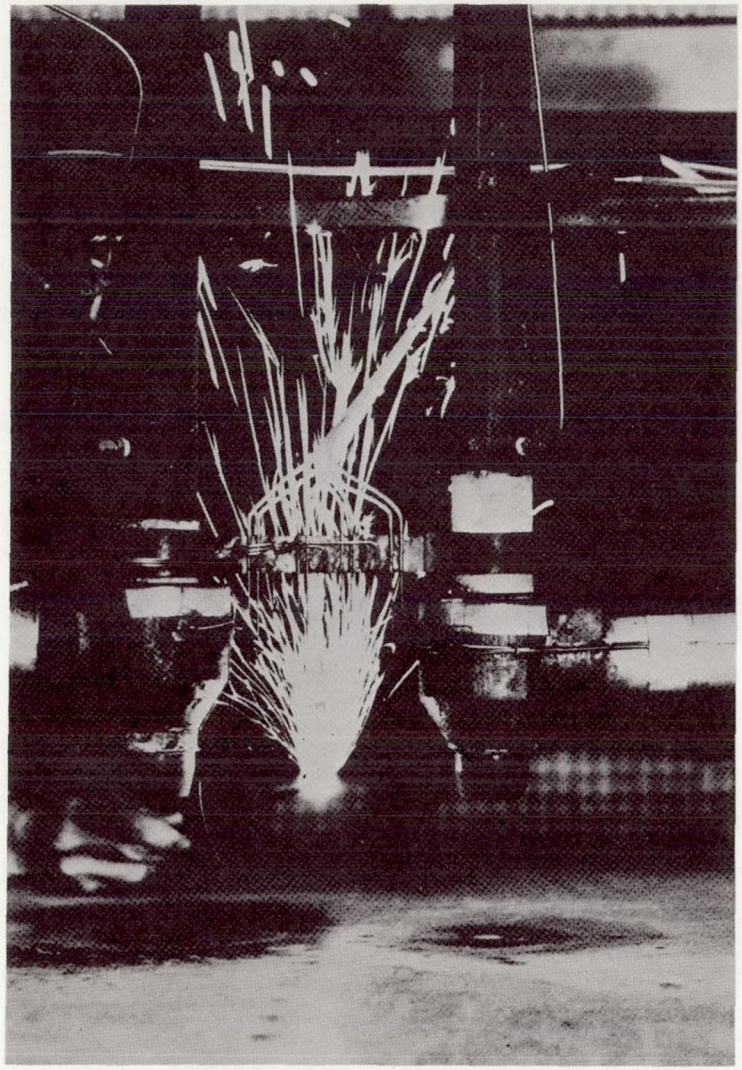

(a) VERTICAL NOZZLES AND EQUAL NOZZLE PRESSURES

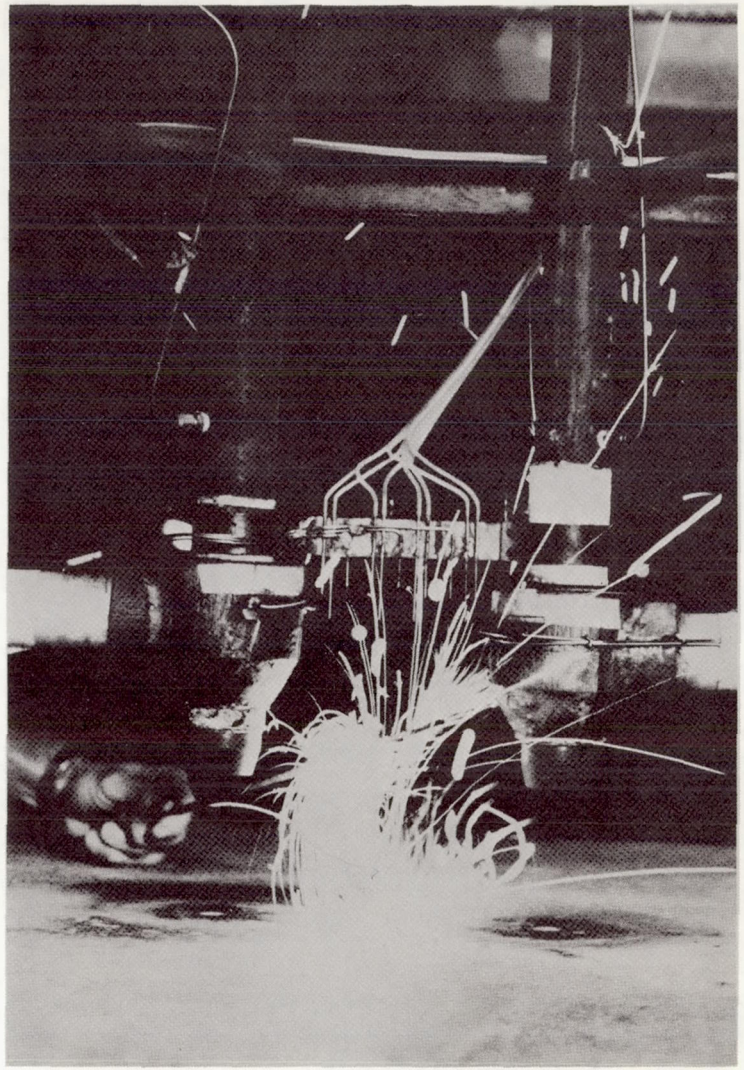

(b) VERTICAL NOZZLES AND NOZZLE PRESSURE IMBALANCE

FIGURE 70 FLOW VISUALIZATION WITH SPARKLERS

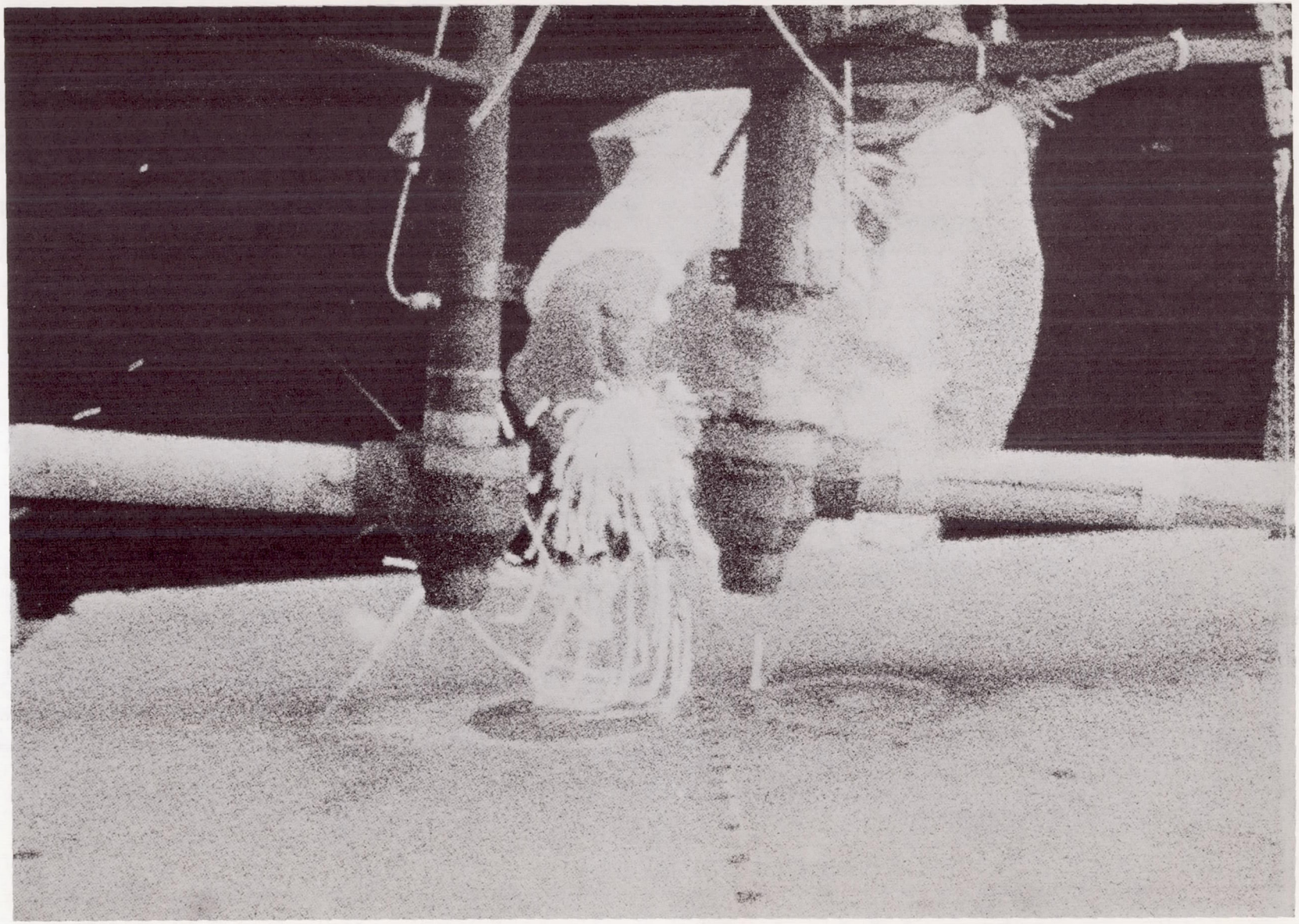

FIGURE 71 FLOW VISUALIZATION WITH SPARKLERS – NOZZLE CANT ANGLE 6° AND EQUAL NOZZLE PRESSURES

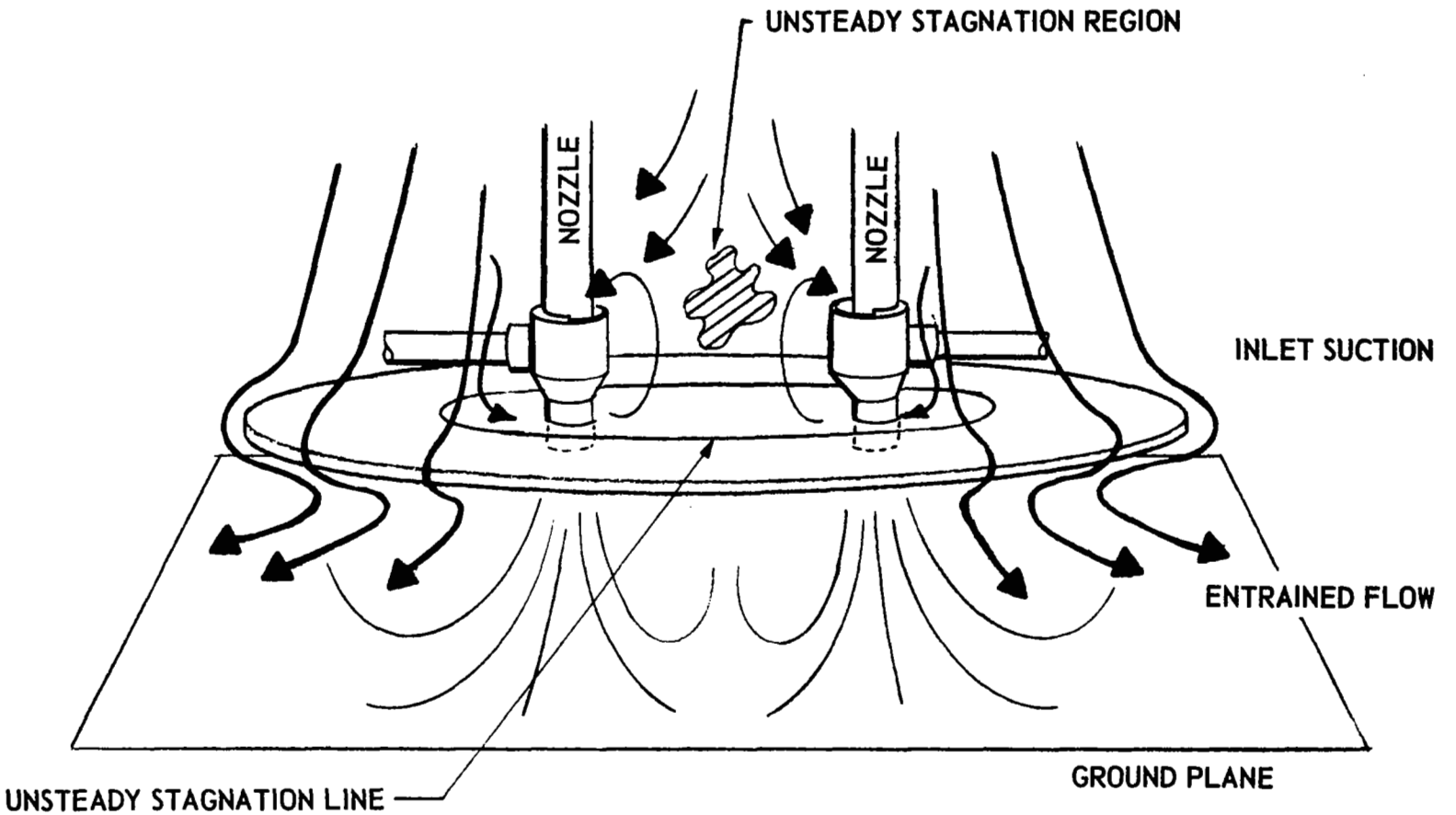

FIGURE 72. FLOW WITH BLOCKAGE DISCS FOR HIGH H/D

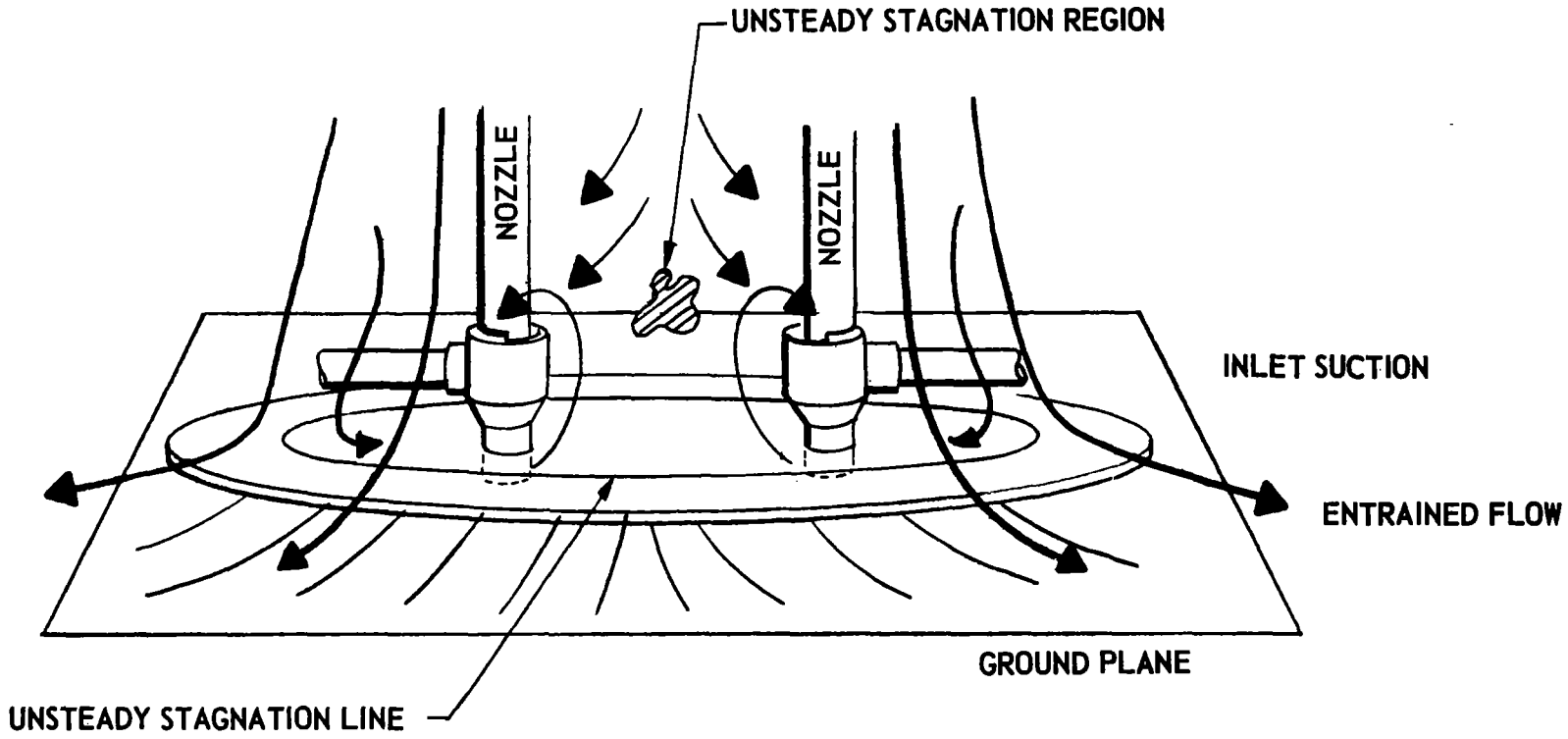

FIGURE 73. FLOW WITH BLOCKAGE DISCS FOR LOW H/D

H/D = 3.0
S/D = 7.0

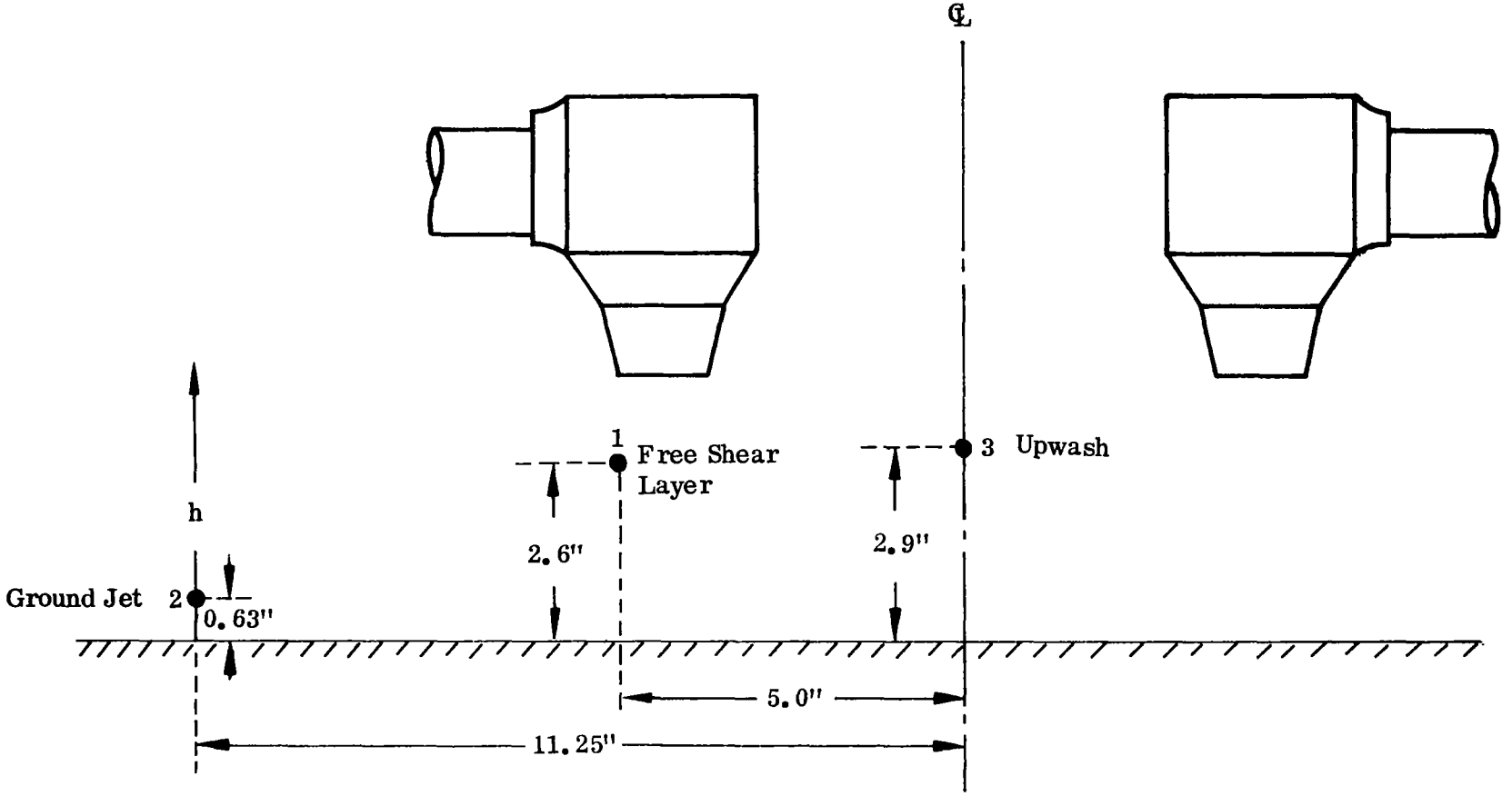

FIGURE 74. HOT WIRE POSITIONS

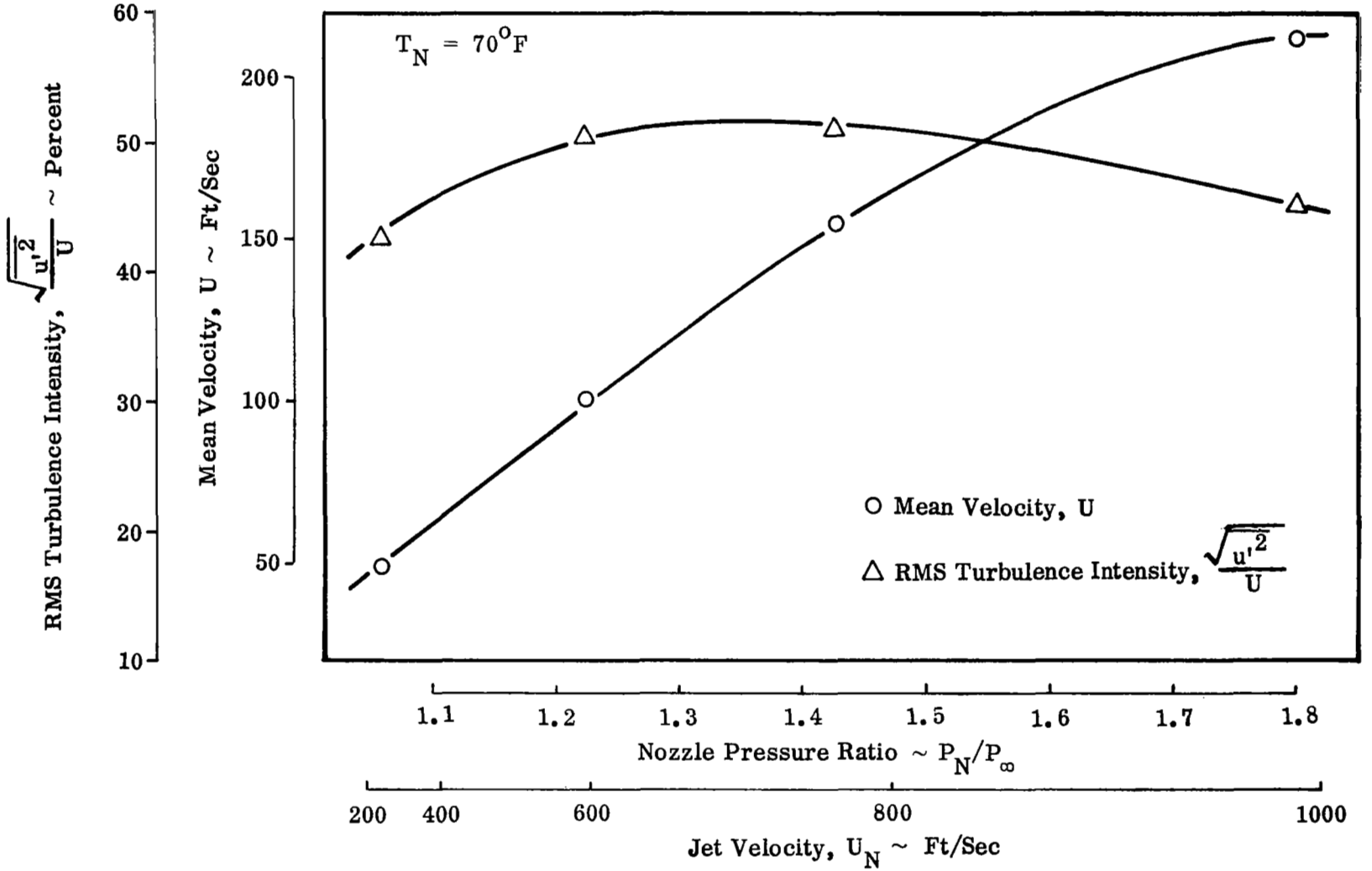

FIGURE 75. UPWASH VELOCITY AND TURBULENCE INTENSITY

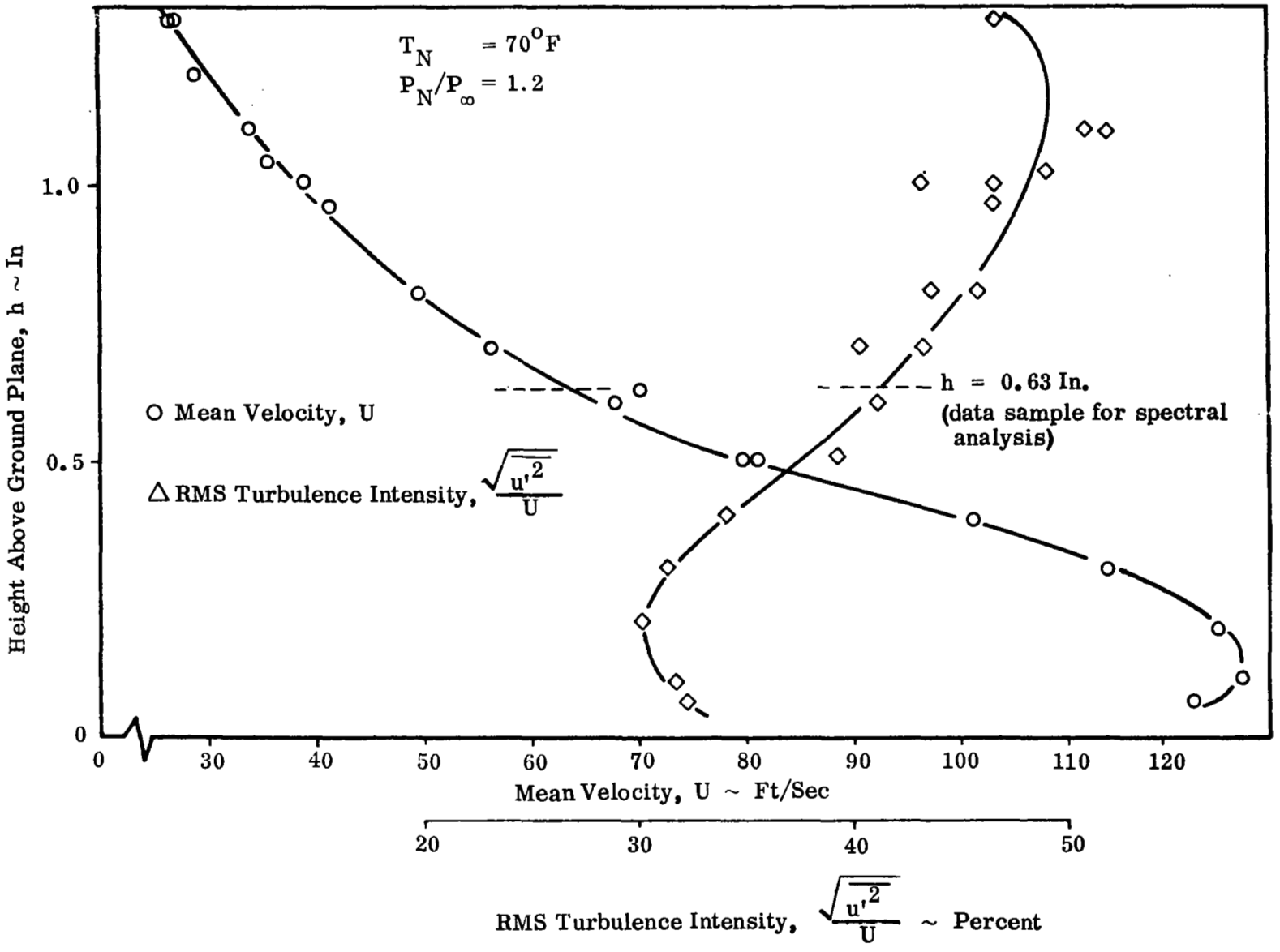

FIGURE 76. GROUND JET VELOCITY AND TURBULENCE INTENSITY

$T_N = 70^oF$

$P_N/P_\infty = 1.2$

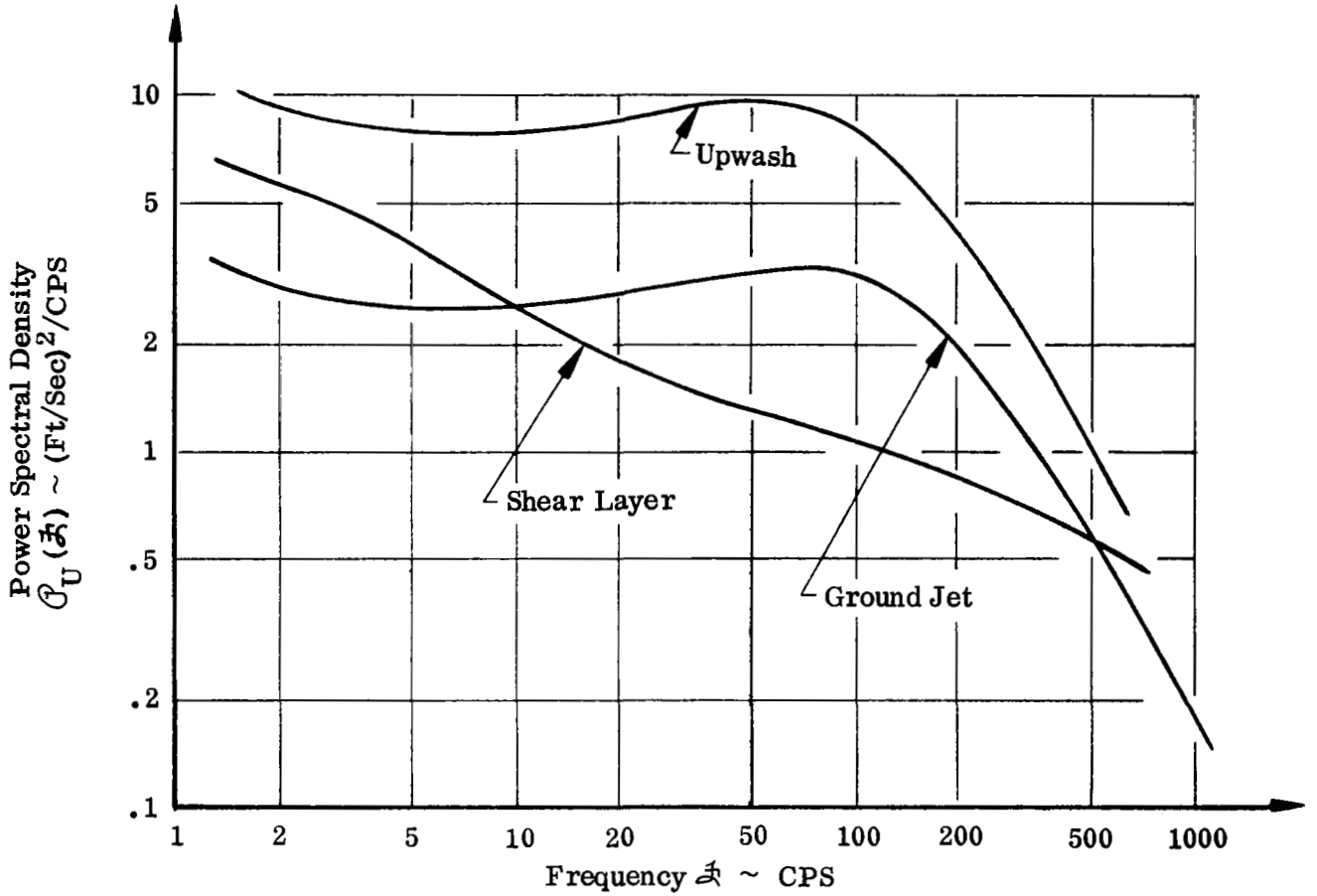

FIGURE 77. VELOCITY FLUCTUATION POWER SPECTRAL DENSITY

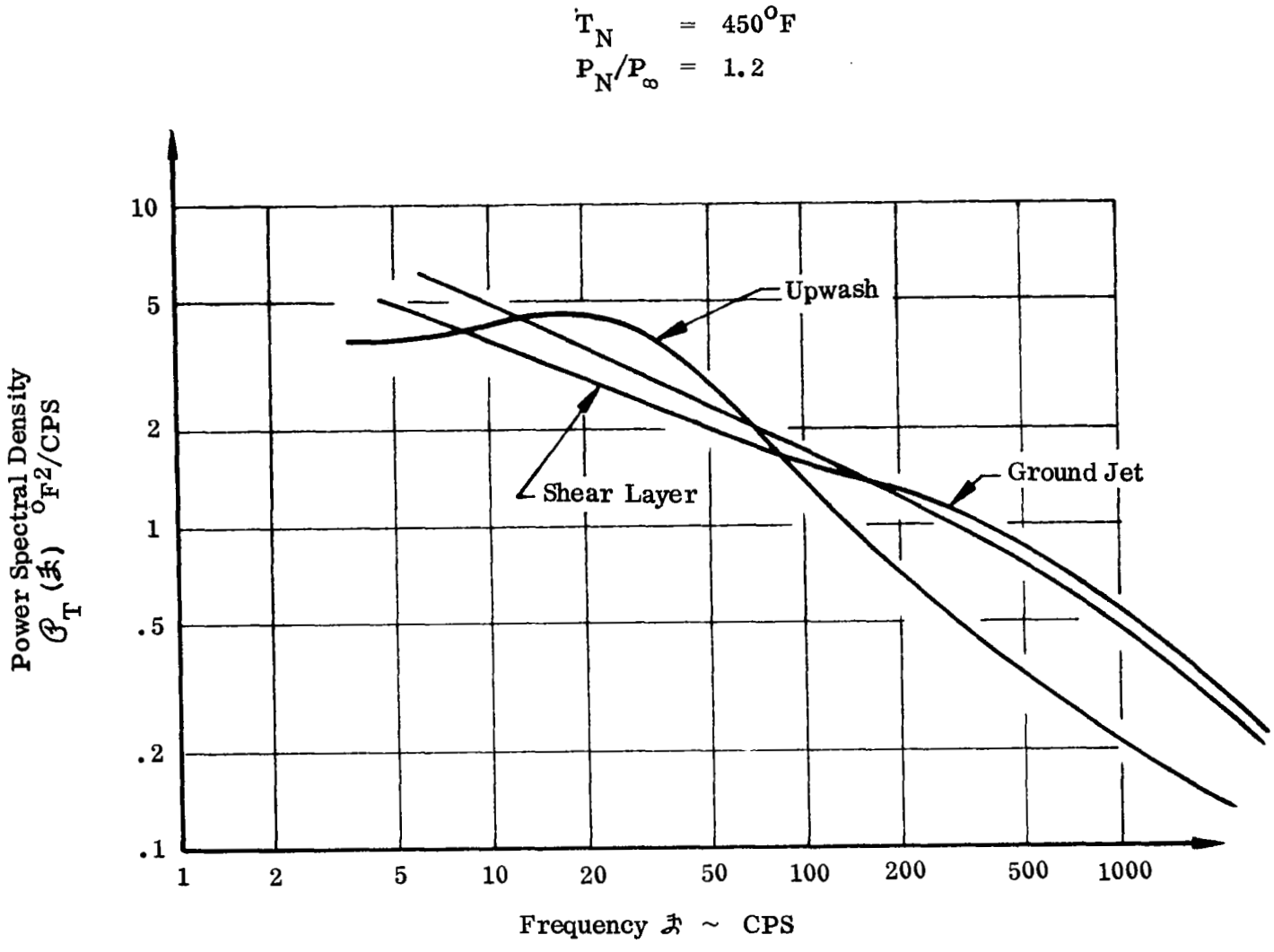

FIGURE 78. TEMPERATURE FLUCTUATION POWER SPECTRAL DENSITY